Division of Earth Resource Science
Faculty of International Resource Sciences
Akita University

Mukuka Simusokwe (D6518109)

Lithology, Alteration and Mineralization of the Fishtie Cu-Co Deposit, Zambian Copperbelt

Doctor Dissertation

September 2021

Abstract

Fishtie is a copper-rich deposit situated southeast of the Zambian Copperbelt (ZCB), about 30 km north of Mkushi town, close to the international boundary between Zambia and the Democratic Republic of Congo. The deposit was discovered in 2004 by First Quantum Minerals (FQM) Limited through systematic application of soil geochemistry, magnetic survey and drilling. This drilling intersected 300 meters wide by over a kilometre long east-west striking copper orebody similar to the ZCB deposits, but hosted at a higher stratigraphic position in the Katanga Supergroup. The reserves are estimated at 55 Mt of copper at an average grade of 1.04%, occurring as oxide, sulfide and mixed oxide-sulfide ores. Cobalt-rich orebodies are present within the copper orebody, but the two metals show different vertical enrichment and depletion trends.

This study was conducted to investigate the following geological characteristics of the Fishtie deposit: (1) the source of the metals, especially copper and cobalt; (2) the source of sulfur; (3) the physical and chemical characteristics of the lithology that are responsible for copper and cobalt mineralization; (4) the timing of mineralization; and (5) the factors controlling the spatial distribution of copper and cobalt metals.

Petrographic results of samples from the Grand Conglomérat Formation sitting on the basement rocks shows chalcopyrite preferentially disseminated in chlorite-rich clasts. These clasts weathered from basement mafic rocks and are considered to be the source of copper and cobalt. Copper and cobalt were leached from detrital mafic minerals during hydrothermal alteration and metamorphism, resulting in decomposition of clasts to chlorite and chalcopyrite. Mineral chemistry of alteration minerals suggest that copper and cobalt were liberated as ions during the alteration of chlorite to biotite. The metal ions were transported to the site of deposition through post-folding faults which provided conduits for the oxidizing mineralizing fluids. Copper and cobalt precipitated as chalcocite, bornite, chalcopyrite, cobaltite and carrollite at the boundary of dolostone and reduced beds of alternating siltstone and sandstone. High-grade copper mineralization of chalcopyrite and bornite formed in folded beds of alternating siltstone and sandstone which acted as traps for mineralizing fluids and hydrocarbons. Copper and cobalt mineralization is zoned from deeper level sulfide mineralization to a shallow supergene mineralization of chalcocite, malachite, heteroginite and cobaltoan dolomite.

Table of Contents

List of Figures

List of Tables

Declaration

I declare that the dissertation entitled *Lithology, Alteration and Mineralization of the Fishtie Cu-Co Deposit, Zambian Copperbelt*, is my own work, that it has not been submitted for any degree or examination in any other university, and that all the sources I have used or quoted have been indicated and acknowledged by complete references.

Acknowledgements

First and foremost, I would like to thank God for his love, goodness, grace and mercy without which accomplishing this work would have been difficult. He is the provider of all knowledge.

Prof. Y. Watanabe and Dr. T. Echigo are deeply thanked for their supervision. Their supervision of this thesis and academic support are greatly appreciated. Prof. T. Echigo is further thanked for taking time to help with XRD, SEM-EDS and EMPA analysis.

All members of the Mineral Resources and Tectonics Laboratory are thanked for the different roles they played during this research.

I would like to extend my appreciation to the staff and management of First Quantum Minerals Ltd for granting permission to work on the Fishtie project.

It would be incomplete if I don't recognize the encouragement and love that I received from my family (brothers, sisters, cousins) during the course of this work. The Zambian and African communities with whom the author associated whilst in Japan were ever so friendly and supportive.

Lastly but not the least, the Japan International Co-operation Agency (JICA) is thanked for the scholarship and financial support they provided to conduct this research.

Chapter 1 Introduction

1.1 Background

Copper and cobalt are critical raw materials driving the Green Revolution because of their wide applications in energy storage, electric motors, distribution and fuel and hardware (Oberle et al., 2019). Approximately 20% of the copper and 60% cobalt production in the world is sourced from sediment-hosted copper deposits (Brown et al., 2019; Hitzman et al., 2017). Sediment-hosted copper deposits are distributed in basins throughout the world (Fig. 1). The Central African Copperbelt (CACB) which encompasses deposits of the Zambian Copperbelt (ZCB), Congo Copperbelt (CCB) and North-Western Province of Zambia, is the largest sediment-hosted copper province on Earth, containing ~200Mt and 5Mt of copper and cobalt metals, respectively (Hitzman et al., 2012). Copper and cobalt deposits of the CACB are hosted in metasedimentary rocks belonging to the Katanga Supergroup of Neoproterozoic-early Palaeozoic age (McGowan et al., 2003).

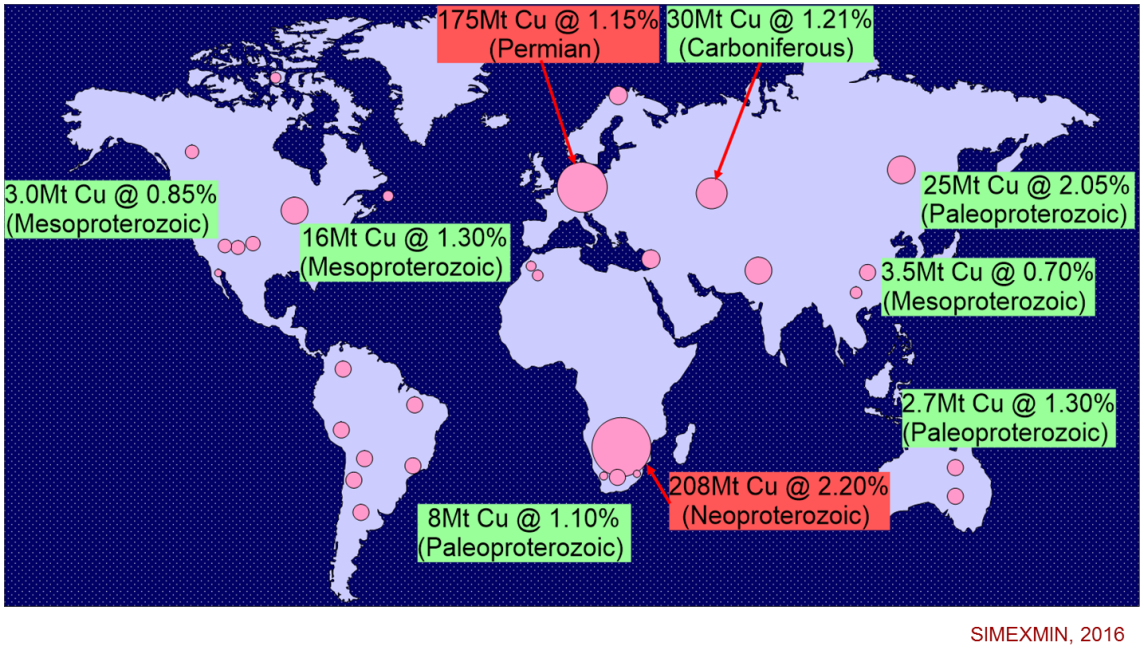

Figure 1: Distribution of the sediment-hosted copper provinces of the world and the ages of the basins. The two supergiant deposits, the Central African Copperbelt (CACB) (Neoproterozoic) and the Kupferschiefer (Permian) are shown in red squares.

Fishtie is a recently discovered sediment-hosted copper deposit in the southeast of the ZCB, close to the international boundary between Zambia and the Democratic Republic of Congo (Fig. 2). The Fishtie copper deposit was discovered by First Quantum Minerals (FQM) Limited in 2004 through systematic application of soil geochemistry and magnetic surveys, followed by drilling of over 200 diamond boreholes in 2010 (Hendrickson et al., 2015). This drilling intersected a copper orebody measuring 300 meters wide by over 1-kilometer long in plan view, elongating along the east-west strike (Hendrickson et al., 205). The copper deposit is hosted in the Katanga Supergroup rocks, similar to the sequence of rocks hosting the sediment-hosted copper deposits in the ZCB, CCB and North-Western Province. Copper reserves at the Fishtie deposit are estimated at about 55Mt of copper ore at an average cut-off grade of 1.04%, occurring as oxide, sulfide and mixed oxide-sulfide ores (Hitzman et al., 2012).

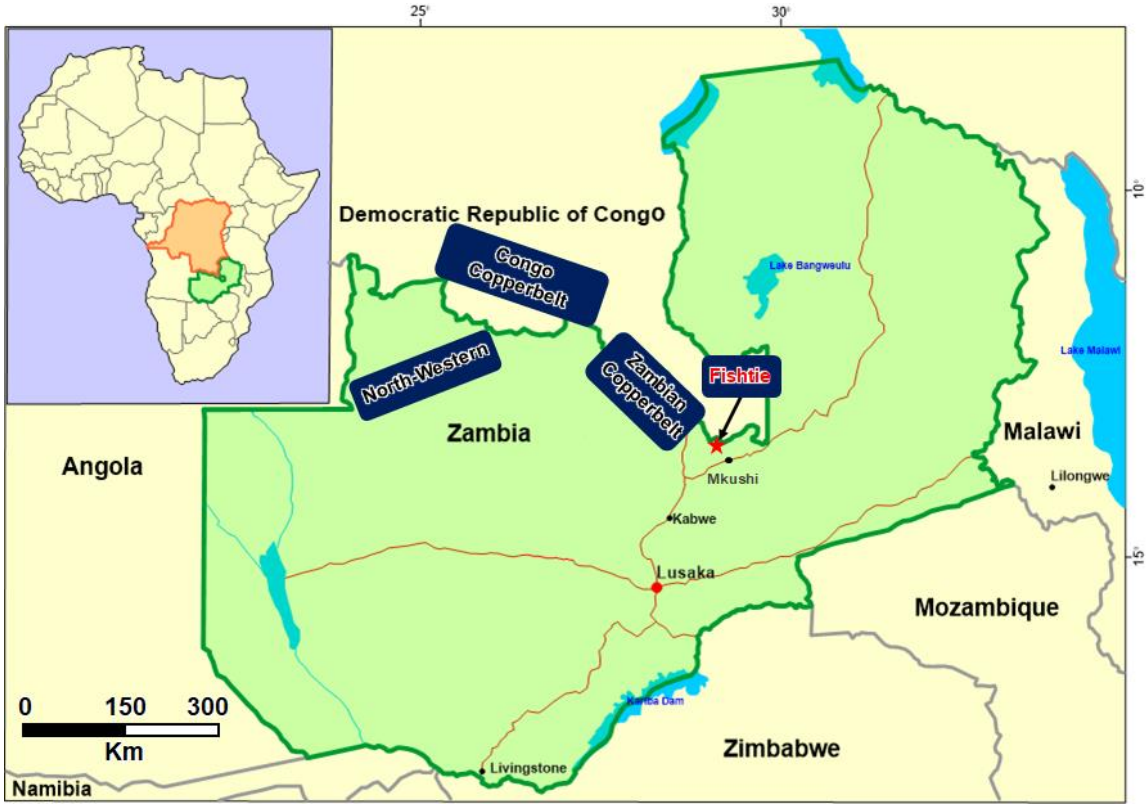

Figure 2: Location of the sediment-hosted copper districts of the Central African Copperbelt (CACB): Zambian Copperbelt (ZCB), Congo Copperbelt (CCB) and North-Western Province of Zambia. Fishtie copper deposit is located southeast of the ZCB.

In terms of size perspective, the Fishtie deposit is relatively small compared to other sediment-hosted copper deposits in the ZCB, CCB and the world (Fig. 3). Despite the small size, proximity to the highly prospective ZCB region, favourable deposit geometry and development of high-grade supergene copper and cobalt mineralization in the upper zones of the stratigraphy, make Fishtie an attractive deposit (Hendrickson et al., 2015).

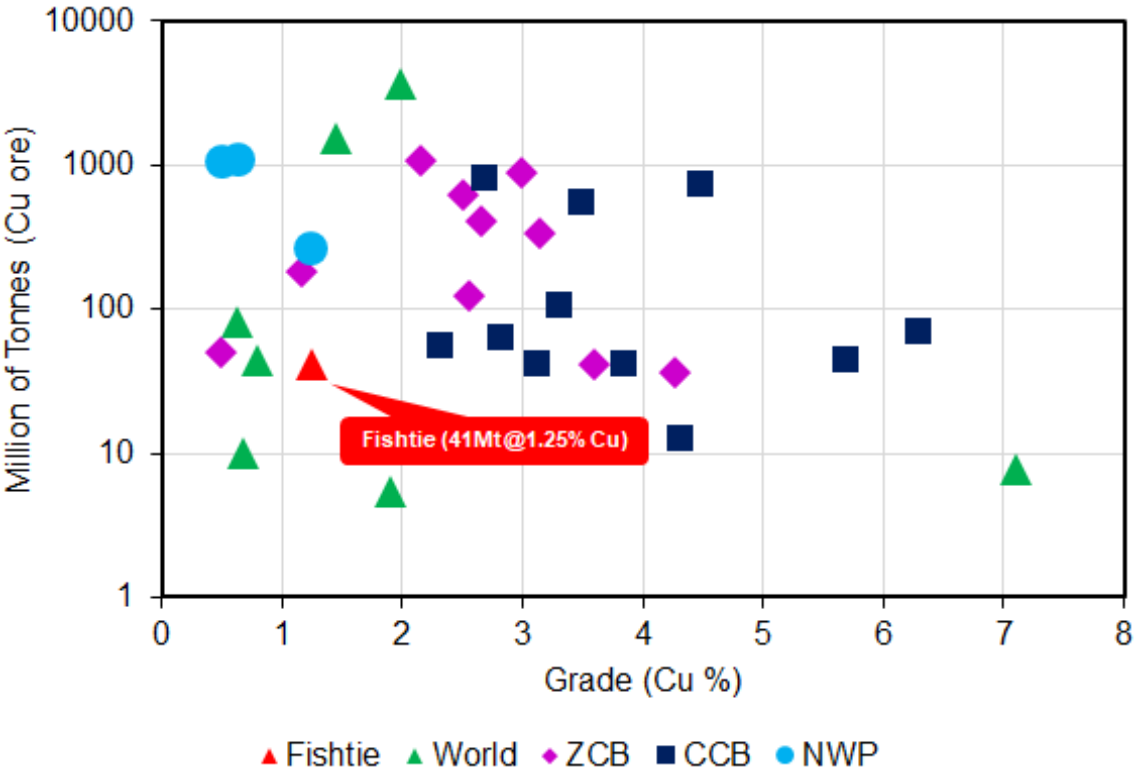

Figure 3: Comparison of copper reserves and grade at the Fishtie deposit with major deposits in the Zambian Copperbelt (ZCB), Congo Copperbelt (CCB), North-Western Province (NWP) of Zambia and the world. Data sources: World = USGS Global Mineral Resource Assessment (2010), Fishtie, ZCB, CCB and NWP = Hitzman et al, 2012.

1.2 Problem definition

An assessment of the critical raw materials used in modern technology by the European Union shows that compared with copper, cobalt has a higher supply risk (Fig. 4). This is

attributed to one of the most important characteristics in the cobalt supply chain where production is concentrated in two countries: mining in the Democratic Republic of Congo and refining in China. From a mining perspective, over 50% of the global cobalt supply is extracted from the Democratic Republic of Congo (Fig. 4). To secure a stable future supply of cobalt, new cobalt deposits outside the Democratic Republic of Congo need to be discovered and developed.

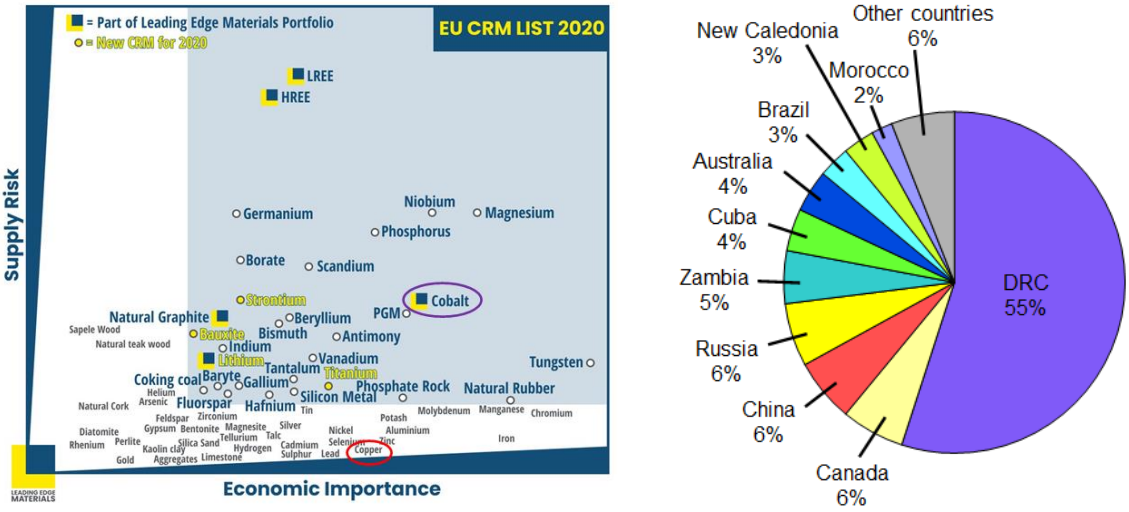

Figure 4: Assessment of critical raw materials used in modern technology and the Top 10 cobalt producing countries in the world. Data sources: Study on the EU's list of Critical Raw Materials (2020), Hitzman et al (2017).

Cobalt is mainly recovered as a by-product of copper mining from the sediment-hosted copper deposits of the CCB and ZCB (Hitman et al., 2017; Mudd et al., 2013). These copper deposits formed in regions that form distinct linear belts and alignments in the CACB (Fig. 5). The ZCB has fewer deposits but consists of most of the giant deposits which hosts about 60% of the total copper endowment of the CACB, while the CCB has many small, but fewer giant deposits, accounting for the remaining 40% copper endowment (Hitzman et al., 2017; Theron, 2013; Fig. 5). The largest and richest cobalt endowments are located mostly in the western part of the CCB, with cobalt grades of 1.1% in the Kinsanfu deposit, 0.7% at Mukondo and 0.6% at Tilwezembe (Hitzman et al., 2017; Fig. 6). In the ZCB, cobalt grades are generally low (e.g., 0.4% at

Nchanga and 0.1% at Nkana), but, because these deposits are very large, their cobalt endowment is substantial (Hitzman et al., 2017).

A review of the economic concentrations of cobalt in the ZCB deposits by Annels and Simmonds (1984) shows that cobalt does not always accompany copper and has a spatial distribution which is restricted to deposits located in a narrow zone on the western side of the Kafue anticline in the Nchanga, Chambeshi, Nkana and Baluba deposits (Fig. 6). Factors controlling this spatial distribution are not well understood, but many researchers attribute it to the metal source (Mendelsohn, 1961; Annels and Simmonds, 1984; Theron, 2013; Hitzman et al., 2017). However, the source of copper and cobalt in both the ZCB and CCB deposits is not well constrained and remains one of the unresolved problems (British Geological Survey, 2019; Selley et al., 2005).

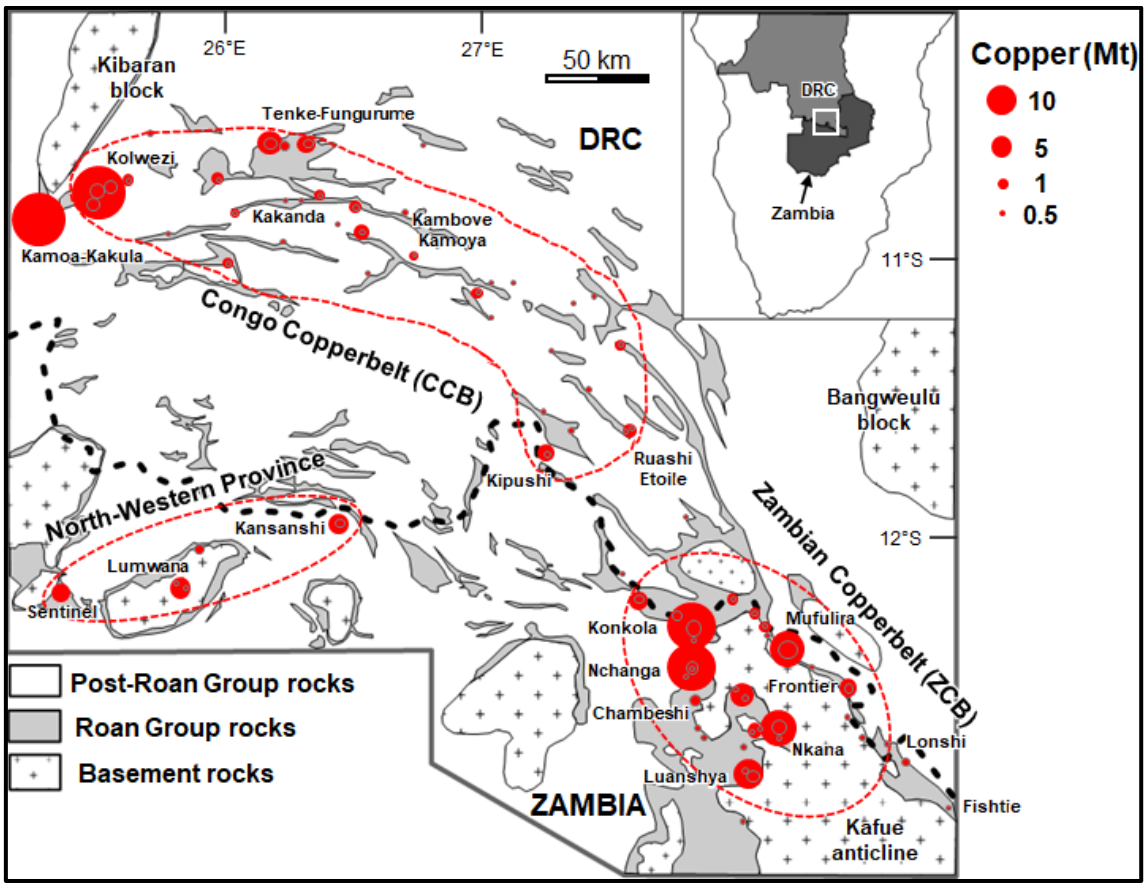

Figure 5: Figure 1.5: Spatial distribution of copper deposits in the Central African Copperbelt (after Selley et al., 2018; copper tonnage data from Hitzman et al., 2017).

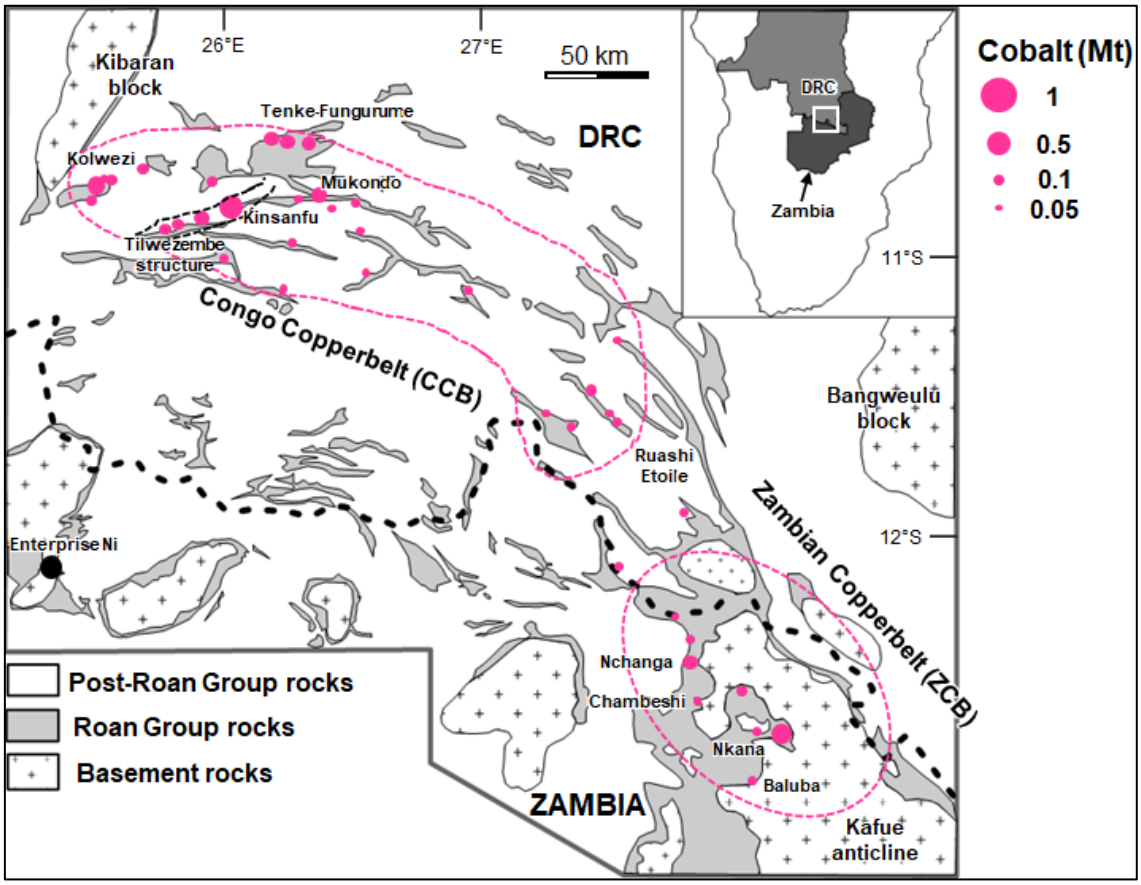

Figure 6: Spatial distribution of cobalt in the Zambian and Congo Copperbelt (after Selley et al., 2018; cobalt tonnage data from Hitzman et al., 2017).

The genetic model of Mendelsohn (1962) for the ZCB deposits suggested that both copper and cobalt is derived from weathering and erosion of basement granitic rocks. The metals were transported in solution to the adjacent basins by rivers and deposited in the sedimentary sequences of the Katanga Supergroup. They attribute localised high-grade copper and cobalt ores in deposits of the ZCB to erosion of orebodies hosted in the granites and subsequent deposition in the Katanga basin (Wakefield, 1978). The lack of evidence for granite hosted orebodies today was explained to suggest a total destruction during erosion. The presence of thick sequences of sandstone and Conglomérat in the ore zone proximal to the basement in the ZCB deposits is regarded as evidence for the eroded granite hosted orebodies (Wakefield, 1978). The sediment provenance of sandstone and Conglomérat consisting of K-feldspar, biotite/ phlogopite and muscovite are said to be igneous in origin derived from the alkali granite/ granitoid,

and possibly similar to the source rocks for Fe-Cu-Co-U±Au mineralization of the Ernest Henry and Olympic Dam deposits in Australia (Theoron, 2013). A granitic source for copper and cobalt ores in the ZCB is said to be further supported by the low nickel enrichment relative to cobalt. According to Davidson (1962) the ranges for the Co:Ni ratios of 2.5:1 - 25:1, with an average of 16.4:1 proposed for deposits in the ZCB by Darney's (1960) favours a granitic metal source (Davidson, 1962; Darnley's, 1960).

In contrast, Annels and Simmonds (1984) suggest that copper and cobalt in the ZCB deposits could have been derived from rocks of basic composition because geochemical evidence shows that cobalt is enriched in ultramafic and mafic rocks and depleted in felsic rocks (Table 1). However, the lack of nickel enrichment in the ZCB deposits has been used to refute suggestions that ultramafic and mafic rocks are possible metal sources.

Table 1 Clarkes for igneous rocks (ranges of quoted values)

	Ultramafic	Mafic	Intermediate	Felsic
Cu (ppm)	10 - 20	87 - 100	85	10 - 30
Co (ppm)	150 - 200	45 - 48	10	1 -7
Ni (ppm)	2000	160 - 2130	55	4 - 15
Co/Ni	0.08 - 0.1	0.02 - 0.28	0.18	0.22 - 0.63
Cu/Co	0.07 - 0.1	1.8 - 2.2	8.5	4 - 10

A review of the sulfide deposits associated with ultramafic and mafic rocks in the Sudbury basin by Naldrett (1981) has shown that Cu:Cu+Ni ratios are generally low, i.e., close to 0.5. Also, that though the Cu:Co ratios (1.76 – 48.18) are in the range quoted for the ZCB deposits, the Co:Ni ratios are very low (~0.03). Hence, it seems that a problem with ultramafic and mafic rocks being the source for copper and cobalt in the ZCB deposits remains with the high nickel concentrations expected from magmatically derived sulfides.

To explain possibility of an association of low nickel concentration with ultramafic and mafic rocks, Annels and Simmonds pointed that Naldrett (1981) analysed rocks that formed from undifferentiated komatiitic magma or tholeiitic magma at an early stage in their differentiation. They report that early precipitation of sulfides from ultramafic magma, caused by assimilation of siliceous material as suggested by Irvine (1975)

together with the crystallisation of olivine, would preferentially reduce the amount of nickel remaining in the residual magma. Early sulfide precipitation would only be possible if the magma became saturated in sulfur by assimilation of isotopically heavy sulfur from an external crustal source. But, early sulfide precipitation by addition of sulfur to the melt would also cause precipitation of copper and cobalt with the nickel reducing the total metal available for enrichment in later ferrogabbroic differentiates. Preferential precipitation of copper at this early stage would also reduce the Cu:Co ratio in these later differentiates.

An alternative explanation for the association of low nickel concentration with mafic or ultramafic rocks can be deduced from the behaviour of copper, cobalt and nickel at various stages in the fractionation of a basic magma to which there has not been significant addition of sulfur or silica (Annels and Simmonds, 1984). The work of Wager and Mitchell (1950) and Wager et al. (1957) on the differentiation of the Skaergaard intrusion in Greenland perfectly illustrates this association (Fig. 7). From figure 1.7 it is evident that, should residual hydrothermal fluids be trapped from the magma during crystallization of ferrogabbros, high concentrations of copper and cobalt are likely to occur together with low concentrations of nickel. The average Cu:Co value at this stage would be close to 25:1, but could reach 44:1, while the Co:Ni ratios show a wide range from 2.5:1 to in excess of 30:1. According to Annels and Simmonds (1984), another example of a relative enrichment of cobalt over nickel, with a Co:Ni ratio of 5.33:1, is reported by Travis et al. (1971) from ferrogabbros of Unit 7 of the Golden Mile Dolerite in Australia. These values are quite similar to those quoted for the ZCB deposits.

There thus appears to be no case for rejecting a basic magma source for cobalt on the basis of the paucity of nickel in the ZCB deposits. High level intrusion of magma at an advanced stage of differentiation could therefore provide the source of the metals which later found their way to even higher levels in the crust. The lack of sufficient basic intrusive/ extrusive material in the basement, from which the metals could be concentrated by weathering, favours a deep-seated hydrothermal origin (Annels and Simmonds, 1984).

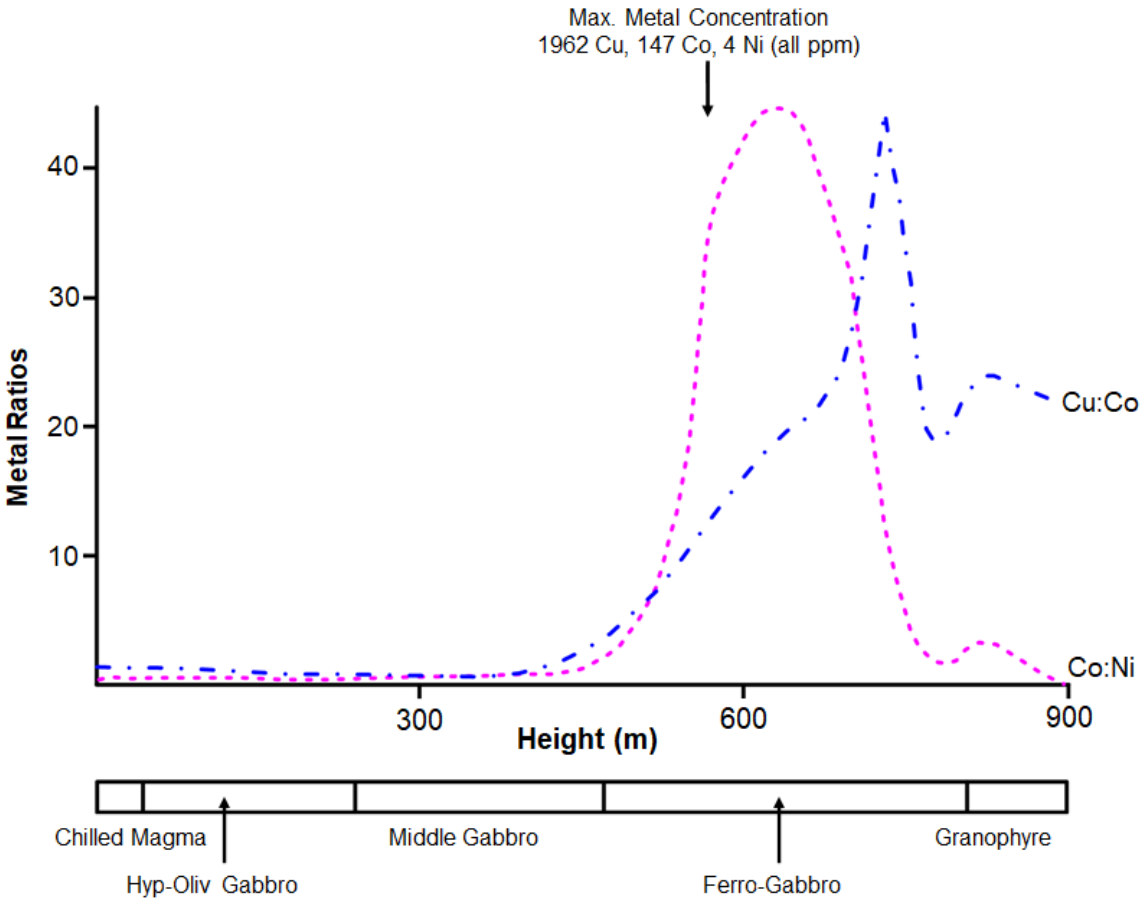

Figure 7: Cu:Co and Co:Ni ratios within the Skaergaard differentiation sequence (after Annels and Simmonds (1984).

A basic metal source for copper and cobalt in the ZCB deposits is also supported by the occurrence of abundant mafic intrusions in the western side of the Kafue anticline of the ZCB where cobalt is extracted as a by-product of copper mining operations (Hitzman et al., 2017). However, Hitzman et al. (2017) concluded that the importance of these mafic intrusions as potential metal sources still remains unproven.

The occurrence of cobalt in the ZCB shows a spatial distribution which is best seen when the deposits are categorized into arenite and argillite-hosted. The argillite-hosted deposits such as the Baluba deposit, exhibit a general lateral distribution where the cobalt orebody is enclosed within the copper orebody (Fig. 8). On the contrary, arenite-hosted deposits e.g., at Lubambe (Konkola North) mine, have a cobalt orebody at the margin of the copper orebody. The vertical distribution of copper and cobalt at both arenite and argillite-hosted deposits exhibits a general inverse relationship. Although the

reasons for the spatial distributions have not been fully investigated in most of the deposits, they are thought to be controlled by variations in the source rocks, host rock, primary porosity, and availability of sedimentary sulfur (Annels and Simmonds, 1984; Annels et al., 1983).

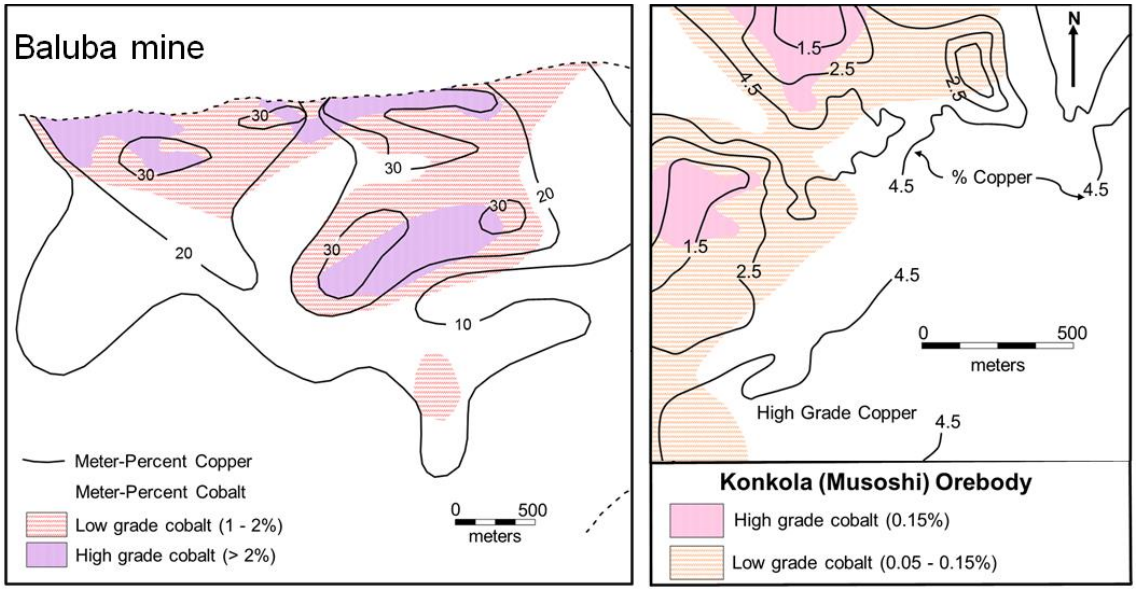

Figure 8: Section and plan view of the Baluba and Konkola deposits showing the lateral distribution of copper and cobalt grade shells. At Baluba mine, the cobalt orebody lies within the copper orebody, while at Konkola the cobalt orebody lies at the margin of the copper orebody (after Annels and Simmonds, 1984).

The second highly debated topic in the CACB and the ZCB in particular, is the timing of mineralization. Several genetic theories explaining the source of the metals and timing of mineralization have been proposed for the ZCB deposits. Among them the epigenetic, syngenetic, diagenetic and metamorphic models, are the most common. These genetic models are developed on the basis of style and occurrence of the copper sulfide minerals.

The epigenetic model which was advanced in the early years of mining suggested that the source of mineralization in the ZCB deposits was hydrothermal fluids that are associated with granites, granodiorites and tonalites present in the basement (Sweeney et al., 1991). According to Sweeney et al. (1991), evidence for a hydrothermal source of mineralization presented in the epigenetic theory (Gray, 1929; Davidson, 1931; Jackson,

1932) included the presence of copper sulfide veinlets in some of the granites located in the ore zone, occurrence of thick bornite-chalcopyrite vein at the base of the Ore Shale at the Chambishi deposit which was interpreted as a pegmatite, presence of aplite and granite sills intruding the lower Katanga metasediments and the observation of white porphyroblasts in the Ore Shale that were originally thought to be the contact metamorphic mineral cordierite. In addition, veinlets in the Nchanga Red Granite were found to contain chalcopyrite associated with fluorite (Jackson, 1932), apparently providing further evidence for a hydrothermal origin of the ores (Garlick and Fleischer, 1972). However, the epigenetic model was discarded due to the unconformity that was observed between the granite and the Katanga sequence metasediments (Schneiderhohn, 1932). After noticing similarities between the CACB deposits and deposits of the Germany Kupferschiefer, Schneiderhohn (1937) formulated a metallogenic model that encompasses what is now called the syngenetic and the diagenetic model.

The syngenetic model relates mineralization to the simultaneous input of sediments and metal ions by rivers into the marginal marine environments (Fig. 9). A wealthy of evidence was presented by Garlick and Fleischer (1972) to substantiate the syngenetic model. These include: (i) the observation of abundant pre-folding sulfide minerals at the Nkana deposit in drill cores; (ii) the lack of correlation between copper content, degree of fracturing, and lithology of high porosity was considered proof against hydrothermal fluid migrations; (iii) the presence of sulfides along foresets of cross-bedding, in troughs of ripples, and along shale laminae, where the size of sulfide grains correlates with the clast size of the sediments was considered proof of syn-sedimentary deposition; and (iv) presence of pre-consolidation slumping of sulfide-bearing sediments at the Mufulira deposit and a reworked sulfidite (a rock made up almost entirely of sulfide minerals) horizon at the Chibuluma deposit were taken as clear evidence of a pre-lithification origin of the ore.

Since the introduction of the syngenetic model, a number of modifications have been made to account for sulfide occurrences in arenites, a feature which is difficult to explain by chemical precipitation in a reducing environment. For instance, Theron (2013) points to the strong sedimentological and lithological control on the distribution of sulfides in the ZCB deposits to suggest the reduction of evaporitic sulfates to reduced

H_2S- and CO_2-bearing pore fluid in the host rock. These were subsequently mixed with an oxidizing copper and cobalt bearing brine derived from the underlying footwall rocks at low temperatures ranging from 100-200°C to precipitate the sulfides in a zonal pattern (Fig. 10).

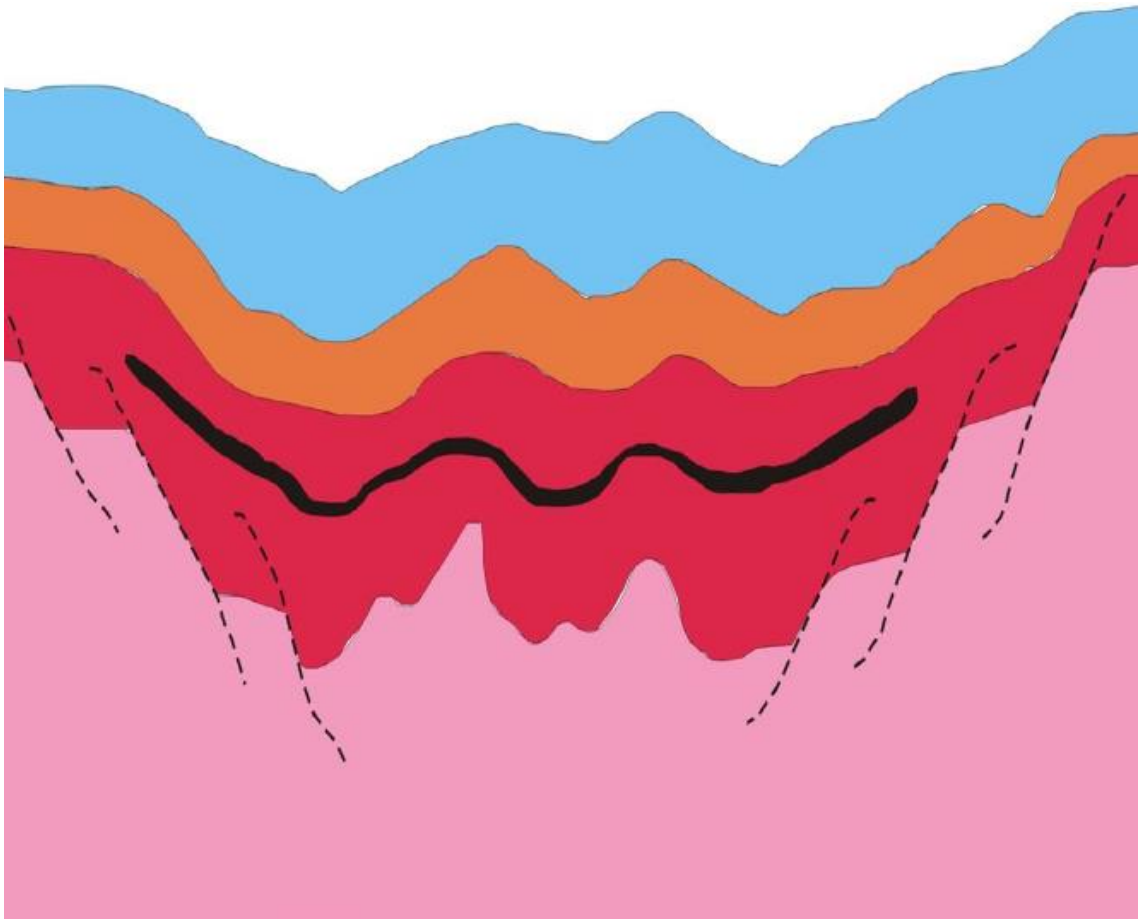

Figure 9: Schematic diagram of the syngenetic model illustrating the pre-folding emplacement of the stratiform copper and cobalt ores in the Katanga basin to form the Zambian Copperbelt deposits (after Cailteux et al., 2004).

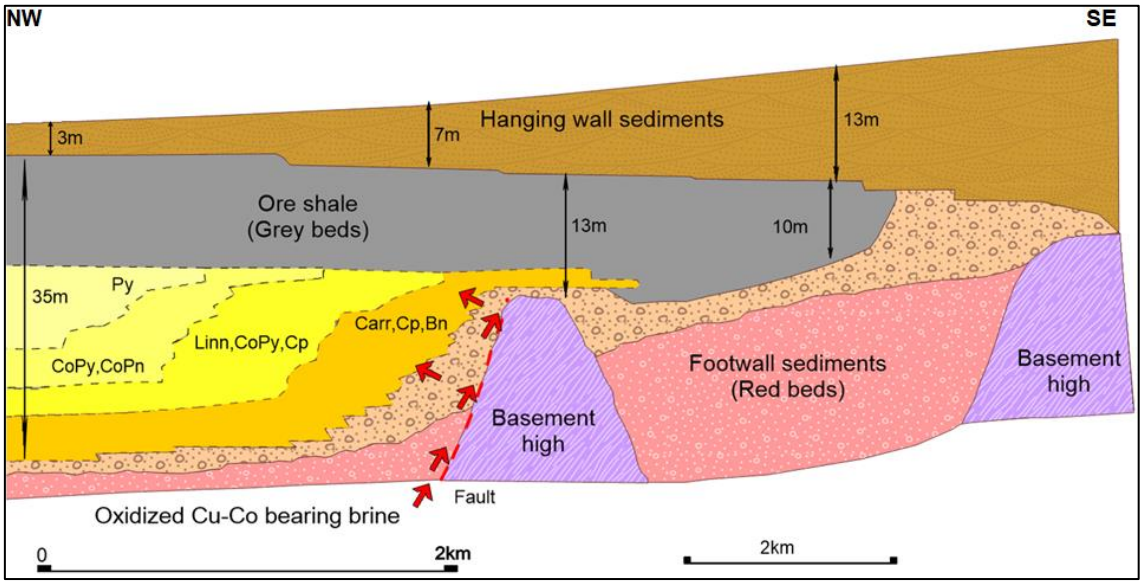

Figure 10: Block model of the basement-proximal ZCB and the footwall oxidized red beds sediments lapping onto granitoid basement. These granitoids are in some places known to contain alkali-granitoid-related Iron-Oxide Copper-Gold (IOCG) deposits, which were a possible primary source of the Cu, Co, and U (after Theron, 2013).

The low endowment of copper and cobalt in the basement rocks raised some gaps in the syngenetic origin of the ZCB deposits. As suggested by Annels (1974) and Raybould (1978), Katanga sedimentation took place in an intracratonic rift bounded by the Kafue anticline. There would therefore, be a possibility of an introduction of copper and cobalt in the sediments through hydrothermal solutions at various stages. Hence, the diagenetic model which envisages the leaching of metals from the sedimentary pile during red-bed diagenesis was developed (Walker, 1976; Holmes et al., 1983; Brown, 1984). The hydrothermal fluids could be related to deep seated magma or derived from the compaction of the sedimentary pile during diagenesis. In the Hitzman et al. (2010) model, the basement of the ZCB deposits consists of a thick sequence of continentally-derived, coarse grained and oxidized siliciclastic sediments (red beds) that deposited during rift initiation and are overlain by deeper marine or lacustrine silts and shales (Fig. 11). The copper deposits are capped by a thick carbonate sequence and contain variable evaporitic strata. In the diagenetic model, copper and cobalt are sourced from iron oxide and oxyhydroxide coatings around sediment grains in the red bed sequences, metamorphosed basement rocks and the bimodal igneous rocks intruding the basement. Moderate to high saline oxidized brines transport metals along basin margins or

basement highs, primarily as chloride complexes. The origin of these saline brines is twofold: residual brines generated from evaporation of basin fluids and melting of evaporites which form the carbonate seal. Metals precipitated as copper sulfides through interactions with an insitu reductant (e.g., diagenetic pyrite or bacterially reduced sulfate) via a chemical reaction shown in Equation 1.1, or a mobile reductant such as mixing of an oxidized sulfate-bearing fluid with trapped hydrocarbons that accumulated in structural or stratigraphic traps, as shown in Equation 1.2.

$$2CuCl_3^{-2} + S^{2-} = Cu_2S + 6Cl^- \qquad \text{(Equation 1.1)}$$

$$2CuCl_3^{-2} + SO_4^{2-} + CH_4 = Cu_2S + CO_2 + 2H_2O + 6Cl^- \qquad \text{(Equation 1.2)}$$

The importance of the evaporites in the formation of sediment-hosted copper deposits is strongly emphasised in the diagenetic model. For instance, the spatial distribution of the sediment-hosted copper deposits globally to within 30° of latitude from the palaeoequator is attributed to the requisite presence of evaporites which provided a long-lived, hydrologically closed system in intracontinental rift basins (Hitzman et al., 2010). According to Hitzman et al. (2005), the evaporites not only provide a source of dense, saline brines for the system, but also act as a regional aquiclude, helping to seal ore fluids within the basin. Dissolution or rupturing of evaporitic seals during basin inversion has been proposed as a mechanism by which ore fluids may be focused into areas containing reductants at higher stratigraphic levels (Hitzman et al., 2005; Hitzman et al., 2010).

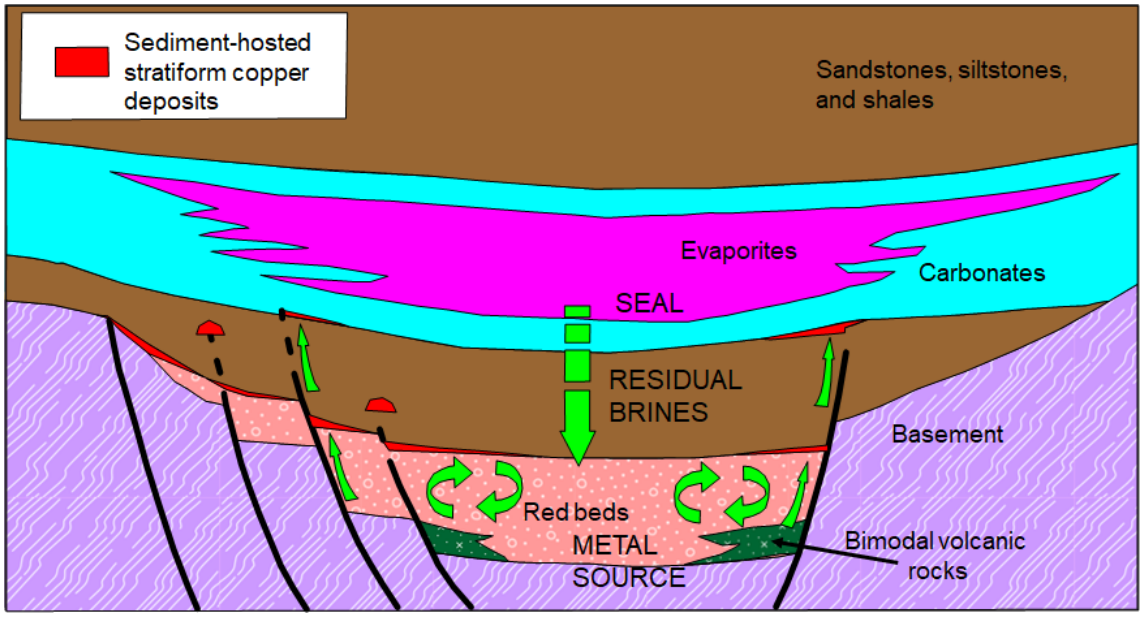

Figure 11: Schematic cross-section through a typical sedimentary sequence in an intracratonic basin capable of generating sediment-hosted copper deposits. Copper is sourced from the syn-rift red beds, bimodal volcanics and/or basement lithology. Reduced, organic-rich siltstones and mudstones provide a redox trap for oxidized metal-bearing brines. Heat from burial and/or igneous activity drives brine migration along basin margins, basement highs and deep-seated rift-related fault structures into structural or stratigraphic traps, with evaporites forming an effective seal (after Hitzman et al., 2010).

The presence of a bulk of structurally controlled copper and cobalt mineralization in the ZCB deposits led to the development of the metamorphic model. Structural control of mineralization in the ZCB deposits is of two kinds. The first structural control suggest that folds determine the occurrence of the Roan Group rocks that host the stratiform copper and cobalt deposits near the surface or at a depth accessible to mining. The second structural control suggest that faults determine the location of the major vein orebodies (Unrug, 1988). Unrug (1988) pointed that the association of vein mineralization with late faults that postdate folding and formation of the thrust sheets, indicates the presence of an appreciable volume of fluids in the basin after the main Lufilian orogeny. The major significance of faults reactivated during basin inversion (Lufilian orogeny) has been proposed at Nchanga deposit by McGowan et al. (2006) (Fig. 12). These structures did not only play a vital role in the late-stage vein mineralization but also in the later remobilization of the mineralization which took place

at higher temperatures during metamorphism and tectonism related to the Lufilian orogeny (Theron, 2013).

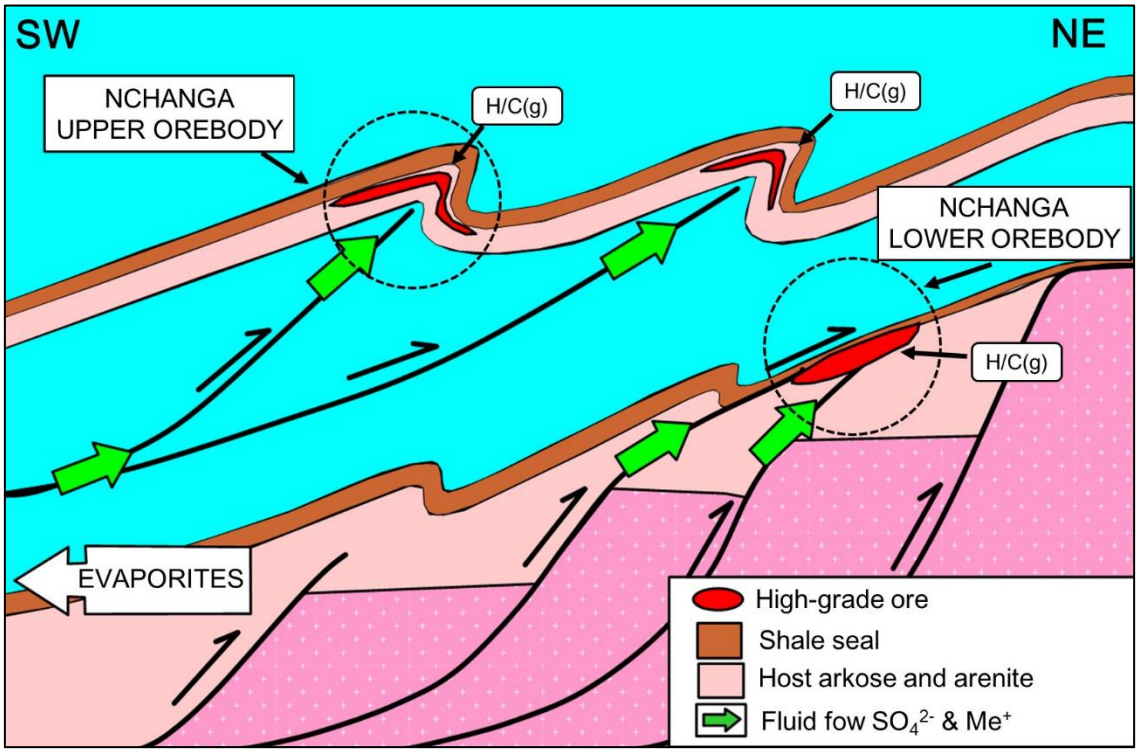

Figure 12: Schematic fluid-flow model for mineralization during basin inversion and thrust-fold development of host sequence. Me^+ is metal ions, i.e., Cu^+ and Co^{2+}.

1.3 Previous Research

A study by Hendrickson et al. (2015) described different types of hydrothermal alteration that affected lithology at the structurally controlled copper-rich Fishtie deposit. These include an early iron mineralization assemblage of magnetite, ankerite and apatite, which was overprinted by three stages of hydrothermal alteration mineralization of biotite, muscovite and chlorite. The authors observed that the iron mineralization is intensively developed towards normal faults suggesting that they formed conduits for iron-rich hydrothermal fluids. The early biotite and K-feldspar alteration is overprinted by muscovite alteration which is in turn replaced by chlorite alteration. Unlike what is reported at Nkana-Mindolo and other deposits in the ZCB where K-feldspar alteration is closely related to copper and cobalt mineralization,

Hendrickson et al. (2015) observed that the early biotite and K-feldspar alteration at the Fishtie deposit does not show close relationship to copper mineralization. Instead, the copper sulfide mineralization at the Fishtie deposit is temporally associated with chlorite mineralization.

A regional review of the deposits in the CACB indicates a clear zonation of metal association/ location and alteration domains (Fig. 13). In the extreme northwest and southeast of the CACB the metal commodity is copper dominant (area labelled yellow in Fig. 13). Between these zones runs a long belt of copper and cobalt deposits (brown region in Fig. 13) connecting the ZCB and CCB, with a small region of copper and cobalt deposits (dark blue area in Fig. 13) enclosed within this belt in the CCB. In the southern portion of the CACB in the domes region (blue area in Fig. 13), the deposits are copper and uranium rich and may contain other metals like molybdenum, gold and nickel. Between the copper-cobalt zone and the domes region, zones of metal associations nickel-uranium, zinc±lead and massive iron replacement are observed.

The alteration is zoned in a similar manner. The alteration footprint in the CACB involves removal of albite and addition of magnesium and potassium (Halley et al., 2016). In the copper dominant regions, the alteration is typically massive potassic alteration. In the rest of the CACB the alteration signature involves addition of magnesium and, in some places, it overprints potassic alteration. Halley et al (2016) suggest that the alteration mineral assemblages formed during hydrothermal activity are dependent on the temperature of the hydrothermal fluids and the primary composition of the host rocks. In high-temperature systems such as at Trident deposit, the addition of potassium and magnesium forms phlogopite and kyanite. However, in quartz-rich rocks with low Al content, talc is more stable than phlogopite. In lower-temperature systems, potassium feldspar is formed rather than phlogopite, and addition of magnesium is manifested as magnesium rich chlorite. The magnesium rich carbonate minerals such as dolomite and magnesite, tend to be more common at lower-temperature systems rather than magnesium silicates.

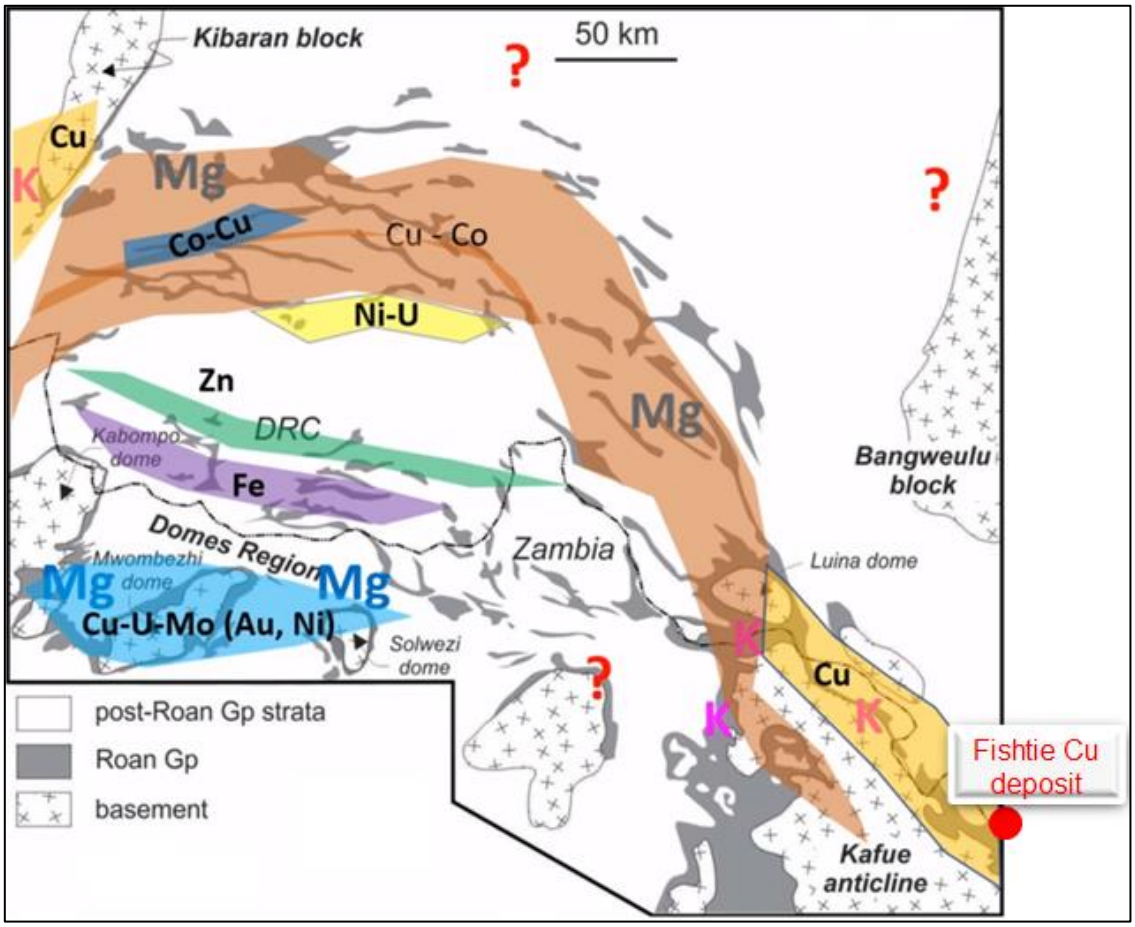

Figure 13: Geological map of the Central African Copperbelt (CACB) showing metal associations/ locations and the hydrothermal alteration domains in the Katanga basin (after Selley et al., 2018).

1.4 Research Objectives

As earlier alluded to, cobalt is extracted as a by-product of copper mining in the ZCB and the rest of CACB, except for a few deposits in the CCB which host supergene cobalt-rich ores (Hitzman, 2012). However, the occurrence, distribution and association of cobalt with copper in the ZCB presents exploration, mining and metallurgical challenges. From the mining and exploration perspective, challenges associated with developing cobalt deposits emanate from the spatial distribution and the fact that cobalt enriched zones do not always correspond to that of copper enriched zones.

The complexity of cobalt mineralogy presents a challenge during metallurgical processing of ore. The cobalt mineralogy in the ZCB deposits is complex with the majority of cobalt being incorporated in the sulfide minerals such as linnaeite ($Co^{2+}Co^{3+}{}_2S_4$), carrollite ($CuCo_2S_4$), cobaltite (CoAsS), cattierite (CoS_2), cobalt pentlandite (Co_9S_8), siegenite $(CoNi)_3S_4$, and rare cupriferous mattagamite whose composition has been determined by Simmonds (1980) as $(Co_{12}Cu_{28})$ $(Te_{99.4}S_{0.6})_{2.13}$.

Supergene cobalt ores associated with manganese oxide ores often cap the sulfide cobalt orebody at most deposits in CCB. These supergene cobalt ores have an advantage during exploitation because unlike sulfide ores like carrollite and cobaltite, which are deep orebodies and fatal to mining because of pollution, they are shallow deposits and more environmentally friendly. The anomalous concentration of cobalt in the weathered zone at Fishtie deposit, suggests a possible concentration of supergene ores.

This study is aimed at investigating the role of the host lithology in the formation of copper and cobalt mineralization at the Fishtie deposit. The issues that will be addressed by the project include the following:

1. The sources of metals, especially copper and cobalt.
2. The source of sulfur.
3. The timing of copper and cobalt mineralization.
4. The physical and chemical conditions that controlled the precipitation of copper and cobalt minerals.

In order to address these issues, the following information is required:

1. Lithostratigraphy of the ore hosting lithology at the Fishtie deposit.
2. Mineral paragenesis of both gangue and ore minerals.
3. Mineral chemistry of alteration minerals to understand the composition and nature of the mineralizing fluids.
4. Sulfur isotopic data to determine the possible source of sulfur.
5. Whole rock geochemical analysis to determine the distribution of copper and cobalt.

Chapter 2 Geological setting

2.1 Regional Geology

Basement rocks at the Fishtie deposit are composed of a sequence of complexly deformed and metamorphosed sedimentary, volcanic and intrusive rocks belonging to the Mesoproterozoic Irumide that stretches from the central part of Zambia to northern Malawi (De Waele et al., 2006; Fig. 14). This belt is composed of schist of the Muva basement rocks, and gneiss, quartzite and phyllite belonging to the Mkushi Gneiss Complex (Stillman, 1965; Fig. 2.1). The Mkushi Gneiss Complex is intruded by an approximately 1.65 Ga granitoid that is seen on satellite and aeromagnetic maps as two major subrounded bodies (De Waele et al., 2003c). The granitoid body located 2.5 km northwest of the Fishtie deposit has a strong magnetic signature, while the intrusion that is approximately 7 km to the southwest of the Fishtie deposit situated in the centre of the Lusale basin has a relatively weak magnetic response (Hendrickson et al., 2015).

The metamorphic rocks at the basement of the Irumide belt are unconformably overlain by metasedimentary rocks belonging to the Katanga Supergroup of Neoproterozoic age, with the Nchanga Red Granite (883 ± 10 Ma, Armstrong et al., 2005) which intrudes the metamorphic basement rocks imposing a maximum deposition age. These sediments deposited in a Mesoproterozoic to Neoproterozoic (1600-542 Ma) rift basin that developed during the breakup of the Rodinia supercontinent (Porada and Berhorst, 2000), within a series of north-northwest trending synclines or subbasins along the margins of basement domes, with the largest example being the Kafue Anticline (Selley et al., 2005).

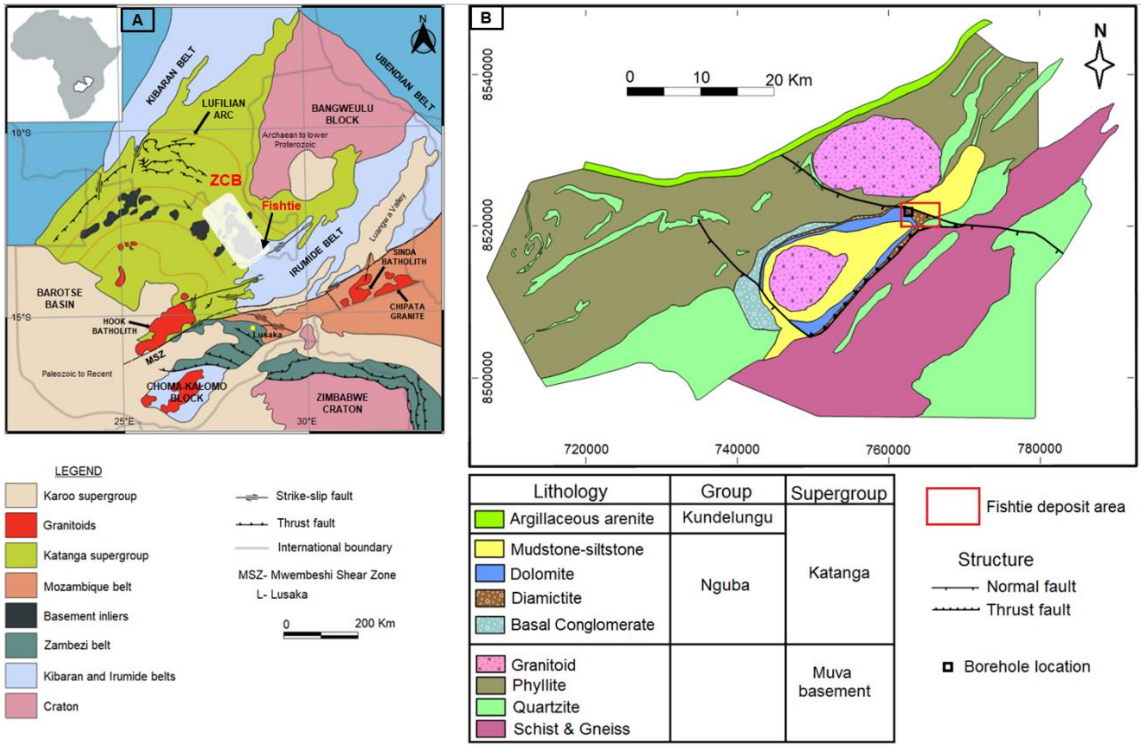

Figure 14: (A) Generalized geological map of Zambia showing the distribution of the rocks of the Katanga Supergroup and the location of the Zambian Copperbelt (ZCB) and the Fishtie deposit. (B) Regional geological map of the Fishtie deposit area showing the different lithological units and the location of the logged boreholes (modified after Master et al, 2005; Geological Survey of Zambia (Stillman, 1965)).

The Katanga Supergroup is an approximately 7 km thick sequence of predominantly continental and marine derived metasedimentary rocks and minor intrusive rocks hosting the majority of the copper and cobalt deposits of the CACB (Selley et al., 2005; Desouky et al., 2010). The Katanga Supergroup is divided into three groups: Roan, Nguba, and Kundelungu (Cailteux et al., 2005; Selley et al., 2005).

The majority of the copper and cobalt deposits in the Zambian Copperbelt are hosted in the Lower Roan Subgroup sequence of the Mindolo Clastics and the overlying Kitwe Formations (Fig. 15). The Mindolo Clastics Formation comprise laterally discontinuous and texturally immature Conglomérats and fining upward sandstones deposited within subbasins in fluvial, alluvial fan and deltaic environments (Selley et al., 2005; Woodhead, 2013). The coarse-grained, continental and oxidized nature of the Conglomérats and sandstones in the Mindolo Clastics Formation is a characteristic of

the ‘red bed’ sequence, where copper is concentrated in iron oxide, oxyhydroxide and clay coatings around siliciclastic grains following diagenetic alteration or destruction of mafic minerals (Rose, 1976).

The Mindolo Clastics Formation are abruptly overlain by a regionally extensive variably organic-rich marginal marine siltstone/ shale termed the Copperbelt Orebody Member, or informally known as the “Ore Shale” of the Kitwe Formation that host the majority of the copper and cobalt orebodies of the Zambian Copperbelt deposits. The Copperbelt Orebody Member is overlain by an approximately 200 m-thick sequence of dominantly cyclical terrestrial siliciclastic sedimentary rocks (Selley et al., 2005).

The siliciclastic rocks of the Kitwe Formation transition upwards into a laterally extensive sequence of dominantly shallow marine carbonates and alternating beds of fining upwards sandstone, siltstone, mudstone, dolomite and algal of the Upper Roan Subgroup (Selley et al., 2005; Woodhead, 2013). The Mwashya Subgroup lies unconformably above the Upper Roan Subgroup comprising mainly deep-water carbonaceous shales, siltstones and clastic carbonate rocks on a marked brecciated base (Cailteux et al., 2007; Bull et al., 2011). The Mwashya Subgroup in the Zambian Copperbelt contains gabbroic intrusions that have yielded ages between 760 ± 5 Ma and 745 ± 7.8 Ma, indicating a period of renewed rifting and related mafic magmatism during this period (Armstrong, 2000; Key et al., 2001; Barron, 2003; Master et al., 2005).

The Roan Group sequences are missing at the Fishtie deposit where the basal unit of the Nguba Group, the Grand Conglomérat unit, directly overlies unconformably the metamorphosed basement rocks of the Irumide belt (Fig. 15). The Grand Conglomérat clast assemblage consists of predominantly subangular clasts of the Upper Roan and Mwashya subgroup rock fragments, indicating significant erosion of the middle part of the Katanga Supergroup (Binda and Van Eden, 1972; Selley et al., 2005). At the Fishtie deposit, the Grand Conglomérat unit comprise a less than 150 m thick sequence of debris flows and diamictite intercalated with thin beds of laminated siltstone and lithic sandstone. The Grand Conglomérat unit has been correlated with the Sturtian diamictites, often associated with a global glaciation event between approximately 750

and 700 Ma (Hoffmann et al., 2004; Hoffmann and Li, 2009; Key et al., 2001; Master et al., 2005).

The stratigraphy overlying the Grand Conglomérat unit comprises 400-500 m thick carbonates and fine-grained siliciclastic rocks of the Kakontwe Limestone unit (Master et al., 2005; Selley et al., 2005; Cailteux et al., 2007).

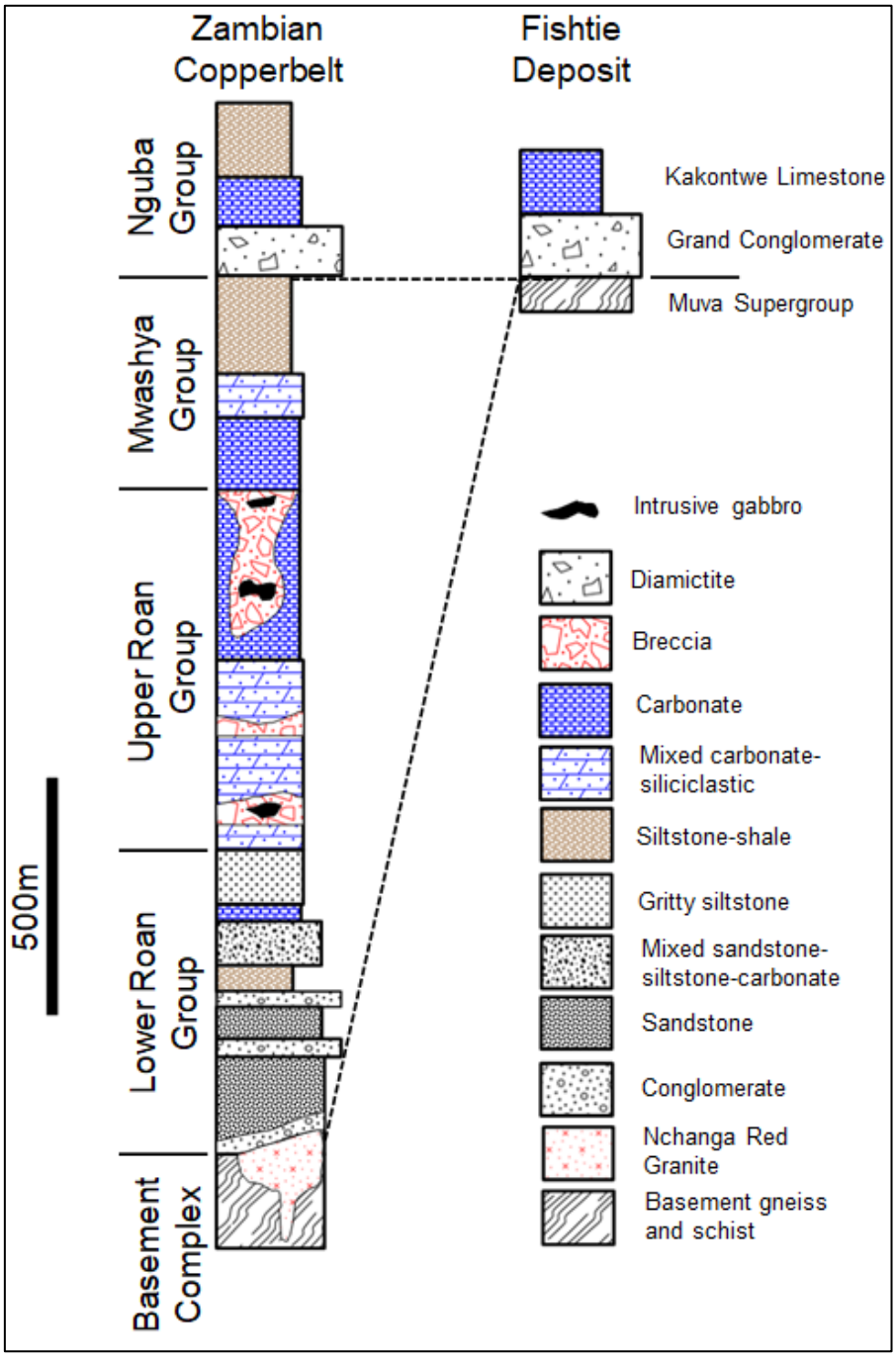

Figure 15: Generalized stratigraphy of the Katanga Supergroup rocks and the correlated lithostratigraphy of the host rocks for the Fishtie deposit (Selley et al., 2005).

Although the fundamental stratigraphic components of the Katanga Basin have been described extensively in the literature, the processes by which the basin formed remain speculative, with contrasting views for either an active syn-sedimentary rifting or more passive subsidence-dominated models being proposed (Kampunzu et al.,

2000b; Mendelsohn, 1961; Selley et al., 2005). A lack of deep marine facies, syn-sedimentary faulting and magmatism in the Lower Roan stratigraphy all indicate the absence of active rifting during early basin formation, with Binda (1994) proposing a more significant role for eustasy. More recent studies have suggested that the basin underwent two main phases of active rifting (Selley et al., 2018). The initial rifting is marked by the oxidised clastics of the Mindola Clastics Formation, with the Copperbelt Orebody Member marking rift climax and marine inundation of the basin, followed by a period of basin starvation, evaporite precipitation and carbonate deposition marked by Upper Roan rocks. The second stage of rifting is marked by the more reduced, shale-dominant lithologies of the Mwashya Subgroup, along with its broadly coeval mafic intrusives and perhaps involved a greater degree of crustal thinning (Armstrong, 2000; Key et al., 2001).

Basin inversion during the Pan-African Lufilian Orogeny produced broad folding and relatively minor reverse faulting throughout the Zambian Copperbelt, with tighter, more extensive folding in the Domes region (Selley et al., 2018). Inversion was accompanied by a thermal event in the Domes region, with peak P-T conditions of 600°C and 700 MPa evidenced in the Kabompo Dome (Meighan, 2015). Peak metamorphic conditions typically produced amphibolite grade rocks in the Domes Region, with greenschist facies assemblages more common in the Zambian Copperbelt (Selley et al., 2005). Where present in the Domes Region, phlogopite, kyanite and Mg-chlorite-bearing metamorphic rocks have recently been reinterpreted as hydrothermal in origin, with the traditional interpretation of high-grade ‘whiteschist’ assemblages, formed through near-isothermal (750°C) decompression during retrograde metamorphism (Cosi et al., 1992; John et al., 2004). In the Zambian Copperbelt, Lufilian folding typically nucleated on earlier normal fault structures which were commonly reactivated, producing net reverse movement (Selley et al., 2018).

Chapter 3 Methodology

This section briefly describes the methods used to meet the objectives of this research project. The methodology is divided into two sections: Field and Laboratory methods (Fig. 16). The field methods involved mainly core logging, observations and sampling. The laboratory works included preparation of powdered samples for X-Ray Diffraction (XRD) analysis, preparation of thin sections for polarising microscopy, Scanning Electron Microscopy – Energy Dispersive Spectroscopy (SEM-EDS), Electron Micro-Probe Analyzer (EMPA) and Raman Spectroscopy. Pure sulfide mineral were separated and prepared for sulfur isotopic analysis.

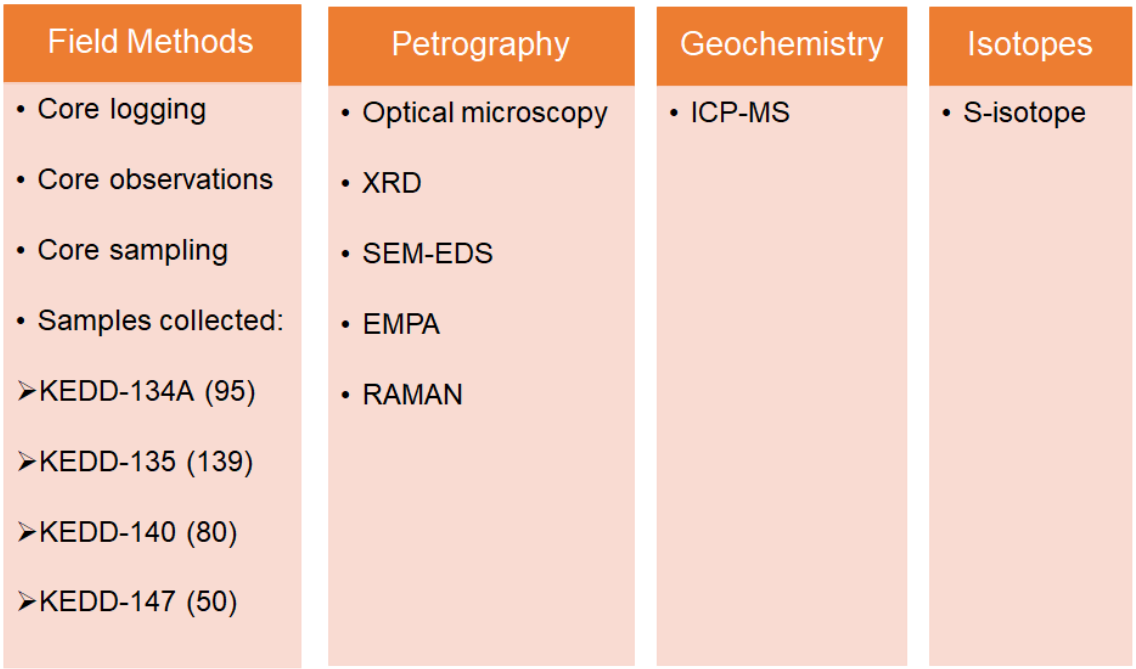

Figure 16: Summary of the field methods and analytical methods used in the research.

3.1 Field work

A desk study was carried out before going for field work in Zambia to understand the geology of the Fishtie deposit and select boreholes to be logged and sampled. The field work was conducted from 12th April to 6th June, 2019.

A down-hole sampling pattern was used in the field whereby samples of about 20 to 30 centimetre in length were collected from four boreholes: KEDD-134A, KEDD-135, KEDD-140 and KEDD-147. These boreholes were selected based on the occurrence of anomalous concentrations of cobalt from assay data. The sampling was done at regular intervals and targeted rock types, lithological contacts, alteration and sulfide mineralized zones. Approximately 100 grams of soil samples were collected from the weathered top portions of the boreholes. A total 95, 139, 80 and 50 samples were collected from boreholes KEDD-134A, KEDD-135, KEDD-140 and KEDD-147, respectively. The samples were couriered to Akita University in Japan in sealed sample bags for laboratory analysis.

3.2 Laboratory methods

3.2.1 X-Ray Diffraction analysis

Selected core and soil samples were prepared as powders at Akita University for X-Ray Diffraction analysis. Samples were crushed to approximately 2mm using an iron mortar and then pulverized to less than 60μm with an agate pestle and mortar.

X-ray diffraction analysis was conducted to identify the bulk mineralogy, especially the clay minerals, in the studied lithologies. X-ray diffraction analysis was conducted using a Rigaku Multi Flex X-ray diffractometer with a scan range of 2° to 60° (2θ) at 0.01° step and 2°/min scan speed, using monochromated Cu Kα (λ = 1.54178 Å) radiation. The voltage and current were set to 30 kV and 16 mA, respectively. Mineral peaks were identified and quantified with the PDXL software using the Reference Intensity Ratio (RIR) method. The RIR method is based upon scaling diffraction data to

the standard material, as discussed in detail in the tutorial: (http://www.icdd.com/resources/tutorials/pdf/Quantitative%20Analysis%20RIR.pdf) by the International Centre for Diffraction Data (ICDD).

3.2.2 Polarizing Microscopy

Petrographic examination was performed at Akita University on polished slides prepared from drill core samples. The mineral assemblages, textures, alteration and ore mineralogy of the host rocks was determined using a Nikon Eclipse E600 POL polarizing microscope.

3.2.3 Scanning Electron Microscopy – Energy Dispersive X-Ray Spectroscopy

Scanning Electron Microscopy – Energy Dispersive X-Ray Spectroscopy (SEM-EDS) (JEOL JSM-6400, EDS; OXFORD Inca Energy System) at Akita University was used to determine the mineral chemistry of alteration and ore minerals, and to confirm textures not readily identifiable with the polarizing microscope.

3.2.4 Raman spectroscopy

The Raman micro-spectroscopy is part of the large category of vibrational spectroscopic methods based on the emission of phonon during relaxation of energy of molecular bonds. This technique can be applied on various materials including organic and inorganic compounds, fluid and gases. Since the technique investigated the structural organisation of molecules of the studied sample, it does not necessary required the material to be crystallized which is suitable in the case of X-ray amorphous carbonaceous materials. The other advantage of Raman micro-spectroscopy during the investigation of mineralized materials is that it provides fast results (commonly few seconds to few tens of minutes) and can be applied directly on fragments (raw samples). A common set of spectrometer, laser and microscope parameters was defined for all our

measurements on polished sections. The instrument parameter used were: laser wavelength of 532 nm, laser power 2 mW, acquisition time of 3 x 10 s (1 s pause between exposures), spectrometer slit of 1000 x 50 µm, 600 gravity spectrometer range of 0-4500 cm^{-1}, spectrum resolution of 9cm^{-1} and objective of 50x long focusing distance. This procedure allowed us to get comparable and reproducible measurements on our samples.

All spectra presented in this paper have been acquired using Renishaw inVia Raman microscope. Calculations were carried out using Bruker Opus software. A series of iterative least-squares curve fittings (Levenberg–Marquant iterative procedure) were made on selected Raman spectra in order to characterize carbonaceous material response in terms of peaks position, surface and relative intensity. Depending on the noise level of the collected spectra, residual RMS error obtained after curve-fitting is typically comprised between 0.5 and 2.

3.2.5 Electron Micro-Probe Analyzer

The chemical composition of chlorite and white-mica group minerals were analysed by electron microprobe analyser (EMPA) at Akita University. Polished thin sections were carbon-coated and analysed with a JEOL-JXA 8230 Electron Probe Micro analyser operating in wavelength-dispersion mode with an accelerating voltage of 15 kV, a specimen current of 50 nA, beam size of 15 µm and counting times on peak and background of 20 and 10 s, respectively.

The following standards were used for Kα and Lα X-ray lines for the elements sought in chlorites and micas: Si, Al: biotite; Fe: andradite; Mg: periclase, Mn: spessartine, Ti: rutile; Cr: chromite, Ni: Ni-olivine, Cu: cuprite, Ca: wollastonite, Sr: SrSO4, Ba: barite, Na, Cl: sodalite, K: orthoclase, F: Durango apatite.

Data were reduced using the XPhi procedure (Merlet 1992). Each sample was analysed on a minimum of two grains, four to five points on each, to check for compositional zoning and to obtain a representative composition.

3.2.6 Whole-rock geochemistry

The data for whole-rock geochemistry was obtained from First Quantum Minerals Ltd. Lithium Borate Fusion method was used to digest the samples. The major and trace elements were analysed by ICP and ICP-MS analysis, respectively. Details of the experimental procedure and calibration methods used can be accessed from Actlabs link; https://actlabs.com/geochemistry/lithogeochemistry-and-whole-rock-analysis/.

Whole-rock chemical analysis was conducted in order to observe downhole enrichment and depletion patterns of elements in the studied boreholes. Major and trace elements were analysed using the method of Code 4LITHO-Quant (11+) Major Elements Fusion ICP(WRA)/Trace Elements Fusion ICP/MS(WRA4B2) which is described on Activation laboratory website; http://www.actlabs.com.

3.2.7 Sulfur Isotopic Studies

Sulfur isotope analysis was conducted at Akita University. 10-20 mg of pure sulfide mineral sample was dissolved in a solution of 20 ml nitric acid and 2 ml bromine at 98°C. The solution was filtered and the filtrate was setup for cation exchange to prepare a solution of sulfide ions. 10 ml of 10% $BaCl_2$ solution was added to the sample solution to precipitate $BaSO_4$. Tin capsules of $BaSO_4$ and V_2O_5 in a ratio of 1:5 was prepared and analysed with ICP-MS. The analysis accuracy was better than ±0.2%.

3.8 Data Evaluation

Data were evaluated using assorted software packages, which include: Xlstat® 2013, Excel® 2013, QGIS 2.6.1., Earthworks® Downhole Explorer and Strater 2 plotting software.

Chapter 4 Results

4.1 Lithostratigraphy of the Fishtie deposit

Lithostratigraphy of the Fishtie deposit was determined from logging of cores (Fig. 17). The boreholes KEDD-134A and KEDDD-135 intersected a metasedimentary sequence of siltstone-mudstone, dolomite and Conglomérat unit. The KEDD-140 borehole intersected the interbedded siltstone-mudstone and dolomite units, while drilling of borehole KEDD-147 ended in the weathered portion.

The top portion of all the boreholes comprises unconsolidated soil and clay-rich zone underlain by saprolite. The soil profile is an approximately 5 m thick layer of light brown kaolinitized quartz pebbles. The clay-rich zone is an extremely weathered horizon consisting of varying proportions of clay minerals such as kaolinite-serpentine and sericite (illite). The clay-rich horizon is also composed of quartz, goethite, calcite, ankerite and siderite. The saprolite forms an approximately 20 m thick horizon of unconsolidated rock fragments with clay-rich patches but the original sedimentary structures of bedding and foliation are preserved. The mineralogy of the saprolite depends on the protolith of the weathered rock but generally consists of quartz, sericite (illite), kaolinite-serpentine, chlorite-serpentine, goethite, calcite, ankerite and siderite. In boreholes KEDD-140, KEDD-134A and KEDD-135, a highly fractured interval of interbedded siltstone-mudstone is observed in the shear zone. The rock fragments of the interbedded siltstone-mudstone in the shear zone are limonitized and sideritic with dark brown stains. Malachite and chalcocite are observed in siderite stockwork veins.

Below the shear zone, a layered interval of interbedded siltstone-mudstone is intercepted (Fig. 17). The siltstone layers are light grey, while mudstone is black, probably suggesting presence of carbonaceous material. A general trend of reverse grading (fining downwards) is observed in this siltstone-mudstone unit. The black mudstone gradationally changes to olive green (Fig. 17). The fining downward (reverse grading) trend changes to a fining upward (normal grading) downhole with a possible fold hinge observed at 48.5 m in borehole KEDD-140 and at 79.5 m in borehole KEDD-

135 (Fig. 17). Below these fold hinges, the lithology alternates between normal and reverse grading and the mudstone changes colour from black to olive green. The interbedded mudstone-siltstone is intercalated with massive dolomite. The Conglomérat unit is intersected at 178.8 m in borehole KEDD-134A and at 177 m in borehole KEDD-135. The true thickness of the Conglomérat unit at Fishtie deposit is difficult to determine from the cores logged because drilling stopped in the Conglomérat unit, but its thickness has been estimated to range approximately from 20 to 150 m (Hendrickson et al., 2015).

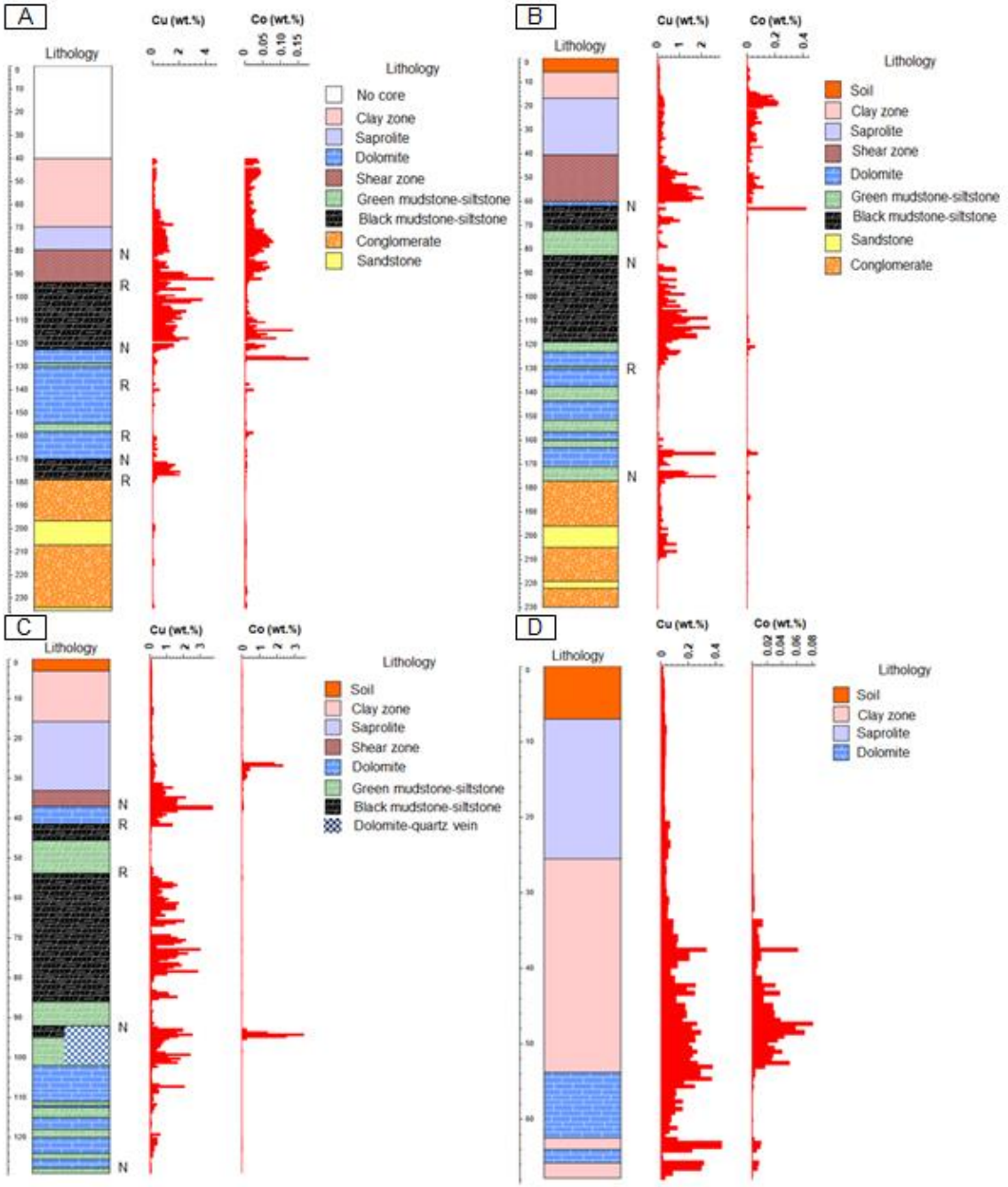

Figure 17: Lithostratigraphy of the host rocks at the Fishtie deposit determined from logging of cores drilled in boreholes; (A) KEDD-134A, (B) KEDD-135, (C) KEDD-140 and (D) KEDD-147. Assay data for copper and cobalt from ICP-MS is plotted against lithology. Abbreviations: N- normal grading, R- reverse grading.

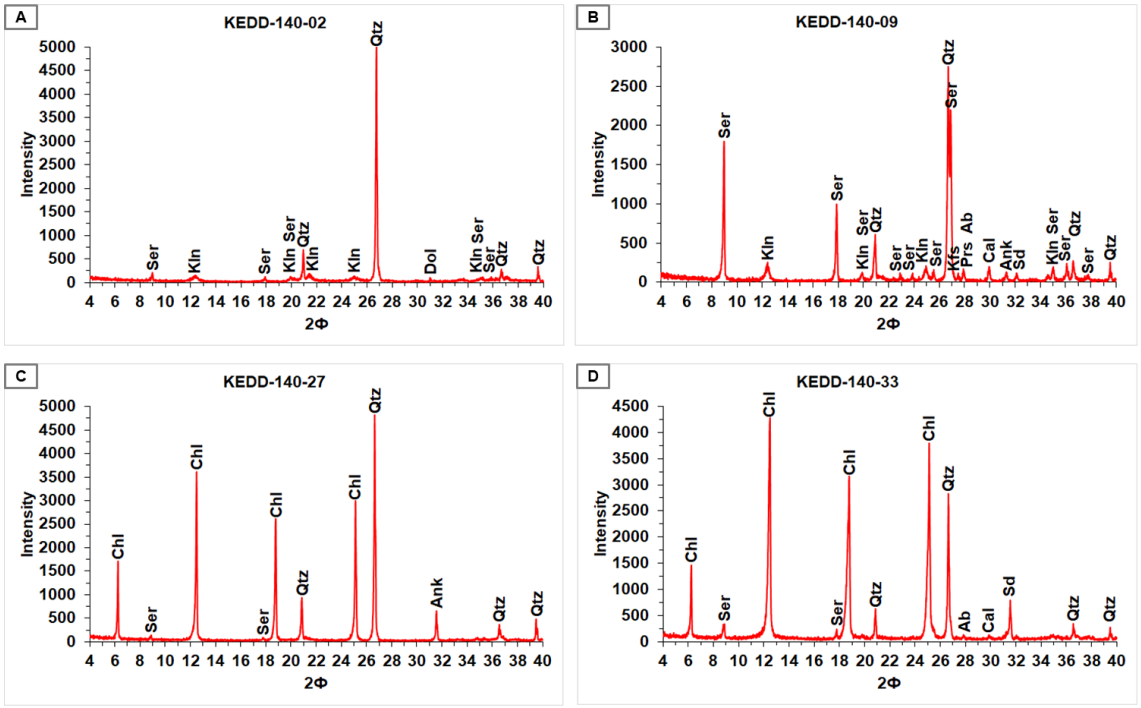

Figure 18: X-Ray Diffraction patterns for samples from; (A) soil (1.15 m), (B) clay zone (9.7 m), (C) saprolite (31 m) and (D) sheared zone (35.8 m) for the borehole KEDD-140. Mineral Abbreviations: Ab- albite, Ank- ankerite, Ca- calcite, Chl- chlorite, Dol- dolomite, Kln- kaolinite, Kfs- K-feldspar, Prs- pyrolusite, Sd- siderite, Ser- sericite.

4.2 Principal lithology

4.2.1 Grand Conglomérat Formation

The Grand Conglomérat Formation is intercepted in boreholes KEDD-134A and KEDD-135, consisting ~55 m thick Conglomérat and sandstone beds (Fig. 17). The Conglomérat ranges from 5 to 30 m in thickness, alternating with thin beds of sandstone. The Conglomérat does not display grading, but it has a massive, light green, matrix-supported texture with clasts constituting about 10-30% of the rock (Fig. 19A). A general increase in the frequency of the clasts is observed from the top to the bottom of the Conglomérat layer. The clasts are angular to subrounded, polymictic, and with no preferred orientation. The clasts range in size from less than 1 mm to greater than 2 meters in diameter. The majority of the clasts in the Conglomérat are derived from quartzite, schist and quartz vein. A few clasts of dolomite, granitoid and mafic rock fragments are also observed in the Conglomérat. The matrix of the Conglomérat changes colour from light green to grey or light brown, reflecting variations in mineralogical composition.

The contact between the Conglomérat and sandstone is either sharp or gradational (Fig. 19B). Sandstone occurs as 5-15 m thick beds (Fig. 19C). The sandstone consists of a homogenous texture, which is either foliated or graded. When the sandstone beds are graded, normal grading is commonly observed.

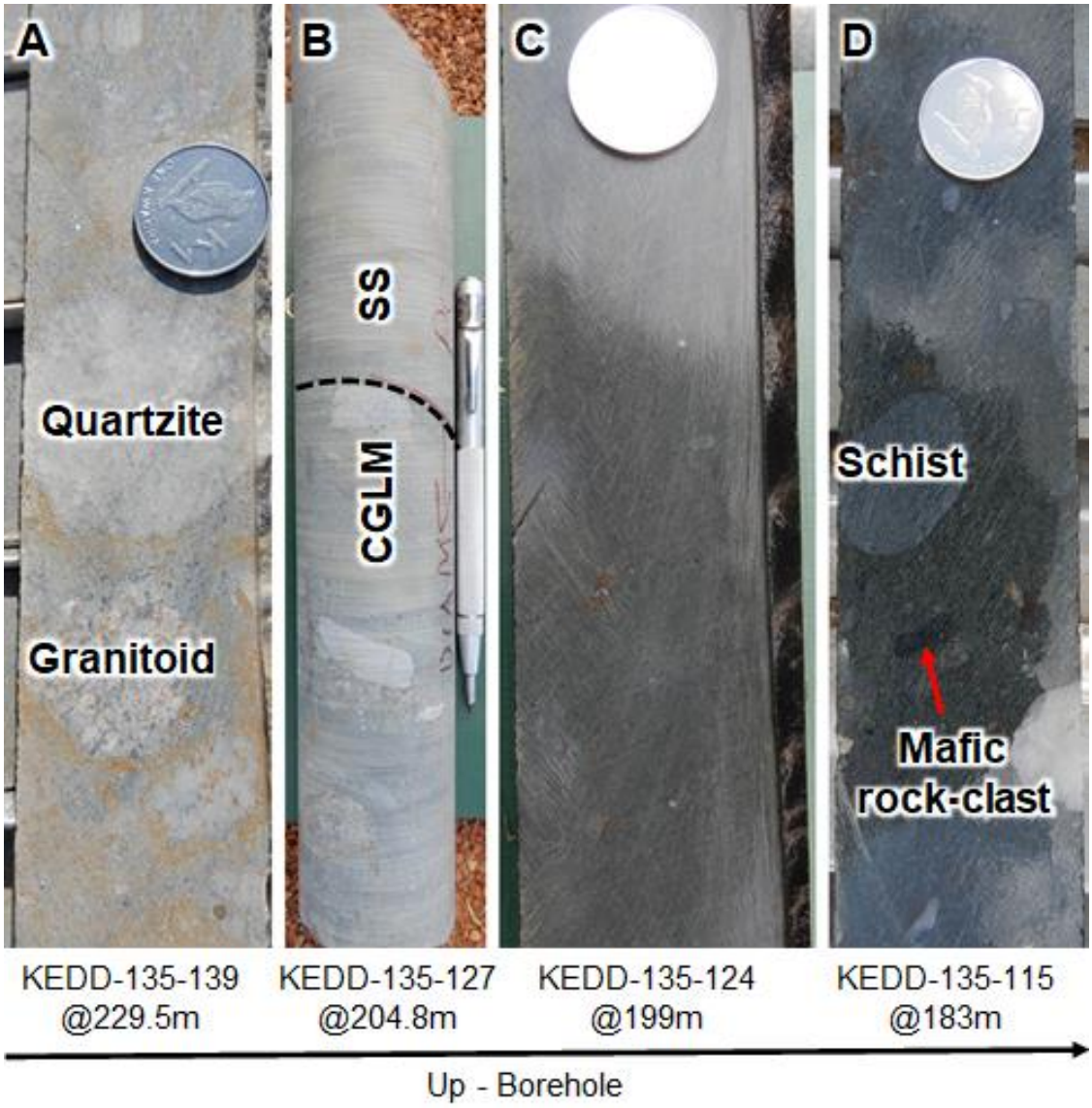

Figure 19: Rock types of the Grand Conglomérat Formation and their textures; (A)light brown Conglomérat comprising of subrounded quartzite and granitoid clasts; (B) sharp contact between Conglomérat and sandstone; (C) light green, fine-grained sandstone bed; (D) light green Conglomérat consisting of angular schist and mafic rock fragment clasts. Abbreviation: CGLM – Conglomérat, SS – Sandstone.

The mineralogical composition of the Conglomérat is best described when the clasts and matrix are considered separately. Granitoid clast consist mainly of quartz, albite, biotite, K-feldspar, muscovite, chlorite and minor calcite (Fig. 20). Quartz and albite grains are subrounded to angular in shape and range from 0.5-1 mm in diameter. Biotite, K-feldspar, muscovite and chlorite occur generally as small subangular to subrounded grains. Clast derived from shist consist mainly of quartz and muscovite.

The angular shaped quartz grains are rimmed by muscovite which display a preferred orientation, probably in the direction of the foliation (Fig. 21B). Hence, the protolith of the schist clast should have been a muscovite schist. Quartzite clasts consist of subrounded to angular quartz grains and fine-grained white mica (sericite) occupying the quartz interstitial spaces (Fig. 21C). Dolomite clasts are massive with chlorite commonly observed replacing the margins of the dolomite grains (Fig. 21D).

The mineralogy of sandstone is similar to the matrix of the Conglomérat. The fine-grained matrix of the Conglomérat and sandstone is composed of quartz, white mica, biotite, chlorite, K-feldspar, dolomite-ankerite (Fig. 22). White mica is the most common phyllosilicate. Fine-grained white mica occurs throughout the matrix but is particularly common adjacent to potassium feldspar grains suggesting that it was formed by replacement of the K-feldspar. Biotite is commonly intergrown with chlorite. Carbonaceous material (dark brown color) is also observed in the matrix of Conglomérat and sandstone. Examination of the carbonaceous material by Raman spectroscopy identified the organic matter as well-ordered graphite, with the graphite peak (or G-band) occurring in the range 1575-1582 cm^{-1} (Raman Shift) (Fig. 23).

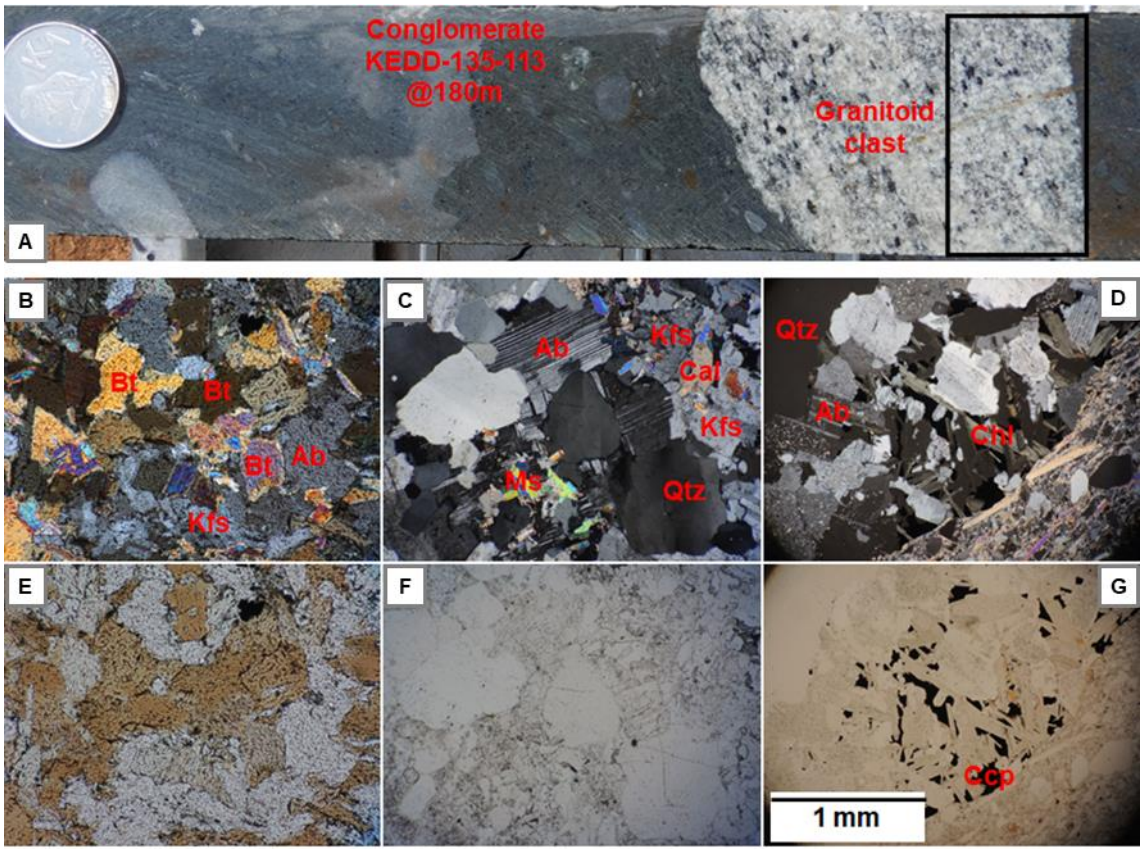

Figure 20: Petrography of granitoid clast; (A) Conglomérat consisting of granitoid clast, rectangle is the part which was cut and polished to a thin section. Plane-polarized photomicrograph of granitoid clast consisting of: (B) intergrown Ab, Bt and Kfs grains, (C) subrounded to angular Qtz and Ab grains, with interstitial Ms, Kfs and Cal, (D) intergrown subrounded to angular Qtz, Ab and Chl. Cross-polarized photomicrograph of granitoid clast showing; (E) same view as in B, (F) same view as in C, (G) same view as in D. Mineral Abbreviations: Ab- albite, Bt- biotite, Cal- calcite, Chl- chlorite, Kfs- K-feldspar, Ms- muscovite, Qtz- quartz.

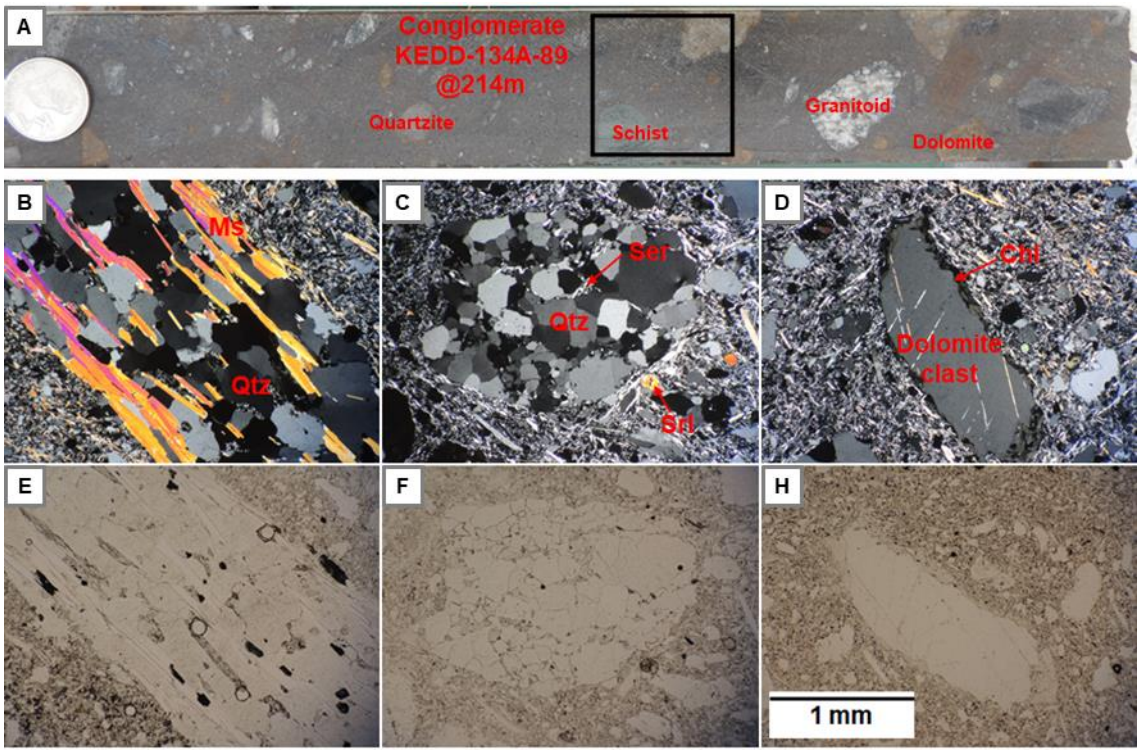

Figure 21: Petrography of schist, quartzite and dolomite. (A) Conglomérat consisting of schist, quartzite, dolomite and granitoid clasts, black rectangle is the part which was cut and polished. Plane-polarized photomicrograph of (B) schist consisting of subrounded to angular Qtz and Ms, Ms display preferred orientation defining the foliation, (C) quartzite clast comprising subrounded Qtz grains and fine-grained white mica (Ser) occur in the interstitial spaces, (D) massive dolomite clast with chlorite replacement in the grain margin. Cross-polarized photomicrograph showing: (E) same view as B, (F) same view as C, (H) same view as D. Mineral abbreviations: Chl- chlorite, Ms- muscovite, Qtz- quartz, Ser- sericite, Srl- schorl.

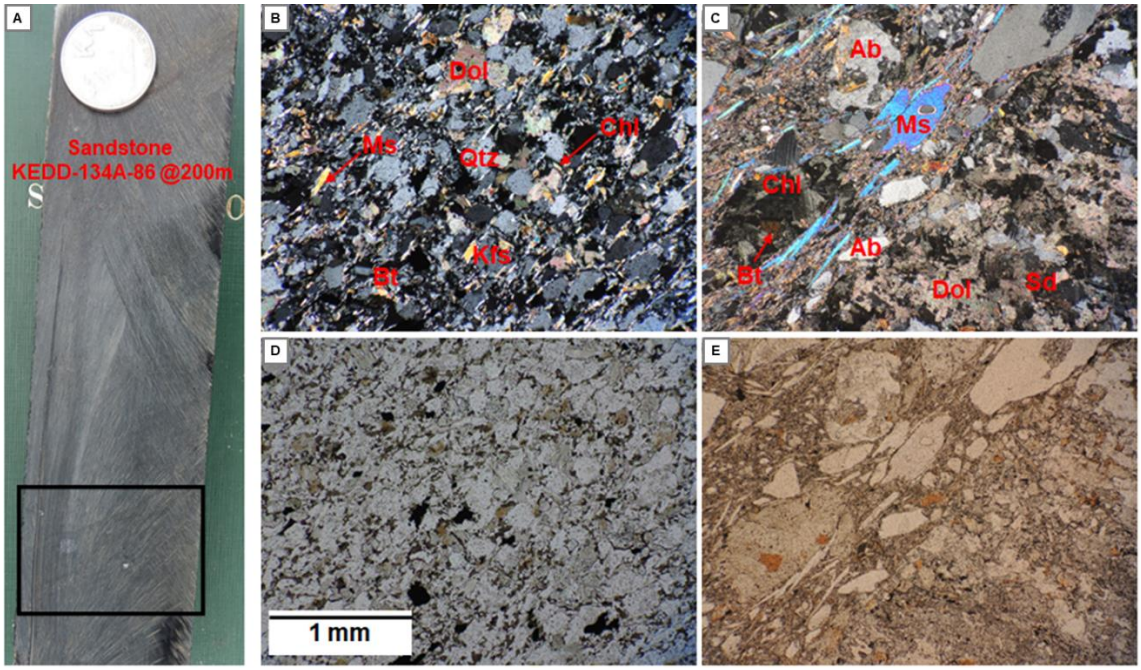

Figure 22: (A) light green fine-grained sandstone, black rectangle is the part which was cut and polished. (B) cross-polarized transmitted light photomicrograph of sandstone showing; Qtz, Bt, Kfs, Ms and Chl dominated clastic-matrix, minor dolomite is observed, (C) Ab, Bt, Ms and Chl in a Dol-Sd dominated matrix. Cross-polarized photomicrograph showing: (D) same view as in B, (E) same view as C. Mineral abbreviations: Ab- albite, Bt- biotite, Chl- chlorite, Dol- dolomite, Kfs- K-feldspar, Ms- muscovite, Qtz- quartz, Sd- siderite.

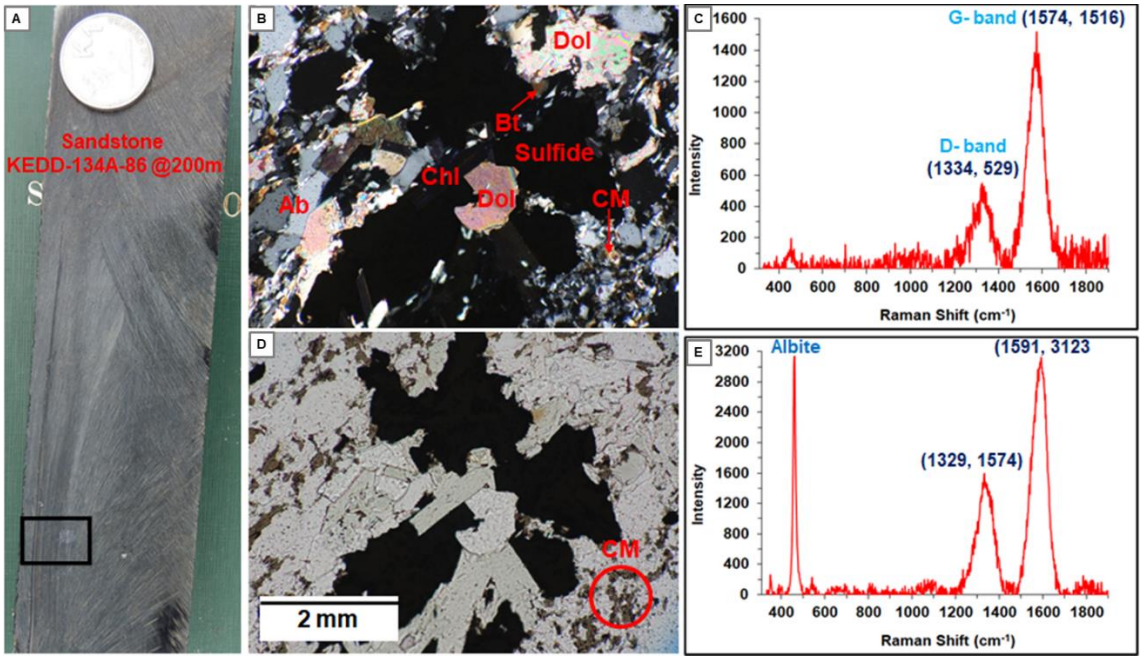

Figure 23: (A) Petrography of sandstone, black rectangle is the part cut and polished to thin section, (B) cross-polarized transmitted light photomicrograph showing Ab, Bt,

Chl, Dol and CM in the clastic-matrix, (C) Raman spectroscopy pattern of graphite showing the positions of the G and D bands, (D) Cross-polarized photomicrograph showing same view as B, (E) Raman spectroscopy of graphite in an albite dominated matrix. Mineral abbreviations: Ab- albite, Bt- biotite, Chl- chlorite, CM- carbonaceous material, Dol- dolomite. Sulfide mineral is chalcopyrite.

4.2.2 Dolomite

Drilling at the Fishtie deposit intersected an approximately 50 m thick massive dolomite unit overlying the Conglomérat unit. The dolomite unit is divided into the lower massive dolomite, bedded dolomite and the upper reprecipitated dolomite. The lower massive dolomite is white, grey, pale-pink color and has medium to coarse-grained, stromatolitic texture (Fig. 24A and B). Vertical to subvertical stockwork veins are often observed cutting the massive dolomite. The stockwork veins in the mineralized zone contain significant disseminated sulfides. The massive dolomite grades to a bedded dolomite in the upper level. Mudstone and siltstone layer several millimetres thick are intercalated in the bedded dolomite. The bedded dolomite is grey to dark grey and fine-grained. The surfaces of the bedded dolomite show a pinstriped, rhythmic texture and is often folded and cut by sulfide bearing stockwork veins (Fig.24C). The upper dolomite occurs just below the clay zone. This dolomite has a distinctively white color and a massive, fine-grained texture (Fig. 24D). The surface of the upper dolomite usually has voids which serve as evidence for dissolution textures. Extreme weathering conditions was responsible for the formation of thick clay zones and reprecipitation of quartz and dolomite layers in the shallow level.

The massive dolomites are composed dominantly of medium to coarse grained dolomite and minor quartz and organic matter (Fig. 25A, C and E). The bedded dolomite consists of alternating dolomite and siliciclastic-rich beds (Fig. 25G and H). The bedded dolomite consists of alternating dolomite- and siliciclastic- rich beds (Fig. 25G and H). The dolomite rich beds consist of medium-grained dolomite, while siliciclastic-rich beds comprise of fine-grained mosaic aggregate of dolomite and minor quartz, and sericite. The upper reprecipitated dolomite consist mainly of fine-grained dolomite and quartz (Fig. 25D).

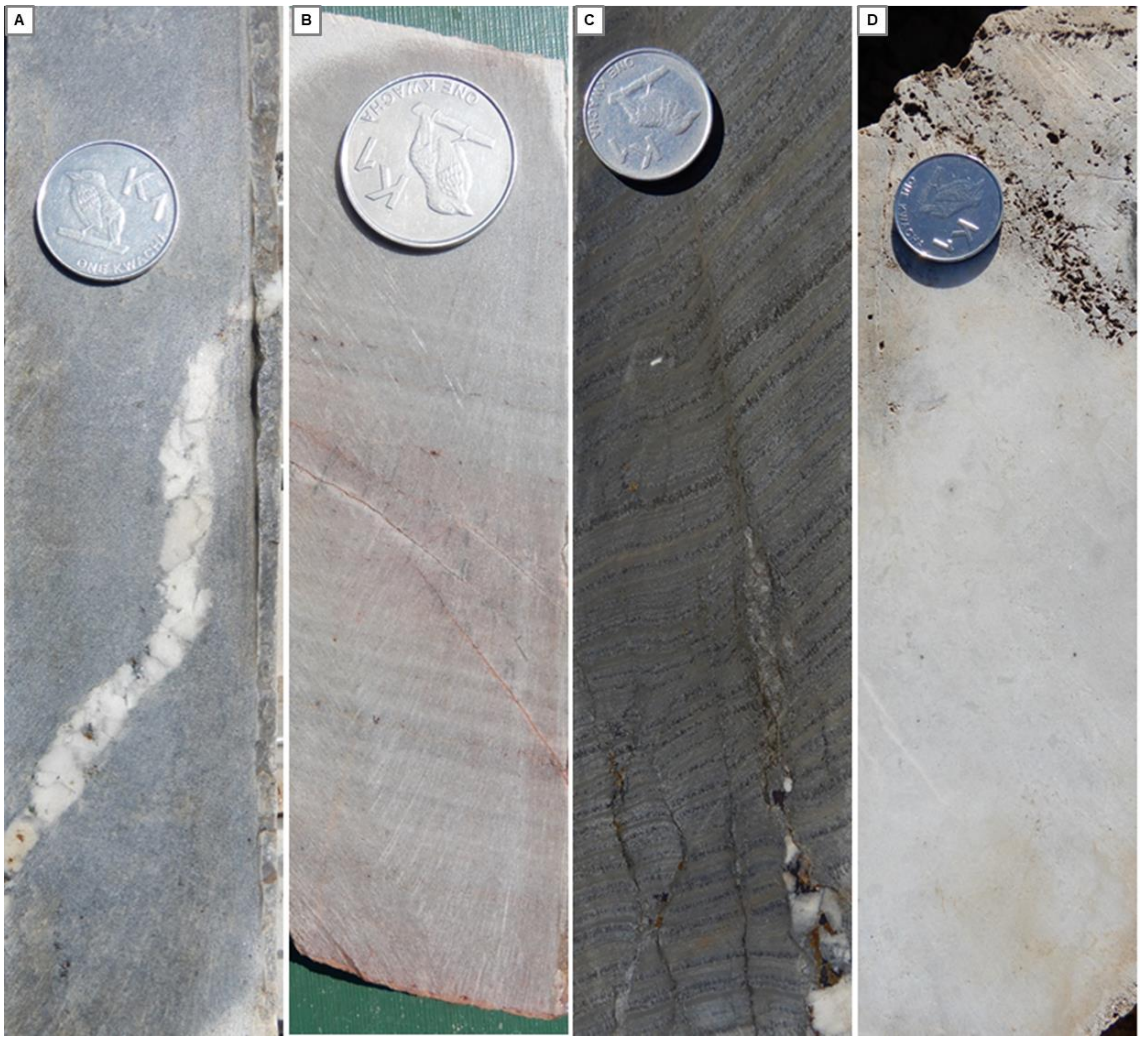

Figure 24: Rock types of the dolomite unit: (A) massive grey dolomite cut by quartz - dolomite vein, (B) pink laminated dolomite, (C) dark gray bedded dolomite cut by subvertical quart-dolomite stock work vein of disseminated sulfides, and (D) fine-grained white upper dolomite, the surface has voids due to carbonate dissolution.

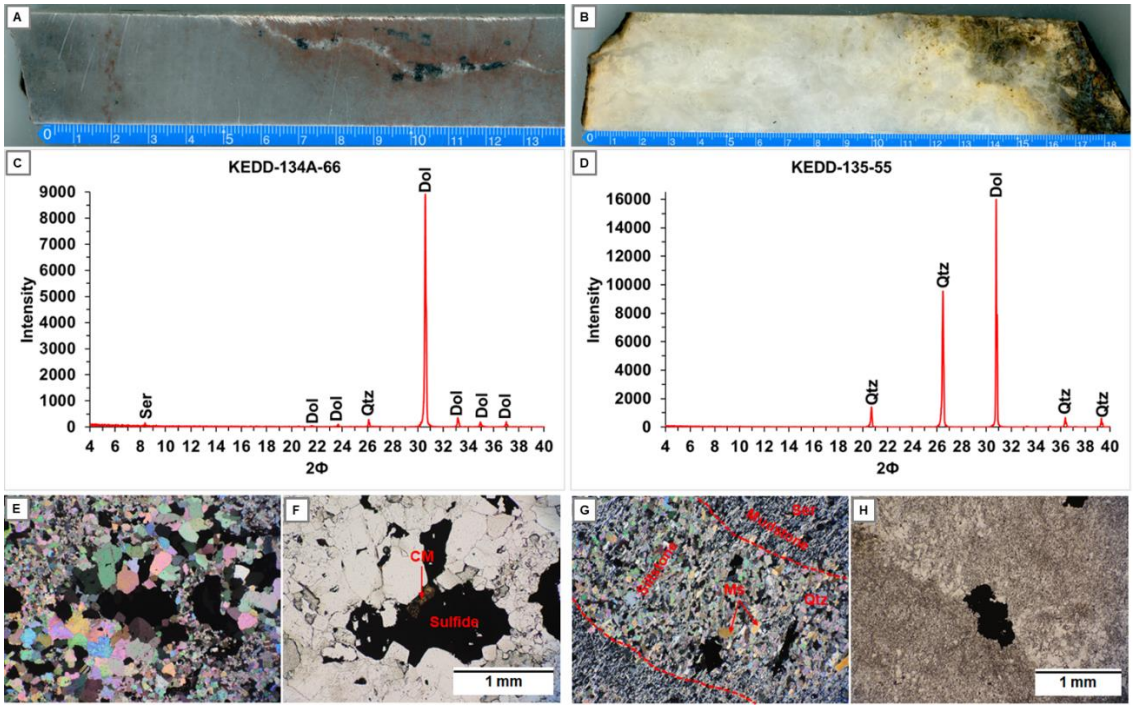

Figure 25: (A) pink massive dolomite, (B) white fine-grained upper dolomite, (C) XRD pattern of the pink massive dolomite in A, (D) XRD pattern of the fine-grained upper reprecipitated dolomite in B, (E) plane-polarized photomicrograph of the pink massive dolomite in A consisting of medium to coarse grained dolomite, (F) cross-polarized photomicrograph showing the same view as in E, (G) plane-polarized photomicrograph of bedded dolomite, (H) cross-polarized photomicrograph of bedded dolomite. Mineral abbreviation: CM- carbonaceous material, Ms- muscovite, Qtz- quartz, Ser- sericite.

4.2.3 Fine sandstone, siltstone and mudstone

These rocks comprise an approximately 50 m thick alternating beds of fine sandstone, siltstone and mudstone overlying the dolomite unit conformably. The siltstone and sandstone beds are light to dark gray in color, while mudstone displays color variations from olive green to black, probably reflecting preservation of organic matter and changes in the depositional environment to lagoonal, sabkha facies (El Desouky et al, 2009) (Fig. 26A and B). The interbedded sandstone, siltstone and mudstone beds are strongly folded and sometimes cut by stockwork veins in intervals (Fig. 26C). The folded interbeds of sandstone, siltstone and mudstone often correspond to zones of elevated Cu concentration. In the mineralized zone, the surface of these rocks is impregnated with fluid flow, gas-like structures (Fig. 26D). The gas structures have a

black, wavy outline and a white core. They are referred to as “mopane worm” textures in this dissertation because of their resemblance to the mopane worms, a food delicacy enjoyed in the southern part of Africa. The mopane worm textures are associated with black mudstone beds. The gas seems to emanate from the black mudstone and flows to the sandstone-siltstone beds. The sulfide minerals are closely associated with mopane textures, suggesting that this gas was involved in sulfide mineralization. The gas flow direction, grading and the orientation of core was used to identify overturned beds.

The mudstone beds have organic matter and are mainly composed of quartz and fine-grained white mica (sericite) and minor K-feldspar, albite, calcite, siderite and dolomite (Fig. 27B and C). The sandstone/ siltstone beds are dolomite-rich (Fig. 27D and E).

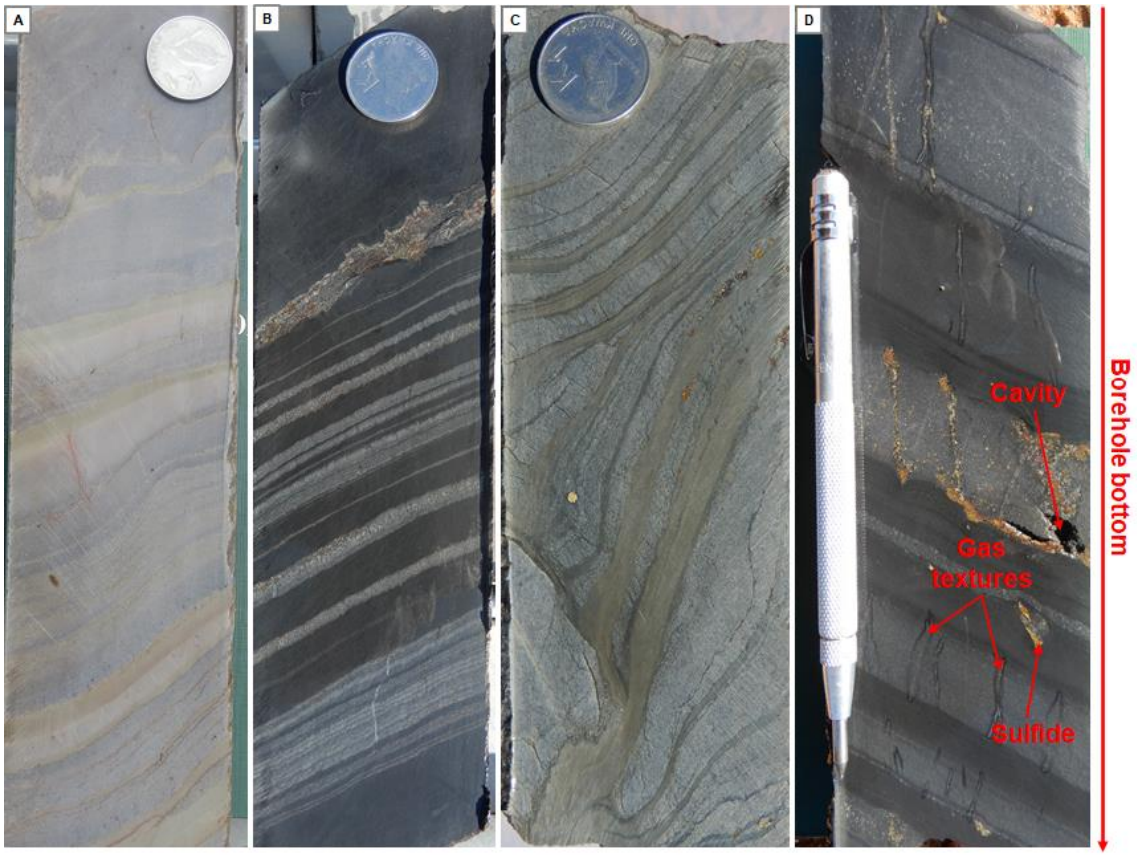

Figure 26: Rock type of the interbedded sandstone, siltstone and mudstone unit. (A) layered alternating beds of gray sandstone/ siltstone and olive-green mudstone, (B) layered alternating beds of gray sandstone/ siltstone and black mudstone, (C) folded alternating beds of gray sandstone/ siltstone and olive-green mudstone, and (D) layered

alternating beds of gray sandstone/ siltstone and black mudstone comprising of gas textures/ structures.

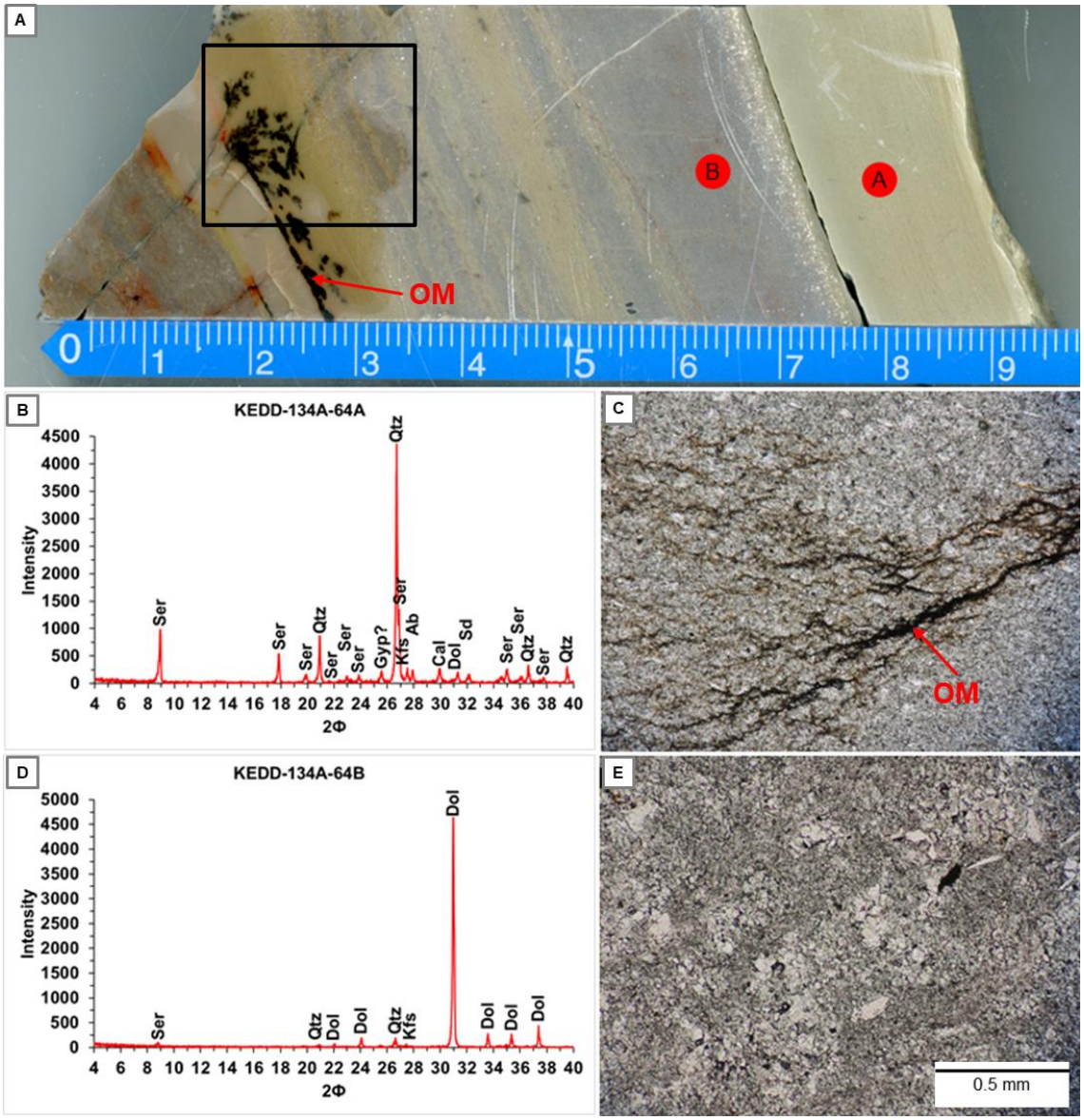

Figure 27: Petrography of interbedded fine-grained sandstone/ siltstone and mudstone, (A) Sample KEDD-134A-64, drilled at 155 m. A and B shows the point where the sample for XRD was obtained, the black square shows the point where the thin section was prepared from, (B) XRD pattern for olive-green mudstone at point A in sample KEDD-134A-64, (C) cross-polarized photomicrograph of olive-green mudstone from point A in KEDD-134A-64, (D) XRD pattern for gray fine-grained sandstone/ siltstone at point B in KEDD-134A-64, (E) cross-polarized photomicrograph of sandstone/ siltstone from point B in KEDD-134A-64.

4.3 Hydrothermal alteration

Although rocks at the Fishtie deposit experienced low-grade, green facies metamorphism, the footprints of hydrothermal alteration are still clearly discernable especially in the Conglomérat unit. Three types of alteration have been observed and logged from drill core. These are muscovite, chlorite and biotite alteration (Fig. 28).

Muscovite is a common alteration observed in the Conglomérat and interbedded siltstone and mudstone unit. In the diamictite and sandstone of the Conglomérat unit, muscovite alteration is recognized from the gray color appearance of the rocks (Fig. 28A). Muscovite alteration affects both the clasts and matrix of the diamictite and sandstone. Muscovite alteration in the interbedded siltstone and mudstone unit is more prevalent in the olive-green siliciclastic-rich mudstone beds. Muscovite alteration occurs as selective to pervasive replacement of detrital albite, chlorite, K-feldspar, dolomite and muscovite by fine-grained white mica (sericite) (Fig. 29A and B). In diamictite and sandstone, muscovite alteration involves replacement of detrital albite, chlorite, K-feldspar and muscovite by sericite in the granitoid clasts. Muscovite alteration in the siliciclastic-rich mudstone beds is commonly observed a replacement of detrital muscovite and dolomite by fine-grained white mica. Muscovite mineralized rocks generally lack calcite and dolomite but contain ankerite. Ankerite is commonly restricted to clast rims or to chlorite-rich zones where it is associated with sulfides suggesting it is related to a later phase of mineralization.

The muscovite alteration is overprinted by chlorite alteration. Chlorite alteration is present throughout the Conglomérat and the copper-sulfide mineralized beds of the interbedded siltstone and mudstone unit. Chlorite alteration is easily identified in diamictite and sandstone of the Conglomérat unit from its characteristic light green color, where it commonly occurs rimming the granitoid and dolomite clasts (Fig. 28B). XRD analysis of the rocks from the interbedded siltstone and mudstone unit shows that chlorite alteration is abundant in the copper-sulfide mineralized black mudstone beds. Chlorite replaces albite, muscovite and dolomite in the granitoid clasts and matrix of the diamictite and sandstone (Fig. 29C and D). The chlorite forms small to moderate sized (20-200 μm) anhedral grains. It does not display a preferred orientation. The chlorite-

mineralized rocks are distinguished by abundant fine-grained quartz in the diamictite matrix. This quartz lacks the obvious detrital shapes seen in samples lacking abundant chlorite. The textures suggest that this quartz precipitated during chlorite formation. Chlorite is both intergrown with and mantles apatite grains and grain aggregates. Chlorite also overgrows ankerite that occurs as small (20-50 μm) anhedral crystals throughout the matrix. Copper-sulfide minerals are most commonly intergrown with chlorite suggesting it is temporally related to the dominant period of sulfide mineralization. The chlorite-quartz assemblage present in the Fishtie samples is somewhat reminiscent of the late magnesian alteration assemblages present throughout the Central African Copperbelt (Hitzman et al., 2012) but most prominent in the deposits in the DRC.

The biotite alteration overprints both the gray muscovite and dark green chlorite alteration as a pervasive brown alteration in the matrix of the Conglomérat unit (Fig. 28C). Biotite alteration also rims granitoid clasts and is extensively developed in the matrix of the diamictite. Biotite-rich diamictite is most common at the top of the Conglomérat unit, although minor biotite occurs throughout the unit. No clearly visible biotite alteration was observed in the rocks of the interbedded siltstone and mudstone. Biotite replaces albite in both granitoid clasts and matrix of the diamictite (Fig. 29E and F). Biotite alteration is commonly associated with apatite, siderite, magnetite and pyrrhotite. This alteration mineral assemblage and textural relationships suggests that the biotite alteration was an iron-rich alteration. Apatite is common in matrix as small (10-40 μm) rounded crystals that are rimmed or partially replaced siderite. Biotite may contain small (10-50 μm) subhedral to anhedral inclusions of muscovite and commonly replaces chlorite. The biotite alteration is not closely related to copper sulfide mineralization. In the mineralized zones, biotite alteration is commonly associated with chalcopyrite that has a weathered texture, suggesting probably remobilizing of the earlier formed copper sulfide minerals during biotite alteration.

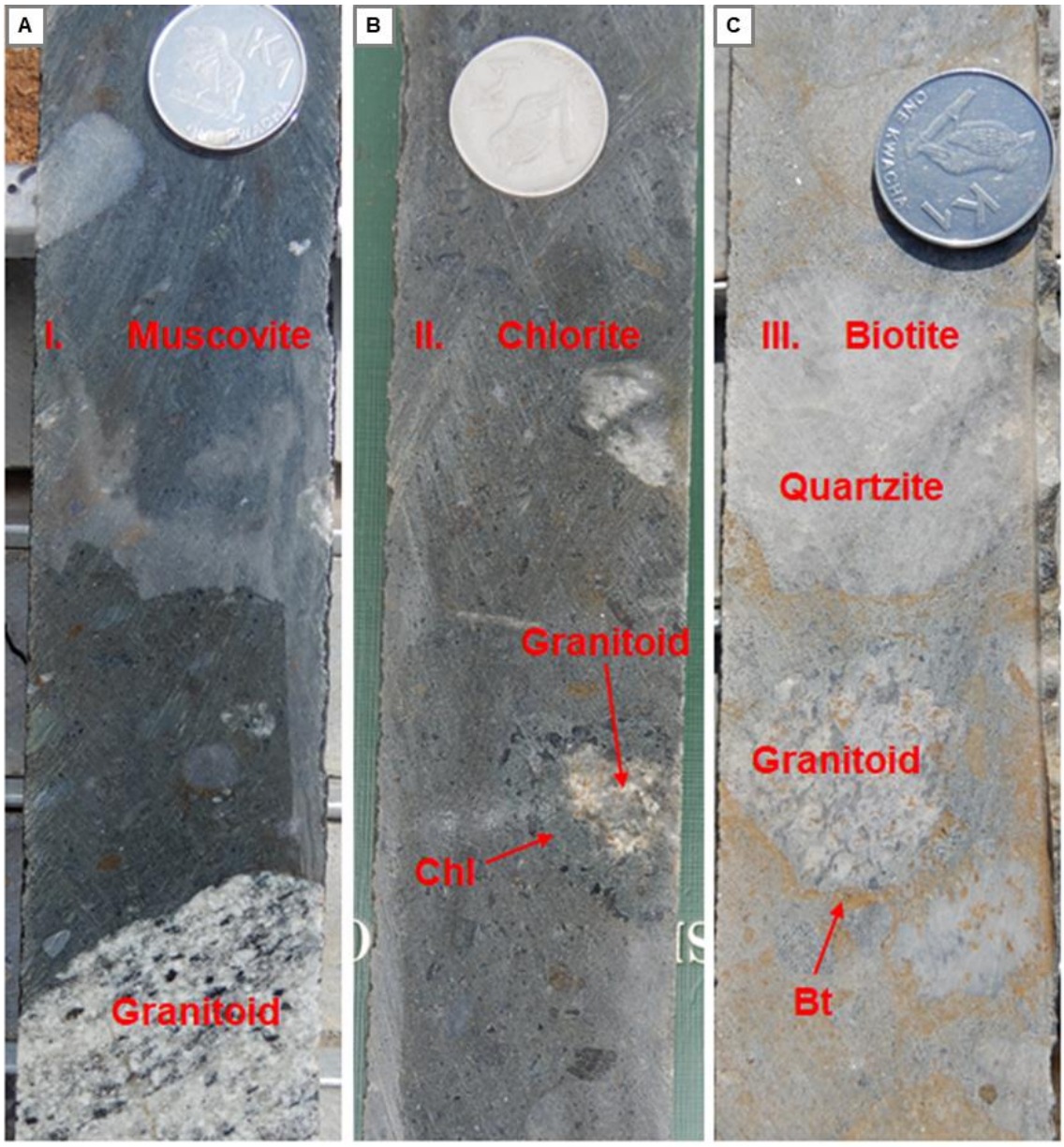

Figure 28: Hydrothermal alteration affecting the rocks at the Fishtie deposit. (A) muscovite alteration involving replacement of Conglomérat clasts and matrix, giving a gray appearance to the rocks, (B) chlorite alteration replacing the margins of the granitoid clasts, dolomite and the matrix and giving the rock a characteristic green color, and (C) biotite alteration showing pervasive replacement of the Conglomérat matrix by brown biotite. Mineral abbreviations: Bt- biotite, Chl- chlorite.

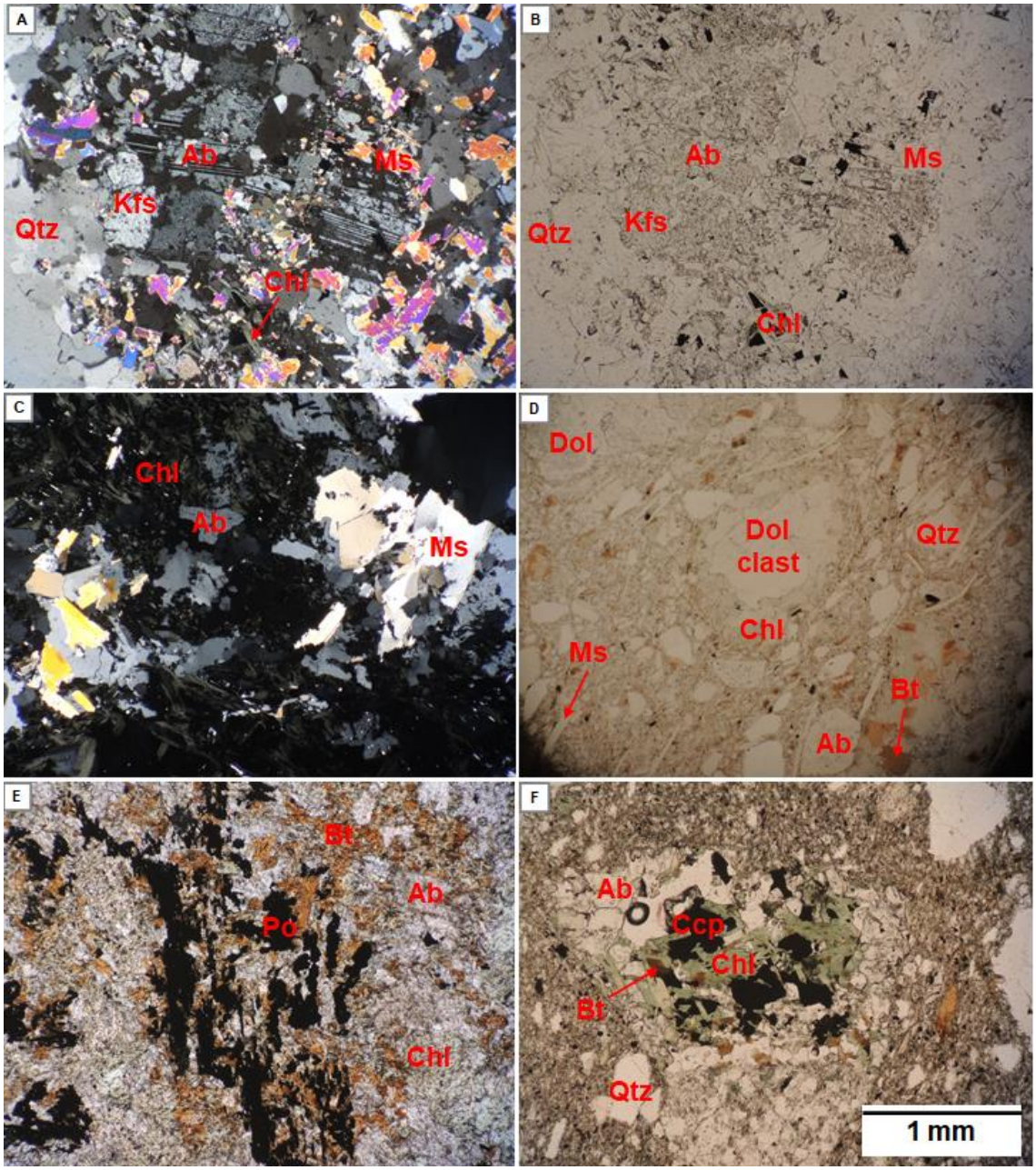

Figure 29: (A) cross-polarized transmitted light photomicrograph of diamictite showing replacement of albite and chlorite by fine-grained white mica, (B) plane-polarized transmitted light photomicrograph showing the same view as in A, (C) cross-polarized transmitted photomicrograph of diamictite showing pervasive replacement of albite and muscovite and chlorite, (D) plane-polarized transmitted light photomicrograph of diamictite showing replacement of dolomite by chlorite in the matrix, (E) plane-polarized transmitted light photomicrograph showing pervasive replacement of albite and chlorite by biotite in the matrix of diamictite, and (F) plane-polarized transmitted light photomicrograph of diamictite showing patchy replacement of chlorite and albite by biotite in the granitoid clast. Mineral abbreviations: Ab- albite, Bt- biotite, Ccp- chalcopyrite, Chl- chlorite, Dol- dolomite, Kfs- k-feldspar, Ms- muscovite, Qt- quartz, and Po- pyrrhotite.

4.4 Copper and cobalt minerals

Logging and whole-rock geochemical data from assays shows that copper and cobalt minerals at Fishtie can be divided into two zones based on the vertical distribution of sulfur (Fig. 30). The upper portion of the boreholes (approximately 50 m in borehole KEDD-140) is strongly depleted in sulfur and forms the oxidized or supergene blanket. Below this zone, copper and cobalt metals are associated with enrichment in sulfur forming the sulfide or hypogene zone.

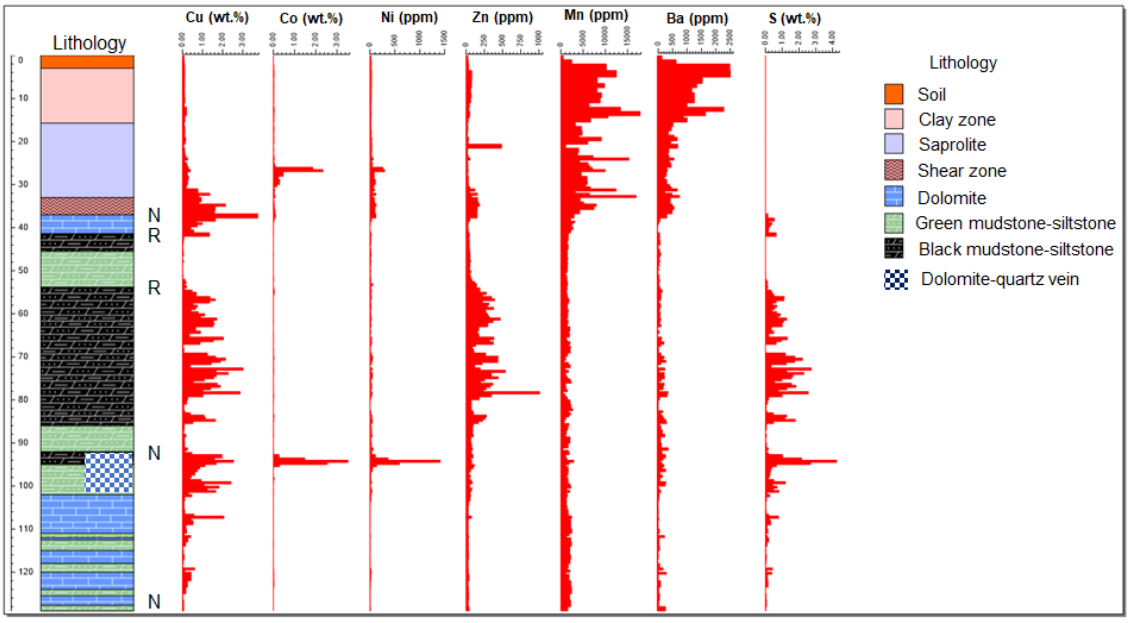

Figure 30: Strip log showing the vertical distribution of lithology, copper, cobalt, nickel, zinc, barium, manganese and sulfur metals in borehole KEDD-140.

4.4.1 Sulfide mineralization

Rocks of the Conglomérat unit at the Fishtie deposit contain both iron and copper sulfides. Iron sulfides include pyrite and pyrrhotite. Sulfide minerals are commonly observed as disseminated fine-grains of pyrite, chalcopyrite and pyrrhotite in sandstone and in the granitoid clasts and matrix of the diamictite (Fig. 31A). In overlying massive dolomite unit, sulfide mineralization is restricted to dolomite-quartz stockwork veins

where it occurs as disseminated coarse blebs of bornite and chalcopyrite (Fig. 31B). In the interbedded siltstone and mudstone beds, pyrite, chalcopyrite, bornite and chalcocite are disseminated preferentially in the siltstone beds (Fig. 31C). The Majority of these sulfide minerals occur in folded interbedded siltstone and mudstone beds, especially in the zones of black mudstone (Fig. 31D). The highest grades of copper contained in the hypogene sulfide zone occur in the central and satellite structural domain within the Conglomérat unit diamictites immediately adjacent to normal faults, along the contact between the Conglomérat and interbedded siltstone and mudstone unit, and within the dolomite-quartz stockwork veins embedded in the massive dolomite (Hendrickson et al, 2015).

Fine-grained (< 50 microns) pyrite with subrounded shapes suggestive of a framboidal habit occurs throughout the rocks at the Fishtie area but disseminated pyrrhotite is restricted to the Conglomérat unit (Fig. 32A). While disseminated pyrrhotite and pyrite may be present in the same sample, generally they occur separately. Pyrrhotite is usually intergrown with chalcopyrite and sphalerite and is associated with biotite, apatite, siderite, ilmenite, magnetite and rutile. The sulfide minerals display some weathering and possibly remobilization textural features. In the dolomite-stockwork veins of the massive dolomite, the sulfide mineralization is dominated by intergrown chalcopyrite, bornite and chalcocite (Fig. 32B). Bornite and chalcopyrite are intergrown, chalcocite appears to be replacing chalcopyrite. Cobaltite and emplectite were identified as the main cobalt sulfide minerals using SEM-EDS. Cobaltite is disseminated in the main dolomite-quartz stockwork veins and in the folded beds of layered dolomite close to the veins. Cobaltite has a massive texture and is intergrown with bornite (Fig. 32C, D and E). Emplectite on the other hand is often seen replacing bornite and chalcocite.

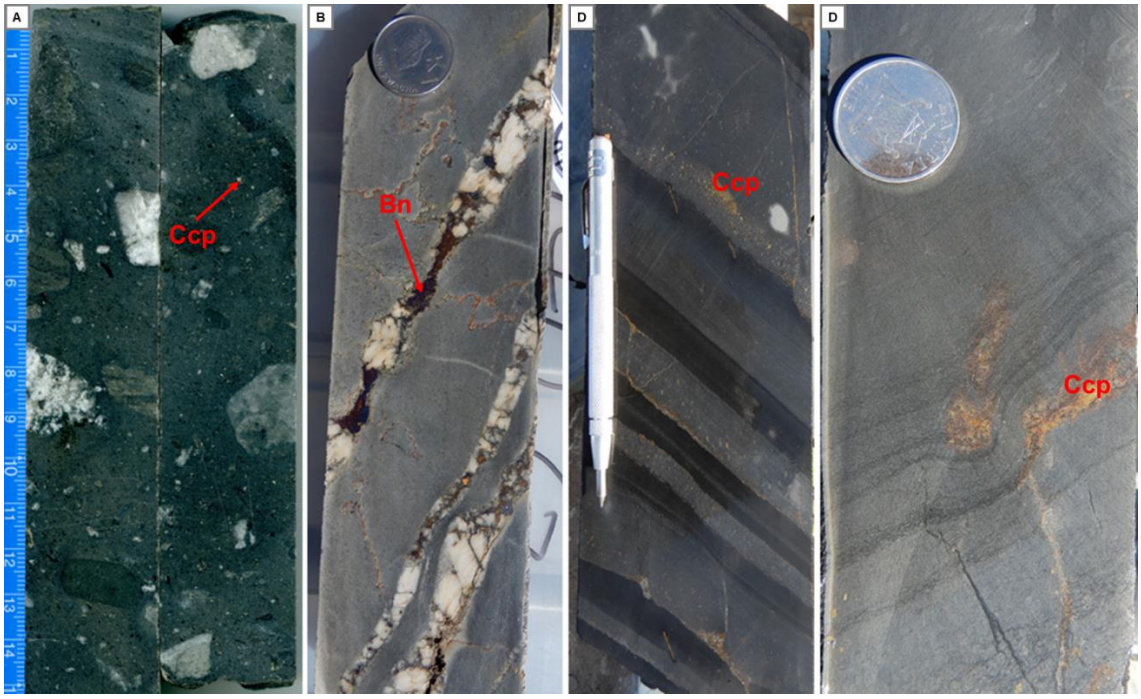

Figure 31: Occurrence of copper and cobalt sulfide minerals in the rocks at the Fishtie deposit. (A) disseminated chalcopyrite and pyrrhotite in the matrix of the diamictite, (B) disseminated coarse-grained bornite and chalcopyrite in dolomite-quartz stockwork veins in the massive dolomite, (C) chalcopyrite disseminated in siltstone beds of the interbedded siltstone and black mudstone unit, and (D) folded beds of thinly laminated siltstone and mudstone unit. Mineral abbreviations: Bn- bornite, Ccp- chalcopyrite.

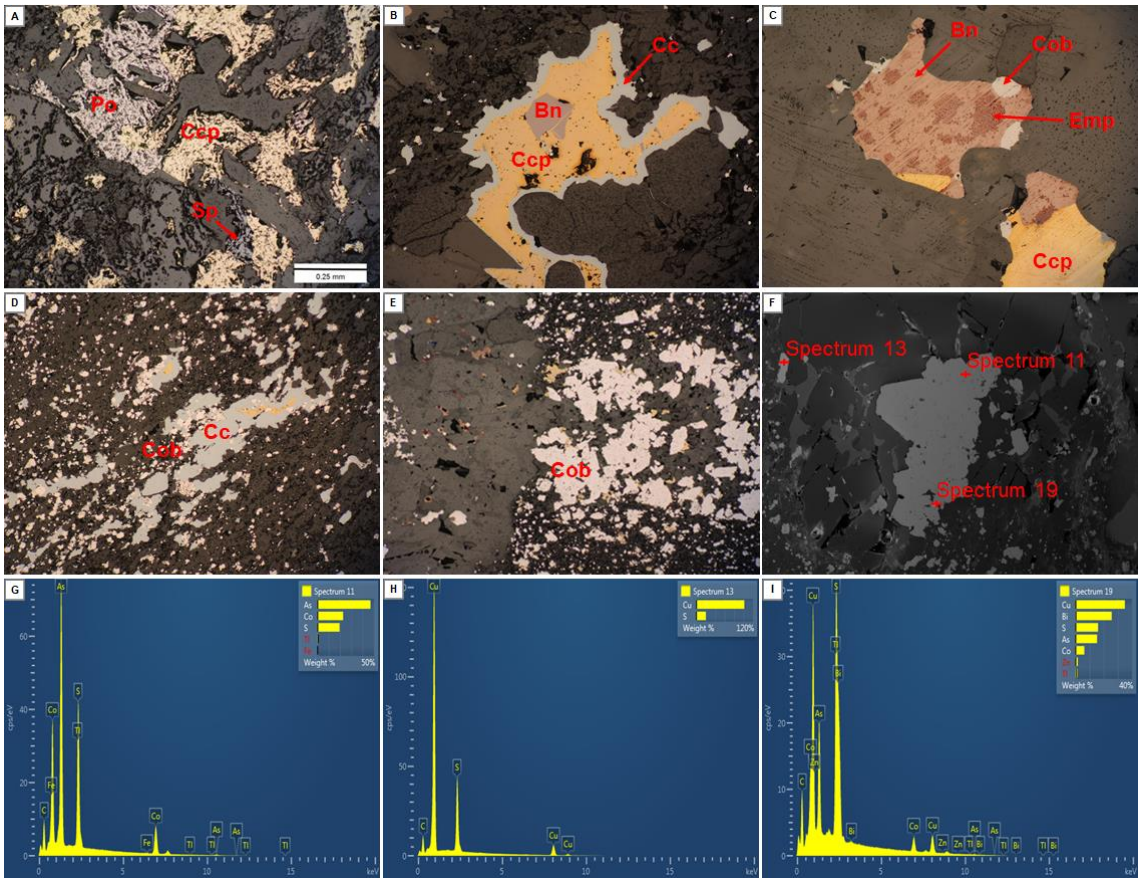

Figure 32: Petrographic observation of copper and cobalt sulfide minerals at the Fishtie deposit. (A) disseminated pyrrhotite, chalcopyrite and zinc in the matrix of the diamictite, (B) Intergrown and replacement texture of bornite, chalcopyrite and chalcocite in the dolomite-quartz stockwork vein, (C) occurrence of cobaltite, emplectite, and chalcopyrite in the dolomite-quartz stockwork vein of the massive dolomite, (D) disseminated cobaltite and chalcocite in the layered dolomite close to the stockwork vein. Chalcocite occurs replacing chalcopyrite, (E) occurrence of coarse-grained cobaltite at the margin of the dolomite-quartz vein in the folded beds of layered dolomite, (F) backscattered electron image from SEM-EDS showing points where spectrums 11, 13 and 19 were analyzed, (G) SEM-EDS analysis result for cobalt at spectrum 11, (H) SEM-EDS analysis result for chalcocite at spectrum 19, and (I) SEM-EDS analysis result for emplectite at spectrum 19. Mineral abbreviations: Bn- bornite, Cc- chalcocite, Ccp- chalcopyrite, Cob- cobaltite, Emp- emplectite, Sp- sphalerite, and Po- pyrrhotite.

4.4.2 Supergene mineralization

The Fishtie deposit contains a significant amount of oxide and mixed oxide-sulfide copper and cobalt minerals. The supergene-mineralized zone occurs within saprolites developed at the base of the clay zone. The highest-grade portions of this supergene

body occur within the central structural domain and form 1 m to 30 m thick zone approximately 450m long (east-west) and 125m wide (north-south) (Hendrickso et al., 2015).

The supergene mineralized zones consist of dark gray to black unconsolidated saprolite composed of chlorite, kaolinite, sericite and the copper oxide and carbonate minerals (malachite>> azurite), and chalcocite with remnant wall rock carbonate minerals and minor quartz. Grades over one meter in this material may exceed 4.5% Cu.

Petrographic observation of secondary copper minerals in fractured rocks close to the saprolite shows that chalcopyrite is overprinted by chalcocite (Fig. 33A). The chalcocite is later replaced by malachite and azurite in dolomite-rich zones (Fig. 32B). In quartz-rich reprecipitated dolomite, chrysocolla is often observed. Native copper is sometimes observed in malachite-rich zones (Fig. 33C). Cobalt oxide minerals are observed as heterogenite and cobaltoan dolomite in dolomite veins (Fig. 33D, E, and F). Hetereogenite is sometimes intergrown with a yellowish green copper arsenic mineral (conichalcite) in the dolomite vein (Fig. 33D). Heterogenite is often black in hand spacemen and displays a conchoidal texture. Cobaltoan dolomite has a distinctively pinkish color in drill core.

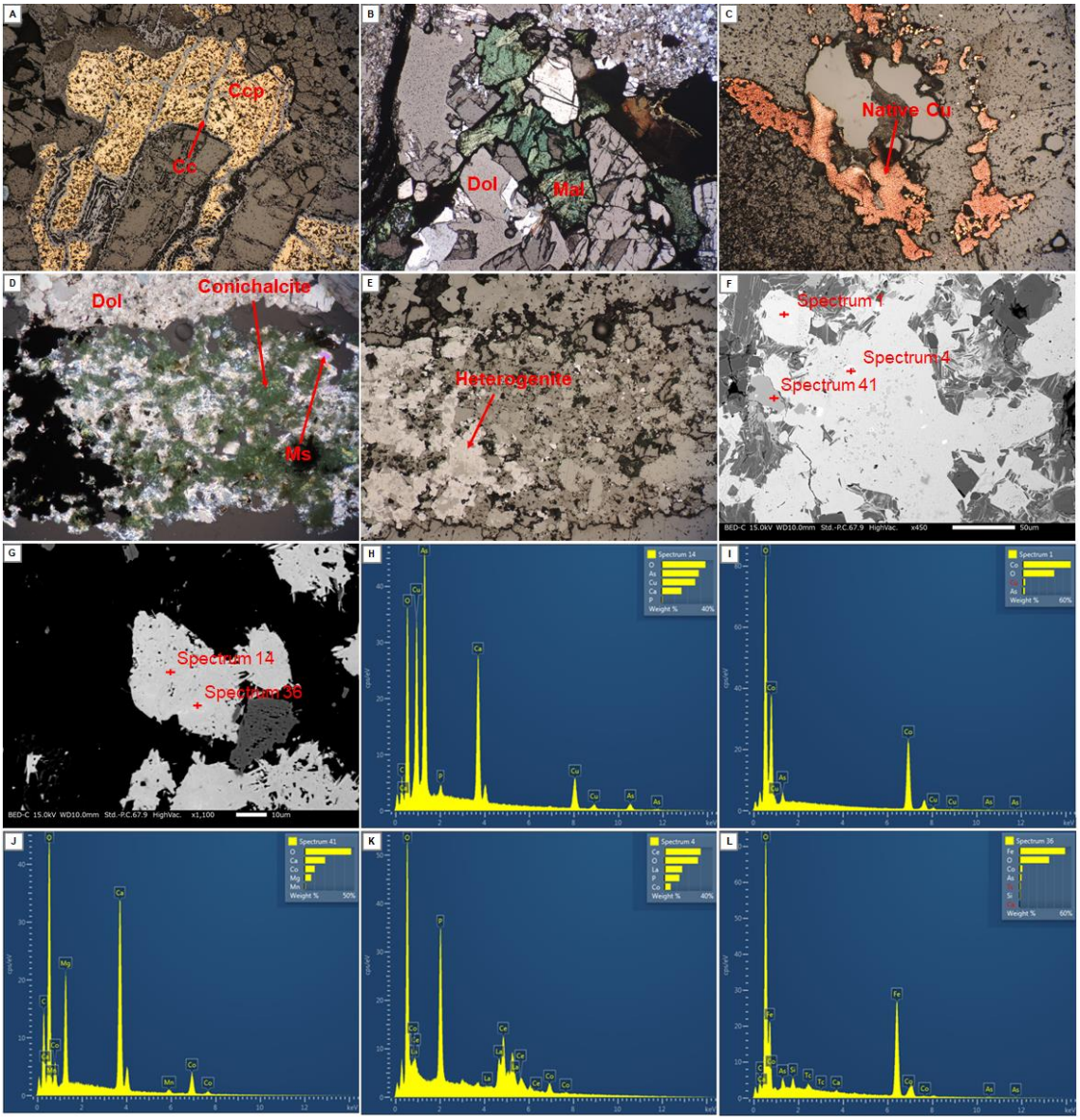

Figure 33: Petrographic observations and EDS spectra of secondary copper and cobalt minerals. All images were taken by optical microscopy, except where otherwise specified. (A) replacement of chalcopyrite by chalcocite, (B) malachite and azurite in dolomite-rich stockwork vein, (C) native copper observed in a calcite vein, (D) conichalcite and cobaltoan dolomite in a dolomite vein, (E) heterogenite in dolomite vein, (F) SEM-EDS backscattered electron image showing the spectrum analysis point for heterogenite, monanzite, and cobaltoan dolomite, (G) SEM-EDS backscattered electron image showing the spectrum analysis point for conichalcite and goethite, (H) EDS spectrum indicating the composition of conichalcite, (I) composition of heterogenite, (J) composition of cobaltoan dolomite, (K) composition of cobalt bearing mononzite, and (L) composition of cobalt bearing goethite. Mineral abbreviations: Cc- chalcocite, Ccp- chalcocite, Dol- dolomite, Mal- malachite, Ms- muscovite.

4.5 Mineral chemistry

Although the footprints of hydrothermal alteration are clearly visible at the Fishtie, it is still difficult to understand alteration paragenesis and relationship to ore mineralization because of the overprinted style of alteration. For this reason, mineral chemistry of the alteration minerals of chlorite, muscovite and biotite was conducted using electron micro probe analyzer to study the nature of the fluids responsible for the observed alteration minerals.

4.5.1 Chlorite geochemistry

Besides biotite and muscovite, chlorite is the main alteration mineral in the diamictite and sandstone of the Conglomérat unit. Chlorite geochemistry records changes in transition metal availability through substitution of divalent and trivalent cations into the mineral structure (Uvarova et al., 2018). Chlorites in this study were analyzed by WDS electron microprobe and the compositions were quantified, as shown in tables 2 and 3 below. Based on the calculated atomic abundances of Fe, Mg, and Al, the chlorite analyzed at the Fishtie deposit is exclusively of the type 1 trioctahedral endmembers and is classified as either Mg-chlorite (clinochlore) and Fe-chlorite (chamosite) (Fig. 34; Zane and Weiss, 1998). Although there are cases where both clinochore and chamosite have been observed in the same sample, a spatial distribution pattern is observed between these two chlorite types. Clinochlore has a much wider distribution pattern but chamosite seems to occur only in zones affected by biotite alteration, probably suggesting that the two chlorites formed during two separate hydrothermal events. Clinochlore is closely associated with albite, dolomite and chalcopyrite (Fig. 35A and B). Chamosite on the other hand, occurs in rocks composed of biotite, siderite, pyrrhotite, chalcopyrite, sphalerite, and magnetite (Fig. 35C and D). This difference in the mineral assemblages related to the two chlorites points to a variation in the composition of the hydrothermal fluids that caused the alteration. Chalcopyrite associated with clinochlore and chamosite shows textural differences; chalcopyrite in

clinochlore assemblage has a smooth surface, whereas in the chamosite assemblage the chalcopyrite displays a weathered texture (Fig. 35B and D).

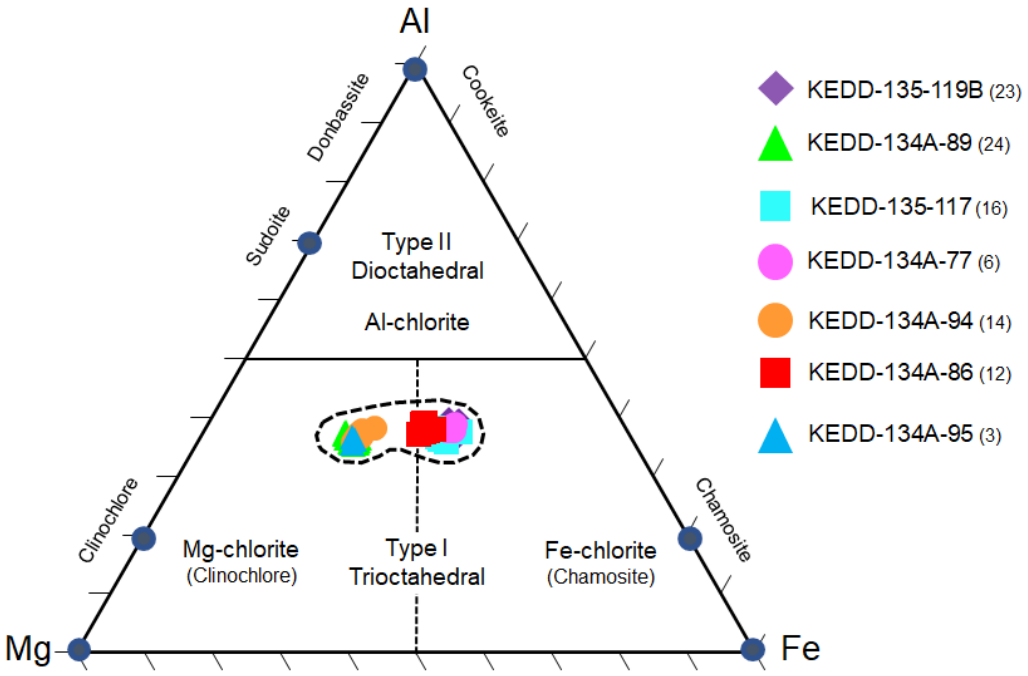

Figure 34: Compositional diagram for rock-forming chlorites from rocks of the Conglomérat unit at the Fishtie deposit in the Al-Mg-Fe tenary diagram (from Zane and Weiss, 1998).

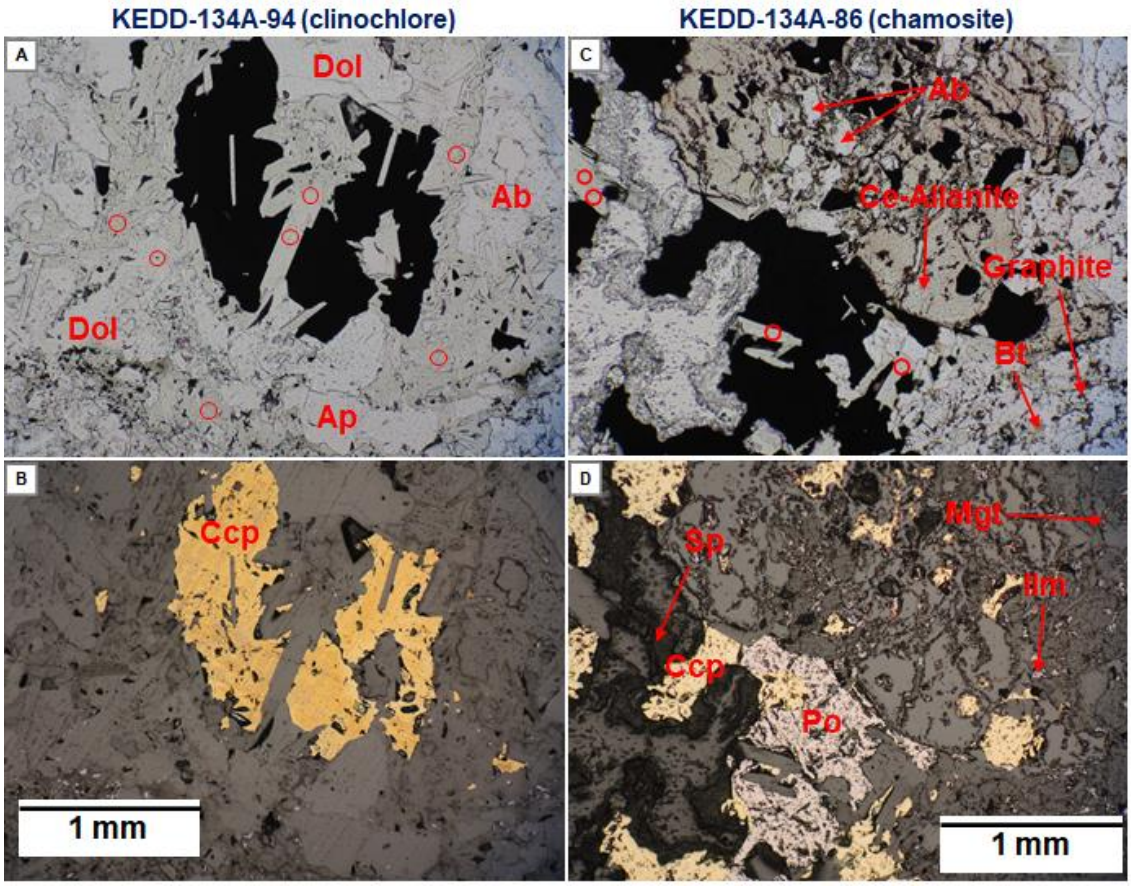

Figure 35: (A) plane-polarized transmitted light photomicrograph of Mg-chlorite (clinochlore) associated with albite, dolomite, chalcopyrite, (B) plane-polarized reflected light photomicrograph showing the same view as in A, (C) plane-polarized transmitted light photomicrograph of Fe-chlorite (chamosite) associated with albite, biotite, allanite, graphite and sulfides; chalcopyrite, pyrrhotite and spalerite, and ilmenite and magnetite dusting. Red circles show EMPA analysis point. Mineral abbreviations: Ab- albite, Ap- apatite, Bt- biotite, Ccp- chalcopyrite, Dol- dolomite, Ilm- ilmenite, Mgt- magnetite, Sp- sphalerite and Po- pyrrhotite.

4.5.2 Major element geochemistry of chlorite

The major element geochemistry of chlorite at the Fishtie is a function of the substitution of elements for each other in the tetrahedral and octahedral site. The chlorite general formula is given as $A_{5\text{-}6}T_4Z_{18}$ where; A = Al, Fe^{2+}, Fe^{3+}, Li, Mg, Mn, Ni, T = Al, Fe^{3+}, Si, and Z = O and/or OH. All the samples analyzed demonstrate an excellent negative correlation between Si and Al (Fig. 36A), attributed to the variable substitution of these cations for one another. Though not very clear, a negative

correlation also exists between Fe + Mg and Mn, indicating the presence of other cations in the M^{2+} octahedral site (Fig. 36B). It is further evident that an increase in the Mn content of chlorite is broadly associated with an increase in the Fe/Mg ratio, and this relationship may be linear within particular samples (Fig. 36C). This perhaps suggests Mn preferentially substitutes for Mg, or an increased Fe content favors incorporation of Mn over Mg, or vice versa. The relationship of the Fe/Mg ratio and Mn also demonstrates a clear distinction between the two types of chlorites at Fishtie where clinochlore plots with Fe/Mg ratio below 0.7 while chamosite plots above 1. The total Fe + Mg + Mn is negatively correlated with Si + Al (Fig. 36D), reflecting the overall limit of cations that can be accommodated per formula unit. Individually, increasing total Al (and thereby decreasing Si) is associated with a general reduction in Mg (Fig. 36E) but simultaneous increase in Fe (Fig. 36F) that can be incorporated into the structure, demonstrating the complex interplay between all the major cations.

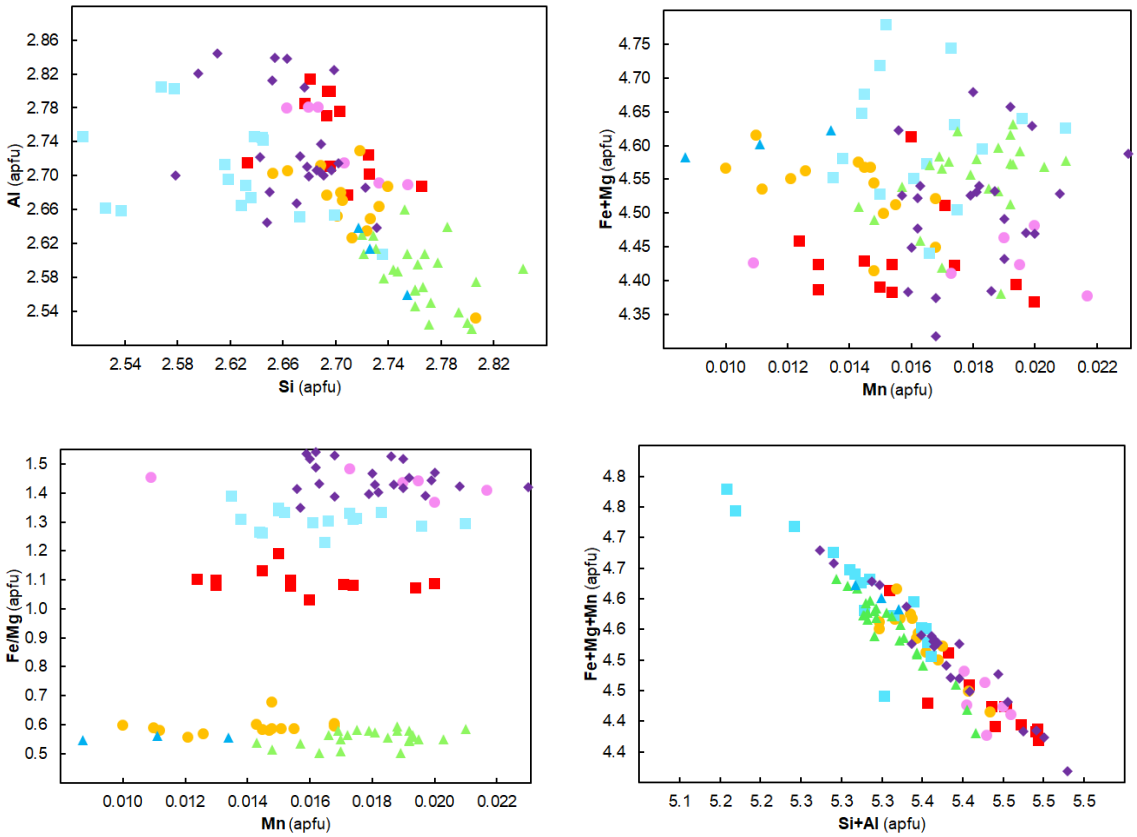

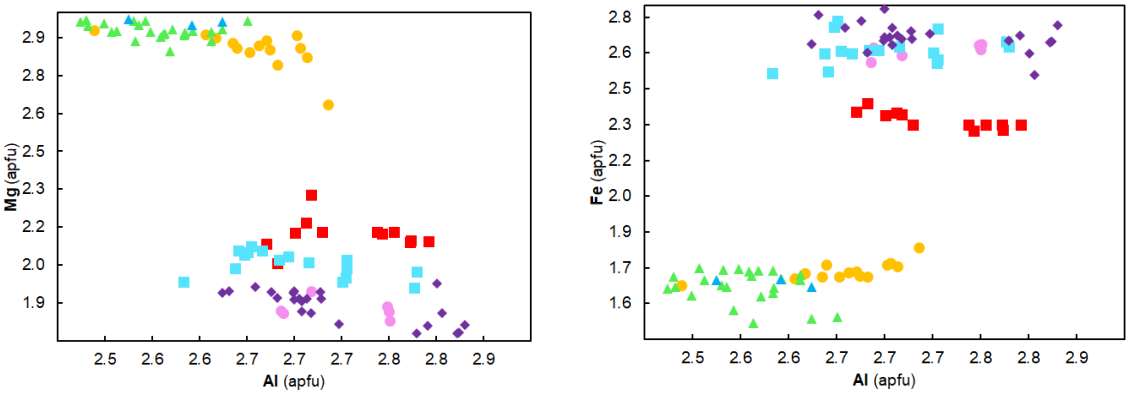

Figure 36: Major element chlorite mineral chemistry data from EMPA showing the relationship between major cations within the chlorite structure. Note all data are shown in atoms per formula unit (a.p.f.u) calculated based on 28 oxygens equivalents.

4.5.3 Minor element geochemistry of chlorite

Minor element geochemistry of chlorite was conducted to investigate the relationship of copper, cobalt, zinc and manganese and some major elements. Copper and cobalt show different correlation trends with Mg and Fe (Fig. 37). Although not very clear, the relationship of Cu and Fe shows a negative correlation, while the correlation with Mg is positive (Fig. 37A, and B). On the contrary, Co has a positive correlation with Fe and is negatively correlated with Mg (Fig. 37C and D). This relationship suggests Cu preferentially substitutes for Fe, or an increased Mg content promotes incorporation of Cu over Fe, or vice versa. Incorporation of Co in chlorite on the other hand is favoured by increased Fe content or substitution for Mg. A negative relationship is observed between Cu and Mn, while Co displays a linear correlation (Fig. 37E and F). This may imply that Cu and Mn substitute each other in the octahedral site. The correlation of Cu and Co does not show a clear trend but a linear relationship can be assumed (Fig. 37G). Zinc shows opposing correlation trends with Cu and Co (Fig. 37H and I). A negative relationship is observed between Zn and Cu but the relationship is linear to positive with Co.

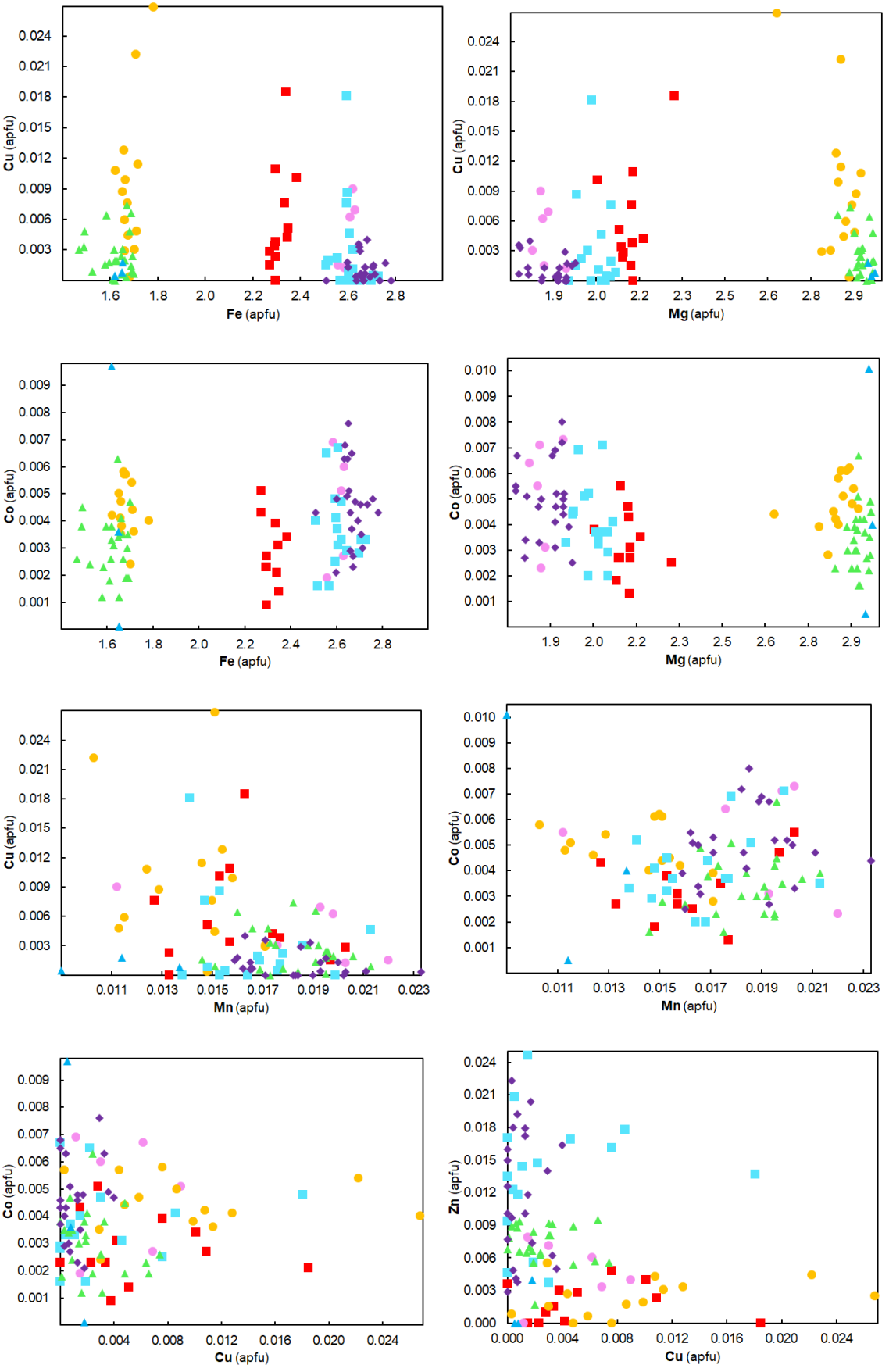
Cu (apfu)
Fe (apfu)
Cu (apfu)
Mg (apfu)
Co (apfu)
Fe (apfu)
Co (apfu)
Mg (apfu)
Cu (apfu)
Mn (apfu)
Co (apfu)
Mn (apfu)
Co (apfu)
Cu (apfu)
Zn (apfu)
Cu (apfu)

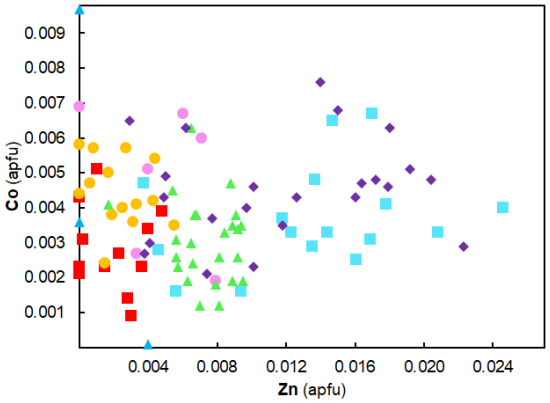

Figure 37: Minor element chlorite mineral chemistry data from EMPA showing the relationship between minor cations within the chlorite structure. Note all data are shown in atoms per formula unit (a.p.f.u) calculated based on 28 oxygens equivalents.

Table 2: Chemical composition (wt.%) of chlorites from rocks of the Conglomérat unit at the Fishtie deposit.

Oxide (wt%)	Diamictite KEDD-134A-89 (24)	Diamictite KEDD-134A-94 (14)	Diamictite KEDD-134A-95 (3)	Siltstone KEDD-134A-86 (12)	Diamictite KEDD-134A-77 (6)	Diamictite KEDD-135-119B (23)	Diamictite KEDD-135-117 (16)
SiO_2	25,51	26,06	24,75	25,31	25,18	22,05	23,58
TiO_2	0,04	0,04	0,02	0,05	0,05	0,05	0,08
Al_2O_3	20,22	21,73	20,01	21,84	21,65	19,18	20,65
FeO	17,90	19,34	17,77	25,93	29,03	26,34	28,12
MnO	0,20	0,16	0,12	0,17	0,20	0,18	0,17
CoO	0,04	0,06	0,06	0,04	0,06	0,05	0,05
ZnO	0,09	0,03	0,02	0,02	0,06	0,13	0,17
CuO	0,03	0,12	0,01	0,07	0,06	0,01	0,04
MgO	18,11	18,38	17,99	13,32	11,39	10,19	12,07
CaO	0,03	0,03	0,01	0,09	0,05	0,01	0,07
Na_2O	0,01	0,01	0,03	0,01	0,01	0,01	0,05
K_2O	0,04	0,02	0,02	0,02	0,07	0,02	0,12
F	0,07	0,09	0,20	0,02	0,01	0,02	0,03
Cl	0,02	0,02	0,01	0,04	0,04	0,04	0,05
H2O	11,03	11,48	10,76	11,22	11,16	9,89	10,77
O=F	0,03	0,04	0,09	0,01	0,00	0,01	0,01
O=Cl	0,00	0,00	0,00	0,01	0,01	0,01	0,01
Total	93,36	97,59	91,85	98,17	99,02	88,17	96,02

Table 3: Atom per formula unit (a.p.f.u.) of chlorite from the rocks of the Conglomérat unit at the Fishtie deposit.

	Diamictite KEDD-134A-89 (24)	Diamictite KEDD-134A-94 (14)	Diamictite KEDD-134A-95 (3)	Siltstone KEDD-134A-86 (12)	Diamictite KEDD-134A-77 (6)	Conglomerate KEDD-135-119B (23)	Conglomerate KEDD-135-117 (16)
OH	7.97	7.97	7.93	7.99	7.99	7.99	7.98
Si	2.77	2.71	2.73	2.70	2.70	2.67	2.62
Al(IV)	1.23	1.29	1.27	1.30	1.30	1.33	1.38
Total Tetrahedral	4.00	4.00	4.00	4.00	4.00	4.00	4.00
Al(VI)	1.35	1.38	1.34	1.45	1.44	1.40	1.32
Ti	0.00	0.00	0.00	0.00	0.00	0.00	0.01
Fe3+	0.00	0.00	0.00	0.00	0.00	0.01	0.05
Fe2+	1.62	1.68	1.64	2.31	2.61	2.66	2.56
Mn	0.02	0.01	0.01	0.02	0.02	0.02	0.02
Co	0.00	0.00	0.00	0.00	0.01	0.00	0.00
Zn	0.01	0.00	0.00	0.00	0.00	0.01	0.01
Cu	0.00	0.01	0.00	0.01	0.00	0.00	0.00
Mg	2.93	2.85	2.96	2.12	1.82	1.84	2.00
Total Octahedral	5.93	5.95	5.96	5.91	5.91	5.95	5.98
OH	7.97	7.97	7.93	7.99	7.99	7.99	7.98
F	0.02	0.03	0.07	0.01	0.00	0.01	0.01
Cl	0.00	0.00	0.00	0.01	0.01	0.01	0.01
Total	8.00	8.00	8.00	8.00	8.00	8.00	8.00

4.6 Sulfur isotope analysis

Sulfur isotopic values of diagenetic and hydrothermal sulfide minerals at Fishtie deposit were measured in order to constrain the source of sulfur for the Cu sulfide minerals. The $\delta^{34}S$ have been compared with the hosting lithology to investigate the role of lithology in the modification of sulfur isotopic signatures (Fig. 38). The wide range of isotopic values present in the sulfide assemblages at Fishtie suggests that there was no significant homogenization of isotopic values during the Lufilian metamorphic event (Hendrickson et al, 2015).

The sulfide minerals that were analyzed were selected from diamictite of the Conglomérat unit, massive dolomite in the dolomite unit and the interbedded siltstone and mudstone unit. Fine grained, disseminated chalcopyrite and pyrrhotite (n=3) from the diamictites of the Conglomérat unit display a restricted range of $\delta^{34}S$ values between +9‰ and +13‰ (Fig. 38A). These values are similar to the ones obtained from pyrite replaced by Cu sulfides in the upper orebody at Nchanga deposit (McGowen et al.,

2003). The $\delta^{34}S$ values of bornite and chalcopyrite disseminated in stockwork veins of the massive dolomite display the lowest values, ranging between +1‰ and +8‰. These values overlap with the lower orebody Cu sulfides at the Nchanga deposit.

The sulfide minerals in the folded beds of the interbedded siltstone and mudstone display relatively higher values and have a very wide range from +5‰ to +27‰. The two pyrite samples from the interbedded siltstone and mudstone show generally high $\delta^{34}S$ values of +18‰ and +27‰. These values are comparable to the $\delta^{34}S$ values measured from pyrite disseminated in the late generation crosscutting veins at the Nchanga deposit. However, diagenetic pyrite from the Zambian Copperbelt commonly has $\delta^{34}S$ values lighter than 0‰ (McGowen et al., 2003). Hence the relatively heavy sulfur isotopic signature of the pyrite at Fishtie deposit may suggest replacement of early framboidal pyrite by ore stage pyrite.

Similar trends to heavier sulfur isotopic values with increasing stratigraphic height in the stratigraphic sequence have been noted in several deposits in the Zambian Copperbelt (Selley et al., 2005). A trend to increasing sulfur isotopic values with stratigraphic height has also been observed at Nchanga deposit (McGowan et al., 2003). The reasons for heavier sulfur isotopic values with increasing stratigraphic height at Nchanga deposit has been attributed to a sequential sulfate reduction in an increasingly open system.

The isotopic values of copper sulfides and ore stage pyrite at Fishtie suggests that much of the reduced sulfur was generated from thermochemical sulfate reduction of remobilized evaporites since no sulfate mineral was observed in the rocks. Thermochemical sulfate reduction of an ore-fluid requires oxidation of organic matter as part of the redox process, which liberates H_2S via the reaction:

$$CaSO_4 + CH_4 \rightarrow CaCO_3 + H_2S + H_2O \qquad \text{(Equation 4.1)}$$

Common reaction products of this reaction include carbonate, oxidized hydrocarbons, and base-metal sulfides, although no solid bitumen is found where methane is the main or only reactive hydrocarbon (Machel et al., 1995). This reaction

agrees with drill core observation where the gas structure or “mopane worm textures” had a black hallow and white core of calcite.

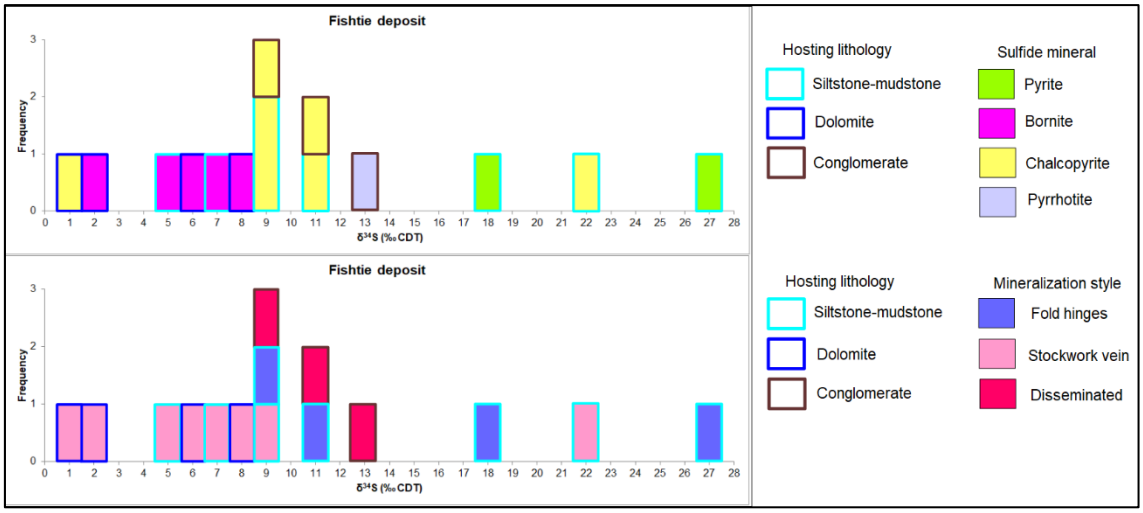

Figure 38: Histogram of sulfur isotopic values. (A) Sulfur isotopic values of sulfide species (solid color) as a function of host lithology (outline color). (B) Sulfur isotopic values as a function of the style of mineralization (solid color) and host lithology (outline color).

Table 4: Sulfur isotopic analysis results for sulfide minerals at the Fishtie deposit

No.	BID	SID	Depth	Mineral	Lithology	Description	Corrected $\delta^{34}S$
1	KEDD-140	KEDD-140-44	56	Chalcopyrite	Interbedded siltstone	Chalcopyrite intergrown with bornite is disseminated in quartz-dolomite vein in siltstone	22,8
2		KEDD-140-56	84	Chalcopyrite	Shale	Chalcopyrite disseminated in black shale	11
3		KEDD-140-60A	94	Bornite	Interbedded siltstone	Bornite intergrown with chalcopyrite, cobaltite, bismuthinite and chalcopyrite is disseminated in quartz-dolomite vein in siltstone	7,1
4		KEDD-140-60B	94	Chalcopyrite	Interbedded siltstone	Chalcopyrite intergrown with bornite, cobaltite, bismuthinite and chalcopyrite is disseminated in quartz-dolomite vein in siltstone	9,15
5		KEDD-140-65	101	Bornite	Interbedded siltstone	Bornite is disseminated in quartz-dolomite vein in siltstone	4,9
6	KEDD-135	KEDD-135-65	83	Pyrite	Interbedded siltstone	Pyrite disseminated in folded dolomite beds of interbedded siltstone	27,2
7		KEDD-135-71	97	Pyrite	Interbedded siltstone	Pyrite disseminated in layered dolomite beds of interbedded siltstone	18,8
8		KEDD-135-86	124	Bornite	Dolomite	Bornite is disseminated in quartz-calcite vein in dolomite	6,7
9		KEDD-135-105	165	Bornite	Dolomite	Bornite with chalcocite replacement is disseminated in quartz-calcite vein in dolomite	8,75
10		KEDD-135-107A	168	Bornite	Dolomite	Bornite intergrown with chalcopyrite is disseminated in quartz-calcite vein in dolomite	1,95
11		KEDD-135-107B	168	Chalcopyrite	Dolomite	Chalcopyrite intergrown with bornite is disseminated in quartz-calcite vein in dolomite	1,3
12		KEDD-135-110	174	Chalcopyrite	Interbedded siltstone	Chalcopyrite intergrown with bornite is disseminated in dolomite beds of interbedded siltstone	9,4
13		KEDD-135-117	187	Chalcopyrite	Conglomerate	Chalcopyrite intergrown with pyrrhotite is disseminated in chlorite-rich matrix of conglomerate	9,2
14		KEDD-135-119A	188	Chalcopyrite	Conglomerate	Chalcopyrite intergrown with pyrrhotite is disseminated in chlorite-rich matrix of conglomerate	11,2
15		KEDD-135-120	193	Pyrrhotite	Conglomerate	Pyrrhotite intergrown with chalcopyrite is disseminated in chlorite-rich matrix of conglomerate	13

BID- Borehole number, SID- Sample number

Chapter 5 Discussion

5.1 Mineralization model of the Fishtie deposit

5.1.1 Stage 1: sediment deposition to early diagenesis

The sedimentation style at Fishtie commenced with the deposition of basement-proximal detrital siliciclastic sediments into the Lusale basin. These sediments were derived mainly from basement quartzite, muscovite schist, vein quartz and alkali granitoid sources. The presence of dolomite clasts in the Conglomérat unit suggests sediment supply was not limited to the local basement source but there was an addition of transported basement-distal coastal carbonates. The Conglomérat unit at the Fishtie deposit is correlated to the regional Grand Conglomérat Formation of the Katanga Supergroup which is thought to have a glacial origin. Evidence of glacial origin for the Conglomérat unit at Fishtie include; (i) poorly sorted subangular to subrounded clasts of quartzite, schist, vein quartz, alkali granitoid and dolomite source, ranging in size from millimeter grains to boulders, sitting in a fine-grained matrix, (ii) faceted and striated clasts from various locations, (iii) microfabrics and microstructures which are diagnostic of processes associated with modern tillites; and (iv) associated sedimentary rocks indicative of glacial or periglacial conditions, including laminated facies with dropstones.

Deposition of massive and layered dolomite of the dolomite unit and the interbedded siltstone and mudstone unit overlying the Conglomérat unit indicate sabkha conditions prevailed over the basin characterized by sabkhas with alternating shallow marine incursions. Massive dolomites and dolomite-rich layers of the interbedded siltstone and mudstone unit formed during dry cycles and/or low sea levels and the siliciclastic-rich beds during wet cycles and/or high sea levels. Anoxic conditions prevailed within the sabkha lagoons, which were often cut off from the fresh sea water influx during dry cycles. This resulted in the preservation of organic matter in the siliciclastic-rich beds of the interbedded siltstone and mudstone beds and the underlying

Conglomérat unit, and the formation and preservation of syngenetic to early diagenetic pyrite.

5.1.2 Stage 2: diagenesis to late diagenesis

Diagenesis predated hydrothermal mineralization and resulted in precipitation of quartz and dolomite during burial at shallow depths and low temperature conditions. These conditions could also have led to formation of diagenetic chlorite from dolomite and feldspar overgrowths on detrital quartz and feldspar (Morad et al., 2000; Tucker et al., 2011). No remnant detrital plagioclase was observed in the drill cores that were sampled. The main effect of the formation of detrital chlorite is an increase in porosity and associated permeability. This stage was very important at preparing the siliciclastic sediments both in the Conglomérat unit and overlying interbedded siltstone and mudstone beds for the metal-bearing mineralizing fluids. The other important effect of this stage was the thermochemical sulfate reduction (TSR) and/or bacterial sulfate reduction (BSR) of dissolved evaporitic sulfates. Thermochemical sulfate reduction usually occurs at temperatures >100°C, and both TSR and BSR require carbonaceous material, resulting in the following basic reaction;

$$2CH_2O + SO_4^{2-} \rightarrow 2HCO_3^- + H_2S \qquad \text{(Equation 5.1)}$$

The presence of graphite in the sandstones of the Conglomérat unit provides evidence that the siliciclastic sediments at the Fishtie deposit contain carbonaceous material. To investigate which process between TSR and BSR was responsible for production of reduced sulfur, chlorite geothermometer was used, as shown in the table below. The chlorite geothermometer was calculated using the formula of Cathelineau (1988) as;

$$T\ (°C) = -61.92 + 321.98\ (Al_{IV}) \qquad \text{(Equation 5.2)}$$

The Al_{IV} is calculated from EMPA from chlorite geochemistry. The average temperatures recorded from chlorite geothermometer is recorded as 347±7 °C for clinochlore and 365±11 °C for chamosite. The results of the chlorite geothermometer

support the production of reduced sulfur from TSR as opposed to BSR which normally occurs at temperatures below 60°C.

In the reaction equation 2, both CO_2 and H_2S are produced. The addition of CO_2 can also cause carbonate dissolution, which can result in increased porosity. Hence, the host rocks were prepared during diagenesis to late diagenesis for the reaction with the oxidizing metal-bearing brine, by;

I. An increase in secondary porosity and permeability, due to carbonate dissolution, chlorite formation, and sulfate reduction of dissolved evaporites.

II. Filling of the primary and secondary pores with reducing H_2S- and CO_2-rich fluids. Folded dolomite-rich beds of the interbedded siltstone and mudstone unit served as the best trap sites for these fluids, and hence, they are preferentially mineralized with sulfides.

Table 5: Calculation of chlorite geothermometer from EMPA data using Cathelineau (1988) equation

Sample ID	Depth	Mineral	Si	Al (IV)	Total	Al (VI)	Al	$TCN_{85\text{-}Al}^{IV}$ (°C)	SD
KEDD-134A-89	214	Clinochlore	2.77	1.23	4.00	1.349	2.584	336	9
KEDD-134A-94	232	Clinochlore	2.71	1.29	4.00	1.378	2.666	353	11
KEDD-134A-95	234	Clinochlore	2.73	1.27	4.00	1.336	2.604	346	5
KEDD-134A-77	180	Chamosite	2.70	1.30	4.00	1.443	2.739	355	10
KEDD-134A-86	200	Chamosite	2.70	1.30	4.00	1.446	2.746	357	10
KEDD-135-117	187	Chamosite	2.62	1.38	4.00	1.321	2.703	383	19
KEDD-135-119B	188	Chamosite	2.67	1.33	4.00	1.404	2.736	367	12

5.1.3 Stage 3: hydrothermal mineralization stage

The introduction of an oxidizing Cu-Co metal-bearing brine must take place before secondary porosity and permeability are destroyed by subsequent metamorphic events. The timing of this event is thus critical as the metal-bearing fluid needs to permeate through the sediments, depositing widespread disseminated strabound mineralization.

Evidence of the presence of an oxidized metal-bearing brine at the Fishtie deposit is the formation of magnetite and Ce-rich allanite associated with sulfide mineralization in the Conglomérat unit. Petrographic observation of weathered chalcopyrite and magnetite dusting in the alkali granitoid clasts of the Conglomérat unit indicates that these rocks were clearly oxidizing in nature and are the most probable source of the metal-bearing fluids. The chlorite geochemistry data displays significant enrichment of Cu and Co, suggesting that they also contributed to the metal source.

The deposition of the Cu and Co sulfides then took place upon the mixing of the two fluids, namely a reducing H_2S-rich fluid trapped in the pores of dolomite-rich interbedded siltstone and mudstone beds and an intruding oxidizing Cu-Co metal bearing brine from the underlying Conglomérat unit. The metal-bearing basinal brines were probably forced upward into the overlying sediments by the onset of the basin dewatering along transecting structures such as the vertical to subvertical stockwork veins observed in the massive dolomite. These basinal brines are usually driven by compaction of the sedimentary basin as well as the onset of the compressional tectonics, such as the Lufilian orogeny. The hydrothermal minerals, which include Cu and Co sulfides, authigenic quartz and carbonates fill the open spaces.

5.1.4 Stage 4: regional metamorphism and metal remobilization and/or redistribution

The petrographic observation of graphite associated with biotite in the Conglomérat unit indicates that peak metamorphism increased from chlorite zone greenschist facies to biotite zone greenschist facies. The temperature conditions of the biotite zone greenschist facies was investigated using the graphite geothermometer from the Raman shift data, and the results are shown in the Table 5 below. The principal behind graphite geothermometer is that the degree of graphitization records peak metamorphic temperatures and is not affected by retrograde processes (Aoya et al., 2010). The graphite geothermometer is calculated as:

$$T\ (°C) = -445R2 + 641, \text{ where } R2 = D1/ (G + D1 + D2) \qquad \text{(Equation 2.6)}$$

The average regional metamorphic temperature calculated is 512±0.65 °C. Under these temperature conditions, local remobilization and distribution of metals in the rocks of the Conglomérat unit is possible. Evidence of a metamorphic overprint of mineralization at the Fishtie deposit include development of concordant-discordant vein system in the sandstone of the Conglomérat unit and increased Zn content in Fe-chlorite (chamosite) which is associated with biotite and graphite in the sandstone.

5.1.5 Stage 5: development of supergene (secondary) mineralization

The Fishtie deposit contains a significant amount of oxide and mixed oxide-sulfide mineralization. Supergene (secondary) ore forms when a primary sulfide ore is transformed into an oxidized ore, and this usually occurs in the upper part of a profile. The supergene mineralized zone at the Fishtie deposit is developed right below the clay zone, within the saprolite. The formation of supergene requires an exposed landmass and meteoric fluids supply. The exposed landmass in the CACB took place during uplift in the late stages of the Lufilian orogeny.

There are two most important meteoric fluids required for formation of supergene ores at Fishtie deposit, these are CO_2 and H_2O. These two species react with primary sulfides to form malachite as shown in the equations below;

$$CO_{2\,(aq)} + H_2O \rightarrow H^+ + HCO_3^- \qquad \text{(Equation 5.7)}$$

$$Cu_2S\ \text{(chalcocite)} + H^+ \rightarrow HS^- + Cu^{2+} \qquad \text{(Equation 5.8)}$$

$$2CuO_{\,(c)} + CO_{2\,(g)} + H_2O_{\,(aq)} \rightarrow Cu_2(OH)_2CO_{3\,(c)}\ \text{(malachite)} \qquad \text{(Equation 5.9)}$$

Carbon dioxide was derived from the dissolution of dolomite in the clay and saprolite zone and from the atmosphere. Presence of reprecipitated quartz-rich dolomites below the saprolite provide evidence of carbonate dissolution and release of CO_2 to form malachite. Malachite is a major void-filling mineral, which combines Cu^{2+} and CO_3^{2-}. In the same Eh-pH field, malachite coexists with associated Cu and Co

minerals like heterogenite, chrysocolla, native copper etc (De Putter et al., 2010). The heterogenite and malachite rich zones in borehole KEDD-140 displays a cobalt cap right above the copper rich zone. This is attributed to adsorption of cobalt on manganese oxide (pyrolusite).

Chapter 6 Conclusion

Copper and cobalt mineralization at the Fishtie deposit is zoned with the supergene (secondary) mineralization zone overlying a primary sulfide mineralization zone. The primary sulfide mineralization zone consists of an early detrital to diagenetic sulfide mineralization associated with Mg-chlorite mineralization observed in the alkali granitoid clasts of the diamictite of the Conglomérat unit. Oxidizing fluids which interacted with the Conglomérat leached Cu and Co from the granitoids clasts and deposited Cu and Co sulfide minerals comprising of chalcopyrite, bornite, chalcocite, and cobaltite in structural and lithological traps in the stockwork veins and folded interbedded siltstone and mudstone unit. The primary sulfide minerals formed through interaction of the metal-bearing fluids and the reduced H_2S trapped in the pores of the dolomitic-rich beds. Thermochemical sulfate reduction of dissolved evaporite in the presence of organic matter is supported as the main process behind production of reduced sulfur by a chlorite geochronometer of approximately 340°C. Later remobilization and redistribution of sulfides in the Conglomérat unit into discordant-concordant veins took place during the Lufilian orogeny which was characterized by peak metamorphism increases from chlorite greenschist zone facies to biotite greenschist facies. This process happened at temperature conditions of approximately 500°C, calculated from the graphite geothermometer. Supergene mineralization formed during uplift and exposure of land mass during the late stages of the Lufilian orogeny. Water and carbon dioxide which was sourced from the atmosphere and dissolution of dolomite, were the main drivers of supergene mineralization. A spatial distribution of Cu and Co rich zones is observed in some boreholes where a cobalt cap overlies a copper rich zone. This is attributed to the presence of manganese oxide minerals (pyrolusite) which might have acted as sites of adsorption for cobalt. Supergene Co is

hosted mainly as malachite, chalcocite, azurite, chrysocolla, native copper and conichalcite. Secondary cobalt minerals consist of heterogenite, cobaltoan dolomite, and goethite.

References

A., M. & A., Z. "Petrography and geochemistry of the late Eocene “early Oligocene submarine fans and shelf deposits on Lemnos Island, NE Greece. Implications for provenance and tectonic setting", *Geological Journal,* vol. 45, no. 4, pp. 412-433.

Annels, A.E. & Simmonds, J.R. 1984, *Cobalt in the Zambian Copperbelt*.

Broughton, D.W. 2014, *Geology and ore deposits of the Central African Copperbelt*, Colorado School of Mines.

Cailteux, J.L.H., Kampunzu, A.B. & Lerouge, C. 2007, *The Neoproterozoic Mwashya–Kansuki sedimentary rock succession in the central African Copperbelt, its Cu–Co mineralisation, and regional correlations*.

Cikin, M., Drysdall,A.R., 1971, *The geology of the country North-west of Mumbwa (The Big Concession) : explanation of degree sheet 1426, SE quarter*, Geological Survey of Zambia, Lusaka.

Gazley, M.F., Hines, B.R. & McFarlane, A. 2015, "Application of principal component analysis and cluster analysis to mineral exploration and mine geology", *AusIMM New Zealand Branch Annual Conference 2015*AusIMM New Zealand, Dunedin, New Zealand, 30 August to 2 September, pp. 131.

Hitzman, M.W., Oreskes, N. & Einaudi, M.T. 1992, *Geological characteristics and tectonic setting of proterozoic iron oxide (Cu-U-Au-REE) deposits*.

Hitzman, M.W., Broughton, D., Selley, D., Woodhead, J., Wood, D. & Bull, S. 2012, "The Central African Copperbelt: Diverse Stratigraphic, Structural, and Temporal Settings in the World's Largest Sedimentary Copper District" in *Geology and Genesis of Major Copper Deposits and Districts of the World: A Tribute to Richard H. Sillitoe*, eds. J.W. Hedenquist, M. Harris & F. Camus, Society of Economic Geologists, pp. 0.

Jacobs, T.T. 2016, *Process Mineralogical Characterization of the Kansanshi Copper Ore, NW Zambia*, University of Cape Town.

Lobo-Guerrero, A.S. 2010, *Iron oxide–copper–gold mineralization in the greater Lufilian arc, Africa*, Short Course Notes 20 edn, Geological Association of Canada.

Oberle, B., Bringezu, S., Hatfield-Dodds, S., Hellweg, S., Schandl, H., Clement, J., Cabernard, L., Che, N., Chen, D., Droz-Georget, H., Ekins, P., Fischer-Kowalski, M., Flörke, M., Frank, S., Froemelt, A., Geschke, A., Haupt, M., Havlík, P., Hüfner, R. & Zhu, B. 2019, *UN Global Resources Outlook 2019: Natural Resources for the Future We Want*.

Porada, H. 1989, *Pan-African rifting and orogenesis in southern to equatorial Africa and eastern Brazil*.

Rainaud, C., Master, S., Armstrong, R.A., Phillips, D. & Robb L.J. 2005, "Monazite and U–Pb dating and 40Ar–39Ar thermochronology of metamorphic events during the Lufilian Orogeny", *Journal of African Earth Sciences*, vol. 42, pp. 183-199.

Rose, A. 1976, "The effect of cuprous chloride complexes in the origin of red-bed copper and related deposits", *Economic Geology*, vol. 71, pp. 1036-1048.

Schmandt, D., Broughton, D., Hitzman, M.W., Plink-Bjorklund, P., Edwards, D. & Humphrey, J. 2013, "The Kamoa Copper Deposit, Democratic Republic of Congo: Stratigraphy, Diagenetic and Hydrothermal Alteration, and Mineralization", *Economic Geology*, vol. 108, no. 6, pp. 1301.

Selley, D, Broughton, D, Scott, RJ, Hitzman, M, Bull, SW, Large, RR, McGoldrick, PJ, Croaker, M and Pollington, N 2005, "A New Look at the Geology of the Zambian Copperbelt", *Society of Economic Geologists*, vol. One Hundredth Anniversary Volume 1905–2005, pp. 965.

Sillitoe, R.H., Perelló, J., Creaser, R.A., Wilton, J. & Dawborn, T. 2015, *Two Ages of Copper Mineralization in the Mwombezhi Dome, Northwestern Zambia: Metallogenic Implications for the Central African Copperbelt*.

Sweeney, M.A., Binda, P.L. & Vaughan, D.J. 1991, *Genesis of the ores of the Zambian Copperbelt*.

Theron, S.J. 2013, "The origin of the Central African Copperbelt: in a nutshell", *The Southern African Institute of Mining and Metallurgy Base Metals Conference 2013*, pp. 21.

Unrug, R. 1988, "Mineralization controls and source of metals in the Lufilian fold belt, Shaba (Zaire), Zambia, and Angola", *Economic Geology*, vol. 83, pp. 1247-1258.

Williams, P.J. 1994, "Iron mobility during synmetamorphic alteration in the Selwyn Range area, NW Queensland: implications for the origin of ironstone-hosted Au-Cu deposits", *Mineralium Deposita*, vol. 29, no. 3, pp. 250-260.

Williams, P.J., Barton, M.D., Johnson, D.A., Fontboté, L., Haller, A.d., Mark, G., Oliver, N.H.S. & Marschik, R. 2005, "Iron Oxide Copper-Gold Deposits: Geology, Space-Time Distribution, and Possible Modes of Origin" in *One Hundredth Anniversary Volume*, eds. J.W. Hedenquist, J.F.H. Thompson, R.J. Goldfarb & J.P. Richards, Society of Economic Geologists.

Waele, B., Kampunzu, A.B., Mapani, B. & Tembo, F. 2006, "The Irumide Belt of Zambia", *Journal of African Earth Sciences*, vol. 46, pp. 36-70.

Wolf, K.H. 2021, "Handbook of Strata-Bound and Stratiform Ore Deposits, part III. Vol. 10. Bibliography and Ore Occurrence Data; Indexes Vols. 8-10".